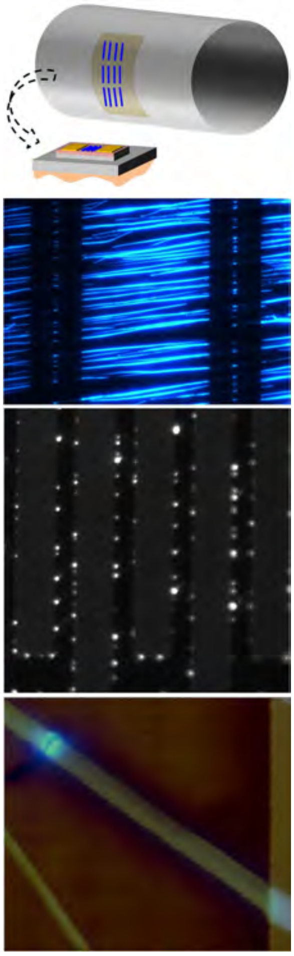

Integration of organic nanofibers by soft transfer techniques and nanostenciling

Ph.D. Thesis
NanoSYD
MCI - Mads Clausen Institute
University of Southern Denmark

Luciana Tavares

August 31, 2011

Front cover image captions:

First image: Illustration of the roll printing technique for integration of organic nanofibers into devices.

Second image: Fluorescence microscope image of para-hexaphenylene (p6P) nanofibers on a field-effect transistor (FET) device with top contact configuration.

Third image: Electroluminescence from p6P nanofibers on a FET device with bottom contact configuration.

Fourth image: Superposition of a tapping mode atomic force microscope (AFM) image and a fluorescence microscope image of p6P nanofibers on a FET device with bottom contact configuration.

Preface

This thesis has been submitted as a partial fulfillment of the requirements to obtain the Ph.D. degree at the University of Southern of Denmark (SDU). The main part of the work has been carried out at NanoSYD - Mads Clausen Institute (MCI), SDU, within the program Functional Materials and Nanotechnology from September 1, 2008 to August 31, 2011 under supervision of Associate Prof. Jakob Kjelstrup-Hansen and Prof. Horst-Günter Rubahn. The first year of the Ph.D. project was carried out at the Federal Institute for Materials Research and Testing (BAM), Berlin, Germany in collaboration with Prof. Heinz Sturm. Apart from this thesis, a number of other publications have also been made during this project. These are listed in appendix A.

At first I acknowledge Jakob Kjelstrup-Hansen for helping to plan the project, for always encouraging the development of new ideas, for helping to perform experiments, reviewing the articles and this thesis, for the valuable discussions, for the excellent supervision overall and finally for making this work possible. I also acknowledge the supervision given by Horst-Günter Rubahn. His scientific contributions were fundamental for this thesis.

I am grateful to Heinz Sturm from BAM for the scientific collaboration, for his support and help when I had just moved from my home country to Germany.

I would like to thank Kasper Thilsing-Hansen for helping to develop the device substrates and for maintaining the equipment always in perfect operational conditions. In addition, his previous findings within nanofiber growth and transfer were essential for the realization of this thesis.

I wish to thank my colleagues and the technicians at MCI for their help and support. Martin Aage Barsøe Hedegaard and Kit Drescher Jernshøj from Institute of Technology and Innovation (ITI), SDU, Odense, I thank for collaborating with the Raman experiments.

Finally, I would like to thank the support of my family and friends in Brazil especially my parents and sister for understanding my absence these last years.

August 31, 2011

Luciana Tavares
NanoSYD
MCI - Mads Clausen Institute
University of Southern Denmark
Alsion 2
DK-6400 Sønderborg
Denmark

Abstract

Self-assembled semiconductor nanostructures are foreseen to have great impact on next generation miniaturized electronic and photonic devices. So far, submicron optoelectronic devices such as multicolor LEDs, lasers, and photodetectors have almost exclusively been demonstrated using inorganic nanowires due their excellent and well-behaved electrical properties combined with a decent mechanical strength that enables easy manipulation of these materials without damage. Organic semiconductors based on small molecules have several advantages over inorganic materials including lower cost, flexibility, and tunability of their properties through chemical synthesis of appropriate molecular building blocks that can self-assemble into crystalline nanostructures. However, such organic nanoaggregates are van der Waals bonded crystals and are therefore more fragile than the covalently bonded inorganic nanowires. This makes the manipulation and thus integration of such organic materials a significant challenge.

In this thesis, it is shown how organic crystalline nanofibers with extraordinary optoelectronic properties can be transferred in a controlled fashion from their growth substrate to a receiver substrate by a roll printing technique that maintains the nanofibers' integrity and thereby enables their integration onto device platforms.

The roll printing method is used to integrate the organic nanofibers in different field-effect transistor platform configurations. Electrical characterization reveals significant differences in electrical performance between the different configurations (bottom contact/bottom gate, bottom contact/top gate, and top contact/bottom gate). Top contact devices exhibit better performance presumably due to a cleaner interface between the electrode and the organic material and consequently a lower contact resistance compared to bottom contact devices. The output characteristics for top contact devices are dominated by the nanofiber bulk as opposed to the bottom contact devices, which exhibit injection limited behavior. These new results shed light on the charge carrier injection and transport properties in crystalline organic nanostructures.

In addition, the integration of the nanofibers on similar transistor platforms has enabled for the first time the observation of polarized and highly localized electroluminescence from such nanofibers. In these light-emitting

devices, the application of an AC voltage to the transistor gate electrode causes sequential injection of holes and electrons into the organic material with subsequent strongly localized light emission upon charge carrier recombination. Their morphology enables the nanofibers to function as optical waveguides and part of the generated light is therefore guided along the nanofiber and radiated at a nanofiber end.

Another important aspect for device integration of organic nanofibers is the lifetime of the devices. Organic materials can suffer from a photoreaction (bleaching) when exposed to UV light under ambient conditions. To avoid or at least minimize such reaction investigations of different coating materials have been performed. The ideal coating should avoid the degradation of the organic material and at the same time maintain the intrinsic material characteristics. A suitable bilayer polymer/oxide coating has been found in which first a polymer material is used as a protection layer to avoid any modification of the nanofibers' luminescence spectrum, and second an oxide layer is used as an oxygen blocker to significantly reduce the bleaching.

These new results show that organic nanofibers can be implemented as device components on field-effect transistor platforms. The demonstration of an organic nanoscale light-emitter show the possibility of developing a miniaturized on-chip light source with tunable emission spectrum for future nanophotonic and lab-on-chip optical detector applications.

Dansk Resumé

Selvsamlende halvleder-nanostrukturer er forudset til at have stor indvirkning på næste generation af miniaturiserede elektroniske og fotoniske *devices*. Hidtil er optoelektroniske komponenter på sub-mikrometerskala såsom flerfarvede lysdioder, lasere og fotodetektorer næste udelukkende blevet demonstreret ved brug af inorganiske nanotråde pga. deres fortrinlige og ensartede elektriske egenskaber kombineret med en udmærket mekanisk styrke, som tillader nem manipulation uden beskadigelse. Organiske halvledere baseret på små molekyler har en række fordele sammenlignet med inorganiske materialer såsom lavere pris, mekanisk fleksibilitet og muligheden for at justere deres egenskaber via kemisk syntese af passende molekylære byggeklodser, som kan danne krystallinske nanostrukturer gennem en selvsamlende proces. Sådanne organiske nanostrukturer er imidlertid såkaldte van der Waals-bundne krystaller og er derfor mere skrøbelige end de kovalent-bundne inorganiske nanotråde. Dette medfører, at manipulationen og dermed også integrationen af sådanne organiske materialer er en væsentlig udfordring.

I denne afhandling vises det, hvordan organiske, krystallinske nanofibre med ekstraordinære optoelektroniske egenskaber kan overføres på kontrolleret vis fra deres vækst-substrat til et modtager-substrat via en rulleprintteknik, der bibeholder nanofibrenes struktur og dermed gør det muligt at integrere dem på *device*-platforme.

Rulle-printeteknikken er blevet benyttet til at integrere de organiske nanofibre i forskellige felteffekt-transistor-konfigurationer. Elektrisk karakterisering har vist, at der er væsentlige forskelle på de elektriske egenskaber af de forskellige konfigurationer (bund-kontakt/bund-gate, bund-kontakt/top-gate og top-kontakt/bund-gate). Transistorer med top-kontakter udviser bedre egenskaber formodentlig pga. en renere grænseflade mellem elektroden og det organiske materiale og dermed en lavere kontaktmodstand sammenlignet med transistorer med bund-kontakter. Udgangskarakteristikken for transistorer med top-kontakter er domineret af nanofiberen selv i modsætning til transistorer med bund-kontakter, som udviser en karakteristik domineret af grænseflade-barrieren. Disse nye resultater kaster lys på ladningsbærer-injektion og transport-egenskaber i krystallinske, organiske nanostrukturer.

Desuden har integrationen af nanofibrene på lignende transistor-platforme

gjort det muligt for første gang at observere polariseret og yderst lokaliseret elektroluminescens fra sådanne nanofibre. I disse lysudsendende komponenter bevirker påtrykkelsen af en AC-spænding på transistorens gate-elektrode, at der sekventielt injiceres huller og elektroner ind i det organiske materiale med efterfølgende ladningsbærer-rekombination og yderst lokaliseret lysudsendelse. Deres morfologi gør nanofibrene i stand til at virke som optiske bølgeledere, og en del af det genererede lys bliver derfor guidet langs med nanofiberen og udsendt fra enden af nanofiberen.

Et yderligere væsentligt aspekt for anvendelsen af organiske nanofibre er levetiden af de fremstillede *devices*. Organiske materialer kan undergå en fotoreaktion (blegning), når de udsættes for UV-lys under atmosfæriske betingelser. For at undgå eller i det mindste minimere en sådan reaktion er undersøgelser af forskellige beskyttende materiale-lag blevet udført. Den ideelle beskyttelse skal undgå nedbrydelsen af det organiske materiale og på samme tid bibeholde materialets intrinsiske egenskaber. En velegnet kombination af et polymer- og et oxid-lag er blevet fundet, hvor polymer-laget bruges til at undgå ændringer i nanofibrenes luminescensspektrum, mens det efterfølgende oxid-lag virker som oxygen-spærre og derved reducerer blegningen væsentligt.

Disse nye resultater viser, hvordan organiske nanofibre kan implementeres som komponenter på felteffekt-transistor-platforme. Demonstrationen af en organisk, nano-skala lyskilde viser, at det er muligt at udvikle en miniaturiseret, chip-baseret lyskilde med et justerbart emissionsspektrum til fremtidige nanofotoniske og *lab-on-chip* optisk detektions-anvendelser.

Contents

Chapter 1

Introduction

1.1 Nanotechnology

Nanotechnology according to Handbook of Nanotechnology [1] "literally means any technology performed on a nanoscale that has applications in the real world. Nanotechnology encompasses the production and application of physical, chemical, and biological systems at scales ranging from individual atoms or molecules to submicron dimensions, as well as the integration of the resulting nanostructures into larger systems". This means that nanotechnology is a highly cross-disciplinary field and the application areas are similarly very broad. Nanotechnology thus covers several domains as for example nanoelectronics [2], nano-optics [3], nanomechanics [4], and nanofluidics [5], and it has been used for different applications as in sensing [6], diagnostics [7], and data transmission/modulation [8], and probably most importantly data processing using integrated circuits (ICs) [9].

Today, ICs consist of millions or even billions of individual transistors. The higher the number of transistors, the better a performance can be achieved, but this requires at the same time a similar device scaling of transistor size. As described by Moore's law, the number of transistors on the chip doubles roughly every two years [9], which has enabled the extremely powerful computers available today.

The production of modern ICs is based on a top-down fabrication scheme, where the device structures are defined by lithography and realized for example by plasma etching. This type of fabrication technology has proven extremely successful for the large scale integration processes in semiconductor manufacturing. While the very stringent processing requirements within modern complementary metal-oxide semiconductor (CMOS) technology make the introduction of new materials and processes into the production line difficult, the rapid development of advanced fabrication technologies has at the same time opened up a range of possibilities within other application areas that can benefit from these tools. These include for example microelectromechanical systems (MEMS) [10], which are mechanical microsystems that can function, e.g. as pressure sensors [11, 12] or accelerometers [13], and microfluidic systems for example for bio/chemical sensing [14]. While these commercial applications still usually make use of a top-down fabrication scheme, a second and very promising strategy is the integration of bottom-up fabricated nanostructures with top-down fabricated microsystems. This can enable the use of new materials to produce nanostructures with new optical and electrical functionalities that can be engineered at the atomic/molecular level [15, 16]. In addition, such bottom-up fabricated nanostructures are typically prepared by relatively inexpensive self-assembly processes and therefore have a significant potential also for high-volume fabrication [17].

In this direction, 1D semiconductor nanowires are foreseen to have great impact on the next generation of miniaturized electronic and photonic devices [18] and could offer improved or new functionality compared to Si technology.

1.1.1 1D nanostructures

Nanostructures are defined as structures with at least one dimension between 1 and 100 nm [19] and are of great interest because dimensionality plays an important role in determining the property of a material. For example, electrons interact differently in 3D, 2D (thin films), 1D (nanowires, nanorods, nanobelts, nanofibers, and nanotubes), and 0D (quantum dots) structures. This affects the material's band gap, density of states, electron (hole) effective mass, etc [19, 20, 21]. While 1D nanostructures can be fabricated both via top-down and bottom-up strategies [19, 22], here the focus will be on the bottom-up type only.

Submicron optoelectronic devices made of 1D nanostructures have almost exclusively been demonstrated using inorganic materials. Such nanowires have been used to develop devices as for example field-effect transistors (FET) [23], lasers [24, 25], nanoscale solar cells using a p-i-n junction [26], and photodetectors [24, 27]. For example, Kind *et al.* [27] developed a photodetector where ultraviolet light exposure changes the ZnO nanowires state from insulating ("OFF") to the UV-exposed conducting state ("ON"). Huang *et al.* [28] fabricated a multicolor nanoscale LEDs, which were made by combining inorganic III-V nanowires with silicon nanowires to create a p-n junction (Figure 1.1). Also, infrared nanoLEDs made from a III-V semiconductor core-shell nanopillar structure were demonstrated using a direct growth technique that can more easily be upscaled [29]. The nanopillars were grown by vapor deposition on a silicon substrate and subsequently electrically contacted by a complex processing procedure [29].

Although the inorganic materials have good and well-behaved electrical properties, they also present a lack of tunability offered by organic materials

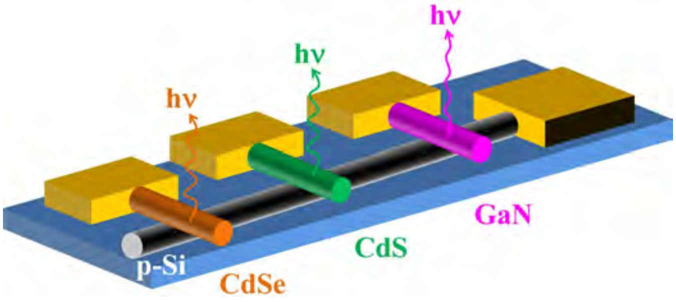

Figure 1.1: Light emission from nanowires. Image adapted from [28].

via chemical synthesis of the molecular building blocks [30], which shows the importance of the study of organic materials as active structures for device applications.

1.1.2 Why use organic nanofibers?

Compared to their inorganic counterparts, organic materials have several advantages including lower cost, flexibility [31, 32], and most notably the ability to tune their intrinsic properties via chemical synthesis of molecular building blocks [30].

1D organic nanofibers made of small molecules can be produced via different routes as for example from solution [33, 34] or by vapor deposition [35, 36]. The overlap of π-orbitals in the crystalline structure of the nanofiber strongly affects the electrical transport properties [37], which improves their characteristics over unordered films. Some organic nanofibers show unique characteristics as for example polarized light emission [30]. This is due their crystallinity and the specific orientation of the emitting dipoles along the molecules' long axes.

Organic nanofibers have been used to demonstrate some device components including field effect transistors [33] and photodetectors [34]. However, a significant obstacle towards the large-scale device implementation is the soft and fragile structure of such organic nanofibers, which makes integration on suitable device substrates challenging.

1.2 Nanostructure integration

In order to use 1D nanostructures as device components, it is often necessary to integrate them on a device platform. The integration of 1D nanostructures into devices is typically done in one of two ways: either via *in-situ* growth where the nanostructure is fabricated directly on the device platform, or via transfer from the growth substrate to a device substrate.

In-situ growth is a promising technique for upscaling the integration of nanostructures in devices. However, it also places some significant restrictions on the device substrate, which must facilitate the growth. This can include the use of catalyst particles to control the growth position [19] or the use of a special, crystalline substrate for epitaxy to control growth direction [38]. Such conditions represent a significant limitation on both the type of device substrate material and nanostructure as well. For example, high temperature processing [39] for nanostructure growth can prevent the use of flexible substrates.

Integration by transfer involves the growth of the nanostructures on a suitable growth substrate followed by their transfer to a pre-processed device substrate. Since these methods use different growth and device substrates, there are much fewer restrictions than with the *in-situ* growth method. In addition, the transfer techniques allow the integration of nanostructures on device substrates with controllable positioning and alignment at relatively large scale. Below is a short overview of the important aspects about integration of nanostructures by transfer, since this technique represents an important step in the nanofabrication process that is used in this thesis.

1.2.1 Transfer techniques

Inorganic and graphene-based nanomaterials

So far, large-scale integration strategies based on transfer of nanostructures from a growth donor substrate to a device receiver substrate have been demonstrated almost only for inorganic and graphene-based nanomaterials [40, 41, 42, 43, 44, 45, 46]. Typically, the nanowires are transferred either 1) via solution or 2) via direct transfer.

Transfer via solution

Transfer via solution can be done using drop-casting [47], and can potentially result in aligned nanowires using, e.g. microfluidic alignment [43] or dielectrophoresis [48]. In the simple drop-casting method, the nanowires are suspended in solution and a droplet is applied to the device substrate resulting in only little position and alignment control of the transferred nanowires [47, 49]. Within a microfuidic scheme, the nanowire solution is pumped through a microfluidic channel attached to the device substrate surface. The shear forces created during the flow of the confined fluid results in the deposition of the nanowires on the microchannel walls with preferential alignment in the flow direction [43]. Dielectrophoresis can also be used to align nanowires [41]. With this method, an applied electric field induces a polarization of the particles. The field can then exert a force on the particles and cause them to align [48, 50].

Direct transfer

The direct transfer methods avoid the initial step of dispersing the nanowires in a liquid solution. Instead, the nanowires are transferred directly from the growth substrate to the receiver substrate by typically some form of contact printing. When using a transfer technique, the adhesion and orientation of the nanostructures on the growth substrate play an important role. In one version of the contact printing scheme (shear-based contact printing) [40, 42, 51], the growth substrate with a "forest" of vertically-aligned nanowires is placed in contact with a patterned receiver substrate and slided against it. The sliding motion induces a shear force that breaks the nanowires at the "root" and horizontally connect them to the receiver substrate resulting in the transfer of aligned nanowires (see Figure 1.2) [42].

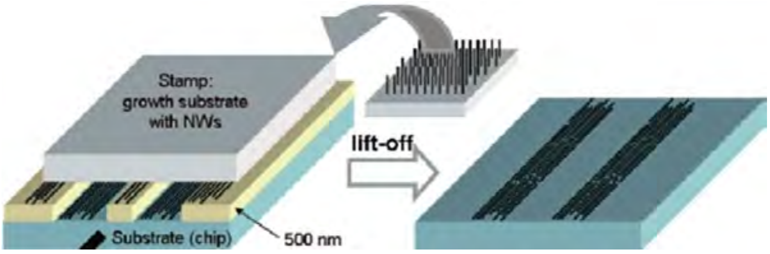

Figure 1.2: Contact printing. Image from [42].

The contact printing technique can be scaled up by the differential printing technique (Figure 1.3) [52]. In the differential printing scheme, the nanowires are initially grown on the surface of a tube, which during the rolling motion also slides against the receiver substrate creating the required shear force [52]. The main issue of the techniques based on shear forces is the force necessary to reorient and make the nanowires adhere to the receiver substrate without damaging the nanostructures [40]. It is important to note that shear-based contact printing is viable for inorganic nanowires, which are significantly more mechanically robust [53] compared for example to organic nanofibers [54].

Transfer by stamping does not involve any sliding motion of the substrate and consequently no shear forces. Stamping has been demonstrated for nanowires [55] and also for graphene-based films [46]. The stamping of nanowires can be done by applying an adhesive tape to the top of the growth substrate, peeling off the tape with the nanowires, pressing the tape with the nanowires against the receiver substrate, and then peeling off the adhesive tape [55]. In the stamping technique for vertically grown nanowires [55], the transferred nanowires do not exhibit the parallel alignment as observed for the contact sliding printing methods (Figure 1.2) [42].

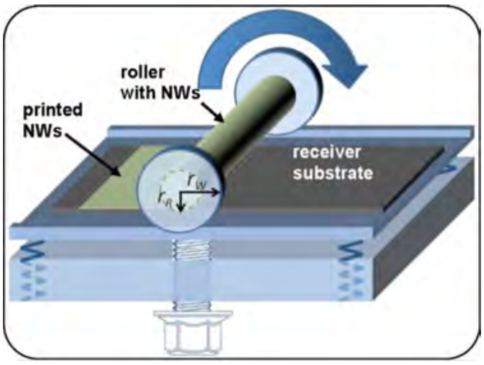

Figure 1.3: Differential roll printing. Image from [52].

1.2.2 Organic nanofiber integration

Organic nanostructures made from small molecules are weakly van der Waals bonded crystal structures [54], and are therefore much more fragile than the covalently bonded structures like nanowires, graphene and carbon nanotubes. This has to be taken into consideration when developing a transfer technique for organic structures.

One report by Bao and co-workers demonstrated a solution-based filtration-and-transfer method for organic microwires based on a complex vacuum filtration scheme that enabled the transfer of partially aligned microwire arrays, however with the alignment deteriorating when scaled to larger areas [56].

In the NanoSYD research group, a few transfer experiments with organic nanofibers have been carried out. Transfer of organic nanofibers has previously been done using a method based on drop-casting and the use of a small shadow mask (Figure 1.4) [57]. This technique enables the transfer of a few nanofibers but is very time consuming and large scale transfer is practically impossible. Transfer by stamping arrays of aligned organic nanofibers under controlled humid conditions without sliding and consequently free of shear forces has been proposed by Thilsing-Hansen [58]. The growth substrate with surface-bound nanofibers was pressed against the receiver substrate inside a sealed box with a controlled atmosphere and mechanical springs were used to control the pressure applied during the stamping. However, the transfer via stamping requires perfect parallelism of the as-grown and receiver substrate otherwise the misalignment results in unsuccessful transfer of the nanofibers. Large-scale transfer of organic nanofibers is still a very challenging task and is one of the key topics investigated in this thesis.

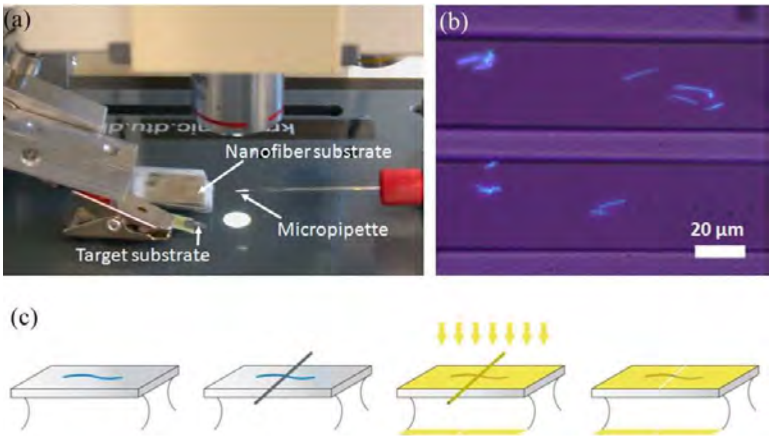

Figure 1.4: (a) Image of the setup for drop-casting integration of the organic nanofibers. (b) Fluorescence microscope image of the nanofibers transferred to the device substrate. (c) Scheme of a rigid nanowire used as a small shadow mask during deposition of metal contacts. Adapted from [57] and private communication.

1.3 Key topics of the thesis

Chapter 2 contains a brief introduction to the organic para-hexaphenylene (p6P) nanofibers used in this work. p6P nanofibers are crystalline nanostructures, which possess extraordinary optical properties.

In chapter 3, a new roll printing method for efficient and accurate integration of p6P nanofibers onto different device platforms is presented. p6P nanofibers were used as a model system to demonstrate the transfer technique. The polarization properties of this type of nanostructure together with their morphology were then used to evaluate the quality of the transferred nanofibers which were found to be similar to that of the as-grown nanofibers. The versatility of the technique is demonstrated by transferring p6P nanofibers onto an unstructured glass substrate, a flexible polymeric foil, and a silicon-based microstructured transistor platform.

The second part of this project was dedicated to the development and characterization of nanofiber-based devices. Chapter 4 describes the results from electrical characterization of transferred p6P nanofibers in different field-effect transistor configurations. Significant differences are observed in the electrical performance between top and bottom contacts configurations. The better performance observed for top contact is presumably due to a cleaner interface between the contact and the organic material and due to metal penetration into the organic material during contact deposition and consequently low contact resistance compared to bottom contact geometries.

In chapter 5, p6P nanofibers are also used as a model system, since such nanofibers exhibit extraordinary optical properties including a polarized luminescence output and the ability to function as active waveguides. The p6P nanofibers were transferred to FET device platforms and an AC voltage applied to the gate caused a sequential injection of charges into the organic material and subsequently radiative recombination of the charges and light emission. In addition, optical waveguiding is demonstrated where part of the generated electroluminescence is guided along the nanofiber and radiated at the nanofiber break.

The p6P nanofibers suffer decrease of luminescence intensity (bleaching) upon UV light exposure under ambient conditions. Chapter 6 shows investigations aimed at finding an appropriate coating for p6P nanofibers that does not alter the original luminescence spectrum of the uncoated material and eliminates or at least significantly reduces the bleaching. It was found that a particular bilayer polymer/oxide film (PMMA/SiO_x) results in a significant reduction of bleaching reactions without affecting significantly the emission spectrum from the nanofibers.

Finally, the results are summarized in chapter 7 together with an outlook.

Chapter 2

Nanofiber growth and properties

2.1 Nanofiber growth

Phenylene-based molecules can self-assemble into crystalline nanofibers with special optical properties [59, 60]. For example, p6P molecules, which are composed of 6 phenylene rings in a linear chain as illustrated in Figure 2.1(a), can upon vapour deposition form nanoaggregates with the molecules sitting in the so-called herringbone crystal structure (Figure 2.1(b)) [61, 62, 63]. Coventionally, the organic nanostructures are named "nanofibers", while the term "nanowire" is typically used for elongated inorganic nanostructures. These two different terms will also be used here although they do not imply any morphogical difference between the structures.

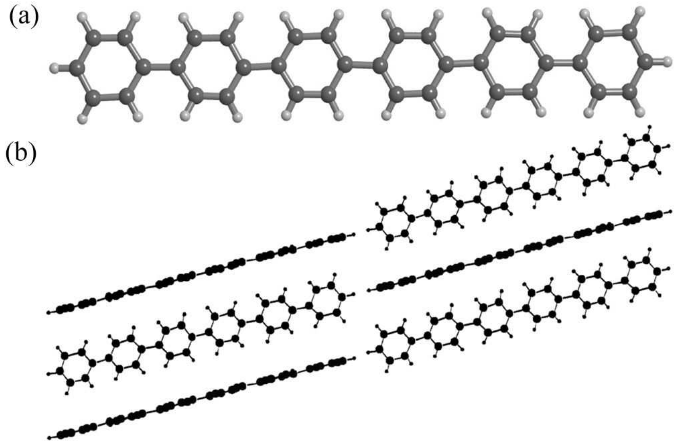

Figure 2.1: (a) Structural model of a p6P molecule. (b) The arrangement of the p6P molecules in the nanofiber crystal structure [62].

p6P nanofibers are typically prepared by vapor deposition of the p6P molecules under high vacuum conditions ($p < 10^{-8}$ mbar) from a Knudsen cell (Figure 2.2) onto a heated muscovite mica substrate. Muscovite mica is a sheet silicate, $K_2Al_4[Si_6Al_2O_{20}](OH)_4$, consisting of octahedral Al-O layers sandwiched between two tetrahedral Si-O layers. One out of four Si^{4+} cations in the upper tetrahedral layer is replaced with an Al^{3+} ion. The resulting negative charge due to the cation substitution is compensated by a layer of K^+ cations in between two tetrahedral sheets. Cleavage occurs along these interlayer cations, each cleavage face has half of the K^+ ions [64]. These ions on the surface of mica produce strong surface electric dipoles [65]. Since these dipoles play an important role in the nanofiber formation process and since they are affected by the ambient surroundings, the mica, after being cleaved in air, is quickly transferred to the vaccum chamber. By depositing p6P at a low rate ($\approx$0.1 Å s^{-1}) and keeping the substrate at an elevated temperature ($\approx$463 K), the molecules physisorp to the surface while the thermal energy enables the surface diffusion of the molecules and molecular clusters. The interaction between the molecules is stronger than towards the substrate causing assembly into the nanofiber structure [60]. It also yields parallel alignment of the long molecular axes and large tilt angles of neighbouring molecular planes [66, 67]. The surface dipoles on mica induce a preferred molecular orientation and mutually parallel nanofibers [68] with macroscopic lengths (up to millimeters) and nanoscopic cross-sections (widths of a few hundred nanometers and heights of several ten nanometers). The herringbone stacked molecules in the fibers are oriented with the (1-1-1) face parallel to the mica surface (Figure 2.3) [61].

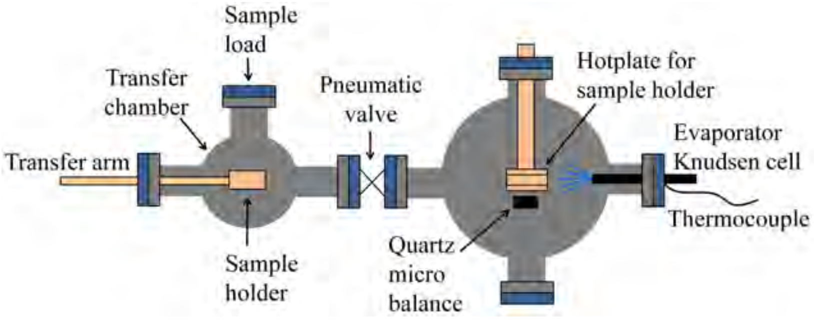

Figure 2.2: Illustration of the vapor deposition system for p6P deposition.

It should be mentioned that p6P nanofibers can also be formed on other substrates. For example on KCl where the fibers form a rectangular network due to the symmetry of the substrate [60, 64]. On gold, the parallelism of the nanofibers is lost since there is no epitaxial relation with the Au substrate [69]. However, this will not be described in details here, as only mica-grown fibers were used in this project.

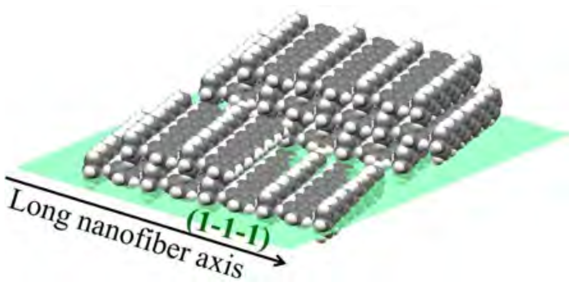

Figure 2.3: Schematic model of p6P crystal structure.

2.2 Optical characteristics

The p6P nanofibers emit blue light upon UV excitation [61] (Figure 2.4).

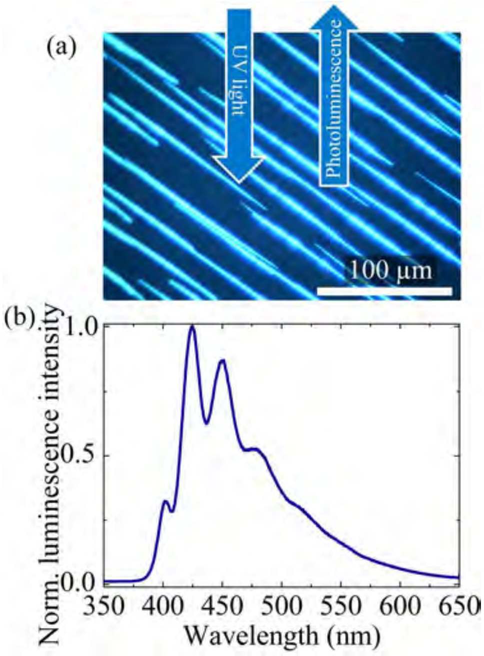

Figure 2.4: (a) Fluorescence microscope image and (b) normalized luminescence spectrum of p6P nanofibers on mica. Spectrum acquired by excitation at λ_{ex}=325 nm using a HeCD laser.

The spectrum in Figure 2.4(b) shows that the peak wavelengths of the emitted light from p6P are at ≈401 nm, ≈422 nm, ≈448 nm, and ≈473 nm, which are due to the radiative decay from the vibrational ground state of the first excited electronic state to various vibrational levels of the electronic ground state [(0→0), (0→1), (0→2), and (0→3)], respectively [70]. The emission is highly polarized [61] because the emitting dipoles are oriented along the molecules' long axes, which are mutually parallel in the herringbone-packed crystalline nanofibers. The C-C stretching vibrations of all carbon atoms of the p6P molecule can be observed as intense Raman active modes [71, 72].

The p6P nanofibers can act as waveguides [73] where part of the generated light is guided along the nanofiber and radiated at a break in the nanofiber. Due to the subwavelength cross-sectional dimensions, part of the light is guided in the evanescent field. In Figure 2.5 the waveguiding is demonstrated by irradiating the same nanofiber with UV light in different positions and detecting the propagating light that radiates from a break in the nanofiber structure [73]. Due to the nanofiber geometry, the emitted light has a spatially anisotropic distribution [74] with a large part of the light being emitted from the ends of the nanofibers while a smaller part is emitted from the top and bottom faces. p6P nanofibers also act as random lasers [75, 76, 77], where randomly spaced lines appear on top of the spontaneous emission spectrum near 425 nm when the nanofibers are photoexcited with ultra short laser pulses [75].

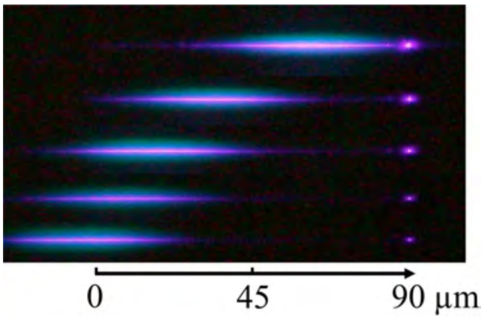

Figure 2.5: Five images of the same p6P nanofiber being excited with UV light in five different positions (large emission zone on the left side) and the propagating light being radiated from a break in the nanofiber structure. The outcoupled intensity at the break decreases for increasing distance between excitation and outcoupling point. From [73].

2.3 Electronic characteristics

In Figure 2.6, the lowest unoccupied molecular orbital (LUMO) (3.0 eV) and highest occupied molecular orbital (HOMO) (6.0 eV) for p6P [62] are illustrated. In organic materials the HOMO is a fully occupied, bonding π-orbital while LUMO is an unoccupied, anti-bonding π^*-orbital. Since the

π^* electron system is thus saturated no intermolecular covalent bonds can form, and the molecular solid is held together only by van der Waals and Coulomb forces [62].

In an organic crystal, in a simplistic view, the HOMO levels support the conduction of holes, the LUMO levels support the conduction of electrons, and photon generation occurs through the relaxation of an electron-hole pair, analogously to the valence conduction-band description in inorganic semiconductors. However, in organic semiconductors the charge transport occurs typically via a hopping mechanism, where delocalized charge carriers jump between adjacent molecules. The localization of the charge carriers in p6P is due to the relaxation of the molecular backbone, which thereby lowers the carrier mobility [62]. p6P is a high-bandgap semiconductor and can be used as the active material in opto-electronic devices. It has been previously demonstrated that unordered p6P film in an organic field-effect transistor (OFET) device shows p-type behavior [78] and can emit light with similar electroluminescence and photoluminescence spectra [79].

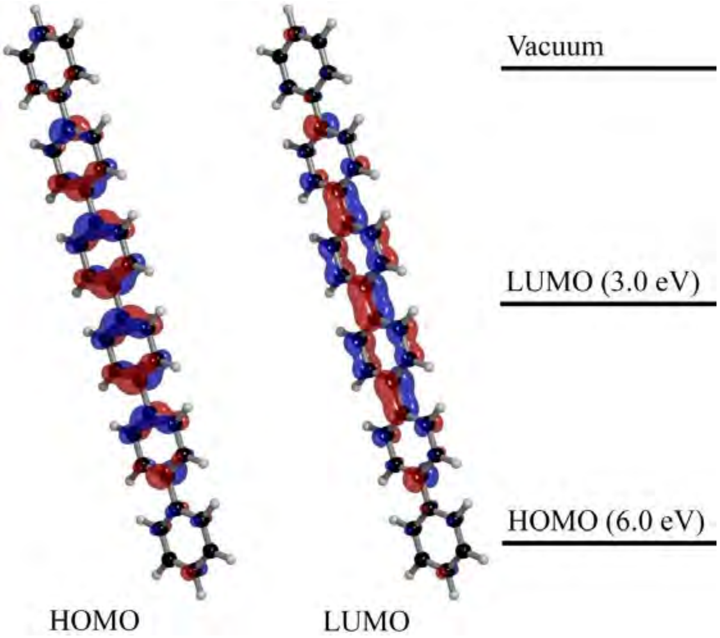

Figure 2.6: The LUMO and HOMO and their energy levels for p6P. Image adapted from [62].

2.4 Bleaching characteristics

When p6P nanofibers are exposed to UV light under ambient conditions, a significant reduction of the photoluminescence intensity with time can be observed [80]. Figure 2.7(a) shows the spectrum of the p6P nanofibers under UV illumination (λ_{ex}=365 nm) using a fluorescence microscope with an integrated UV-2A filter, which blocks wavelengths below 420 nm from passing to the detector. In Figure 2.7(b) is the decrease in luminescence intensity of the peak at ≈422 nm during almost 7 minutes. As can be seen, p6P exhibits a characteristic photoinduced reaction (bleaching) resulting in such decrease in luminescence intensity upon UV light exposure. Maibohm *et al.* [80] showed that the photo-oxidation reaction can be slowed down by irradiating the nanofibers in vacuum or by coating them with a few hundred nanometers thick layer of silicon oxide (SiO_x), which on the other hand results in changes in the original p6P spectral characteristics [80]. Using the fact that the bleaching reaction can be attenuated but not completely stabilized even in vacuum surroundings, it was proposed that the degradation process in p6P involves at least three independent processes: intramolecular configuration change, photo-oxidation, and material removal [80].

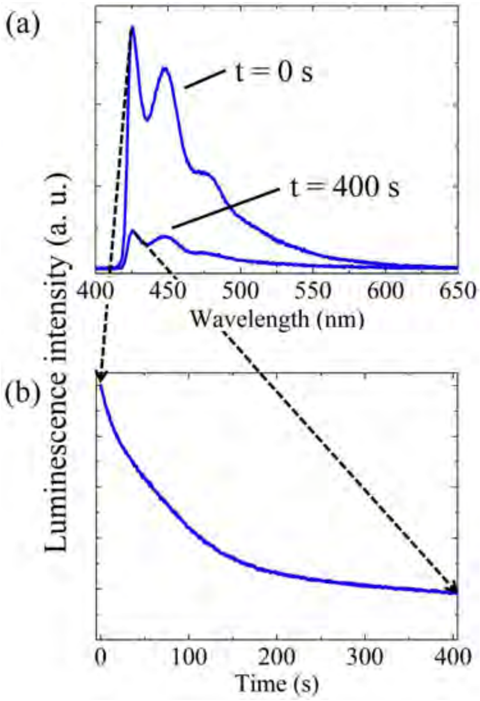

Figure 2.7: (a) Luminescence spectra and (b) luminescence intensity for emitted light at λ_{em}=422 nm as a function of time from p6P nanofibers on mica. Excitation at λ_{ex}=365 nm.

Chapter 3

Nanofiber device integration by roll printing technique

In this chapter, a simple and efficient transfer technique that enables fast and large-scale integration of highly-oriented organic nanofibers is presented. It is also shown that the intrinsic optical properties of the organic nanofibers are virtually unaffected or even improved by the transfer. In addition, two methods are demonstrated to obtain a few nanofibers on a device substrate: 1) growth of individual or a few nanofibers in a custom-designed area with subsequent transfer, and 2) transfer to an elevated platform with predefined geometry on the receiver substrate. As receiver substrates, the technologically most relevant surfaces were chosen: glass, gold, and polymer (polyethylene) spanning a large range of surface energies.

3.1 The roll printing technique

The roll printing technique for nanofiber transfer includes as a first step fixing the receiver substrate on a soft rubber to minimize nanofiber deformation during transfer and fixing the donor substrate with the as-grown nanofibers to the curved surface of a transparent cylinder with radius of curvature of 5 cm. The transparency makes it possible to visually align the desired position on the donor substrate to the receiver substrate and also enables a visual control of the contact between the surfaces, i.e. it is possible to see the deformation of the rubber used as compliant material to avoid mechanically deforming the nanofibers. In the case of a rigid donor substrate, which cannot conform to the cylindrical surface, the method can still be applied by exchanging the donor and receiver substrate positions and use a flexible receiver substrate that can be fixed to the cylinder surface. De-ionized water vapor produced using an ultrasonic vaporizer is then condensed on the receiver substrate to facilitate the transfer, as initial experiments showed that transfer in low-humidity surroundings is problematic. The spreading of the water film between the donor and receiver substrates also indicates when contact between the surfaces is established. Figure 3.1 illustrates the transfer of nanofibers to an unstructured receiver substrate.

Figure 3.1: Schematic drawing of the roll printing transfer technique using a glass cylinder.

The requirement for a successful transfer is that the adhesion of the nanofibers towards the receiver substrate is higher than the adhesion to the growth substrate [81]. However, to avoid strong tapes [55], or friction [51, 52] that can easily destroy the fragile nanofibers, the adhesion of the organic nanostructures was controlled with water vapor, which in adequate amount does not cause misalignment of the nanofibers and enable perfect transfer of the nanofibers. Here, a simplified explanation of the forces involved in the transfer of the nanofibers via capillary and/or van der Waals forces in liquid ambient is provided [1].

Van der Waals (vdW) forces between two objects are due to electromagnetic interactions between the atomic or molecular constituents of the two objects. Presumably, vdW interactions between the nanofibers and the growth substrate constitute the main adhesion force. However, vdW forces are reduced in a liquid environment [1, 62], thus the water vapor used during the transfer can aid in the release of the nanofibers via a lowering of the vdW forces that cause the nanofibers to adhere to the growth substrate.

A second contribution comes from capillary forces. The condensation of humidity or water vapor between two objects in close proximity to each other forms a liquid bridge or meniscus [62], which creates relatively large attractive forces between the objects [82]. Hydrophilic surfaces cause spreading of water while hydrophobic surfaces hinder spreading. This has an important role in capillary condensation since this largely determine the shape of the meniscus, i.e. the contact angles between the water meniscus on both the objects and therefore also the capillary force strength [83]. The capillary forces arise from the pressure difference between the inside and the outside of the meniscus [84]. The capillary forces may pull the nanofibers and increase their adhesion to the receiver surface [1, 85, 84].

Results obtained in this thesis show that the transfer works independently of the hydrophobicity of the substrates, however the transfer is strongly dependent on a suffucient humidity.

3.1.1 Optical properties of transferred nanofibers

Upon transfer, the optical properties of the nanofibers were studied by optical microscopy. The fluorescence microscope images of the nanofibers were obtained irradiating the samples with an Hg lamp (emission line of 365 nm selected by a band pass filter) and an epifluorescence microscope with a Nikon UV-2A filter cube to separate the excitation and luminescence light.

Fluorescence microscope images and polarization

The p6P nanofibers emit highly polarized light under UV excitation [61] as described in chapter 2. The polarization properties of the nanofibers make the polarization ratio a suitable parameter to quantify the extent of alteration caused by the transfer process. Figures 3.2(a) and (b) show the fluorescence microscope images of as-grown nanofibers and Figures 3.2(c) and (d) show the fluorescence microscope images of transferred nanofibers on a glass substrate imaged through a polarizer with the transmitting axis indicated by arrows. The polarization properties were quantified by positioning the sample on a goniometric stage and recording the output luminescence intensity measured through a stationary polarizer as a function of sample angle (Figure 3.2(g)). The polarization curves were fitted to Malus' law for calculating the polarization ratio $P = (I_{max} - I_{min})/(I_{max} + I_{min})$. A large polarization ratio indicates good alignment while changes in the nanofiber orientation would result in a reduction of the polarization ratio. The light intensity I from an area similar to Figures 3.2(a)-(f) was sampled at intervals of 5 degrees and imaged through a polarizer giving a polarization ratio for as-grown nanofibers of $P = 0.86 \pm 0.01$ (see Figures 3.2(a),(b),(g) and videos[1]) and for nanofibers transferred onto a glass substrate of $P = 0.85 \pm 0.01$ (see Figures 3.2(c),(d),(g) and videos[1]). The transfer to a gold-coated substrate results in a similar outcome.

Figures 3.2(e) and (f) show fluorescence microscope images of the nanofibers transferred to a thin polyethylene foil and demonstrates the viability of the modified technique with the planar and rigid donor substrate (mica supported on a rigid substrate) fixed on the compliant rubber and the flexible receiver substrate attached to the roll, giving a polarization ratio of

---

[1] See the videos "As-grown_nanofibers.avi" and "Transferred_nanofibers.avi", which show as-grown and transferred nanofibers, respectively, imaged through a stationary polarizer. The videos are available either on http://onlinelibrary.wiley.com/doi/10.1002/smll.201100660/suppinfo or on the CD attached to the last page of this thesis.

$P = 0.88 \pm 0.01$ (Figure 3.2(g)). This demonstrates that the transfer is conserving the mutual nanofiber alignment.

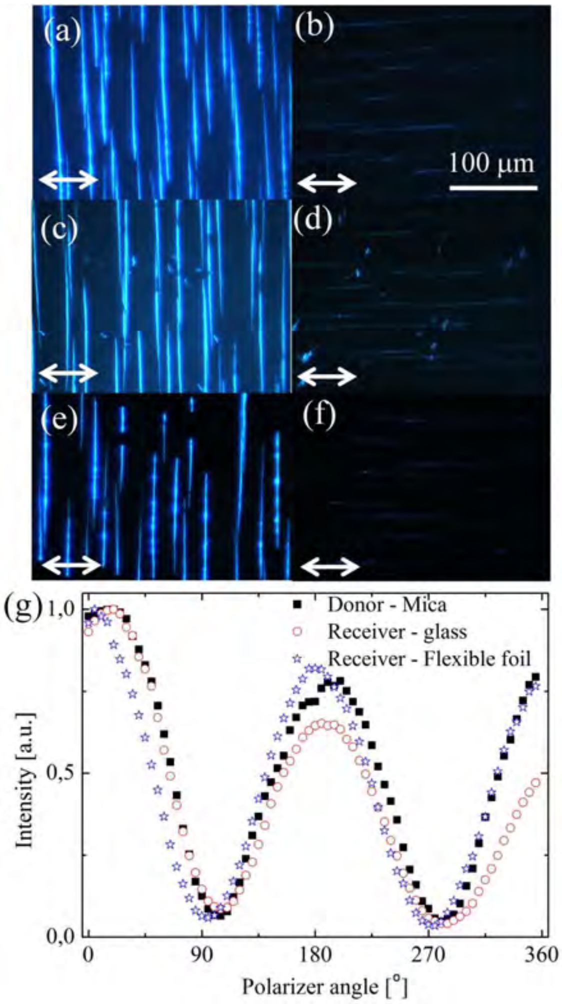

Figure 3.2: Fluorescence microscope images of the as-grown p6P nanofibers with a polarizer oriented (a) perpendicular and (b) parallel to the nanofibers. Transferred nanofibers on glass substrate with a polarizer oriented (c) perpendicular and (d) parallel to the nanofibers. Nanofibers transferred onto flexible polyethylene foil by fixing the receiver polymeric foil on the cylinder as described in the text. Images recorded through a polarizer oriented (e) perpendicular and (f) parallel to the nanofibers. The arrows indicate the polarizer direction. (g) Measured intensity from nanofibers on as-grown mica substrate, transferred nanofibers to glass, and flexible polyethylene foil as a function of polarizer angle.

Luminescence spectra and bleaching decay

The luminescence spectra and the decrease in luminescence intensity during UV illumination (bleaching) were measured to check if defects or contaminants were introduced during transfer of the nanofibers. The data was collected with a spectrometer coupled to an epifluorescence microscope via a glass fiber with 100 μm core diameter, while the samples were exposed to UV light (more details in chapter 2 and 6). The spectra (Figure 3.3(a)) and the bleaching curves (Figure 3.3(b)) from as-grown nanofibers on mica substrate and transferred to glass and flexible foil show basically the same characteristics indicating that no significant defect density or contamination were introduced during transfer.

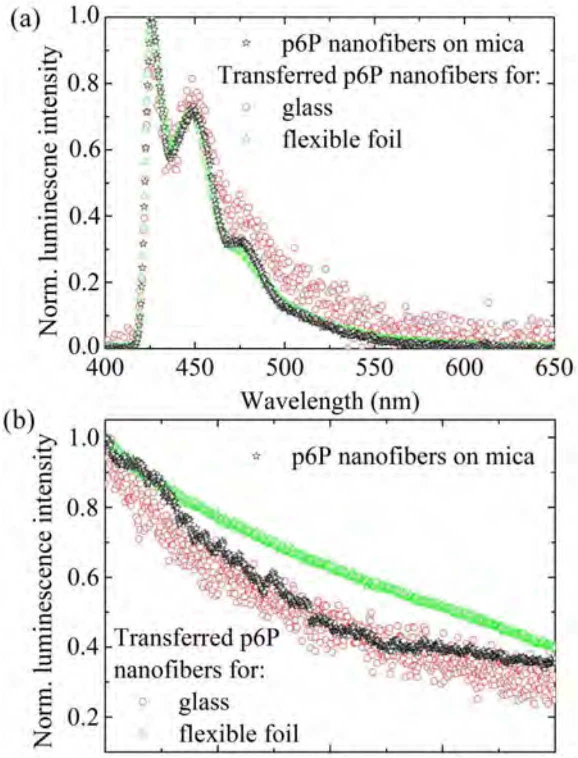

Figure 3.3: (a) Normalized luminescence spectra of p6P nanofibers on as-grown mica substrate and transferred to glass, and flexible foil. (b) Normalized luminescence intensity for emitted light at λ_{em}=422 nm as a function of time from as-grown p6P nanofibers on mica substrate and transferred to glass, and flexible foil. Excitation at λ_{ex}=365 nm.

3.2 Custom-designed nanofiber growth with nanostencil

Two methods are demonstrated to obtain a certain number of nanofibers on a device substrate. The first method that can enable transfer of only few or potentially even a single nanofiber using the roll printing transfer technique, involves the use of a nanostencil to define the nanofiber growth area before transfer (Figure 3.4(a)). The nanostencil consists of a 100 nm thick silicon nitride membrane with perforations of the desired geometry patterned using photolithography and KOH etching (stencil preparation is described in appendix C). The stencil is clamped in direct contact with the growth substrate during p6P deposition resulting in nanofibers only in a well-defined area. A stencil opening with dimensions of 10 μm x 200 μm gives rise to approximately the same number of nanofibers (9 or 10) (see Figure 3.4(b)) of around 20 μm length (Figure 3.4(c)). This shows that there are some difussion below the SiN stencil as the nanofibers are longer than the stencil openings width. This demonstrates the ability to accuratly control the number of nanofibers.

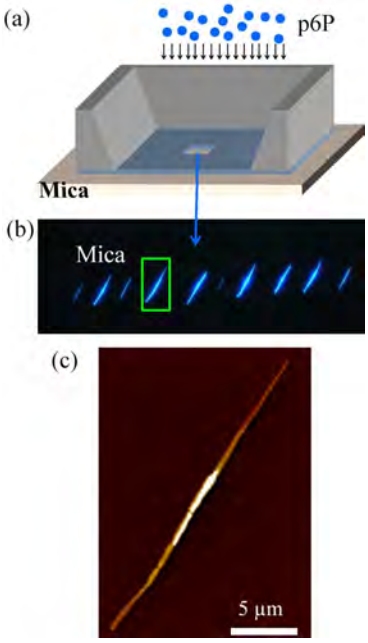

Figure 3.4: (a) Illustration of a stencil in contact with muscovite mica during p6P deposition. The stencil opening was 10 μm x 200 μm. (b) Fluorescence microscope and (c) tapping mode AFM images of p6P nanofibers on mica after deposition through the stencil. Rectangle in (b) indicates nanofiber shown in (c).

When two perforations in the SiN membrane are only a few micrometers from each other (Figure 3.5), the p6P molecules diffuse below the SiN membrane and can form nanofibers in between both stencil openings.

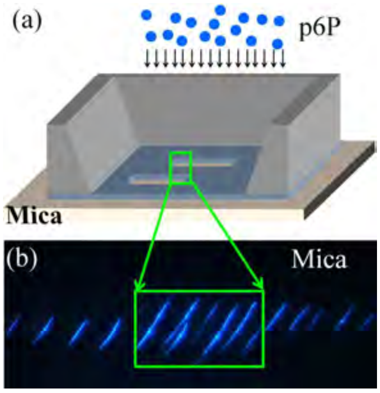

Figure 3.5: (a) Illustration of a stencil in contact with muscovite mica during p6P deposition. The stencil openings are 10 μm x 200 μm. The indicated area shows where the openings are only a few micrometers far from each other. (b) Fluorescence microscope image of p6P nanofibers on mica after deposition through two openings in a SiN stencil. The indicated area shows the nanofibers that grew between the openings and below the SiN membrane.

Figure 3.6(a) illustrates the stencil in contact with the muscovite mica substrate during p6P deposition with a opening in the SiN membrane of 120 μm x 320 μm. Figure 3.6(b) shows a fluorescence microscope image of the as-grown nanofibers on a mica substrate prepared by deposition through the stencil opening and Figure 3.6(c) shows the same nanofiber array transferred to an unstructured silicon substrate without breaks and excellent alignment of the nanofibers. Figure 3.6(d) shows magnified images of the nanofiber indicated in Figures 3.6(b) and (c) from which bright spots are clearly visible along the as-grown fibers but not along the transferred ones. These bright spots are caused by breaks in the as-grown nanofibers created during the growth process [73]. When luminescence is stimulated in p6P nanofibers, part of this light is guided along the long nanofiber axis and exits at such breaks. Since the transfer process causes the nanofibers to be flipped upside down, the light scattering from the breaks is no longer observed. To quantify this effect, Figure 3.6(e) shows intensity versus distance curves along the same indicated region of the nanofiber in Figure 3.6(d) before and after transfer. On the transferred nanofibers no irregular light scattering is observed, thus demonstrating a more homogeneous and bright light emitting surface induced by the transfer process. This can also be observed

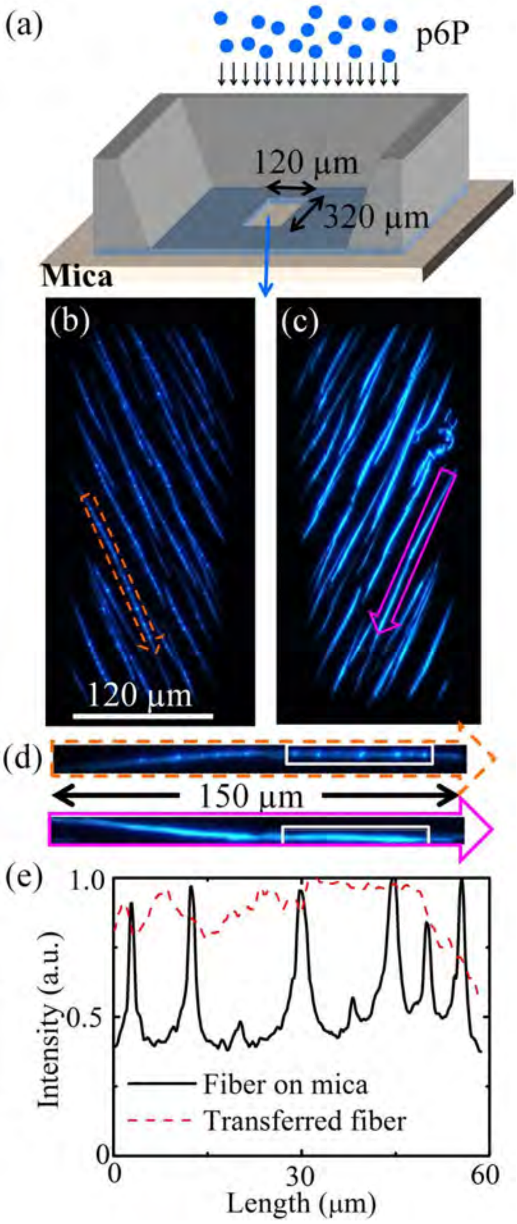

Figure 3.6: (a) Illustration of a stencil in contact with muscovite mica during p6P deposition. The stencil opening was 120 μm x 320 μm. Fluorescence microscope image of p6P nanofibers (b) on mica after deposition through the stencil and (c) the same fibers transferred to a clean substrate. (d) Magnified view of the same nanofiber before and after transferring. (e) Luminescence intensity of the selected area indicated in (d).

from the videos[2]) and for nanofibers transferred onto a glass substrate of $P = 0.85 \pm 0.01$ (see Figures 3.2(c),(d),(g) and videos[2]). The vanishing of the bright spots is observed only when nanofibers are transferred onto a planar receiver, whereas transfer to a flexible receiver attached to the roller causes the bright spots to still be visible as can be observed in Figures 3.2(e) and (f). This is presumably due to the manipulation of the flexible polymeric foil during detachment from the roll.

3.3 Transfer to prestructured receiver substrate

The second strategy to obtain a few nanofibers on a device substrate includes transfer to a prestructured receiver substrate. Here, it is demonstrated using a field-effect transistor (FET) device as the receiver substrate. The FET platform design was optimized based on the nanofibers' size and typically density to facilitate efficient nanofiber transfer of a suitable number of fibers. The FET substrate had 1.2 μm high elevated platforms of size 1000 μm x 200 μm with predefined metal electrodes that enable direct electrical connection to the nanofibers (more information about the FET device in chapter 4 and appendix B). The FET substrate was fixed on a compliant platform and nanofibers were transferred as illustrated in Figure 3.1. Figure 3.7(a) shows the fluorescence microscope image of an array of p6P nanofibers transferred onto a transistor platform, and Figure 3.7(b) shows the growth substrate after transfer. All nanofibers within the predefined area are effectively transferred.

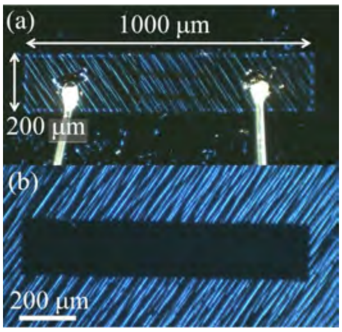

Figure 3.7: Outcome of roll printing transfer for prestructured FET substrate. Fluorescence microscope images of (a) a FET substrate with transferred nanofibers and (b) the mica substrate after nanofiber transfer.

---

[2] See the videos "As-grown_nanofibers.avi" and "Transferred_nanofibers.avi", which show as-grown and transferred nanofibers, respectively, imaged through a stationary polarizer. The videos are available either on http://onlinelibrary.wiley.com/doi/10.1002/smll.201100660/suppinfo or on the CD attached to the last page of this thesis.

3.4 Large scale transfer

In order to demonstrate the scaling possibilities of the roll printing method, nanofibers were transferred to 10 FET substrates (Figure 3.8) in one transfer step, with the number of samples essentially being limited by the size of the growth substrate. Figure 3.8(a) is an illustration of the large scale roll printing method. Figures 3.8(b) and (c) show the FET substrates with predefined electrodes and Figures 3.8(d) and (e) show FET substrates without electrodes (future top contact electrodes would be deposited). In Figure 3.8(f) it is seen that the nanofiber direction is changing. This is due to the different domains on the mica substrate, where the nanofibers' growth direction changes across a step edge (Figure 3.8(g)).

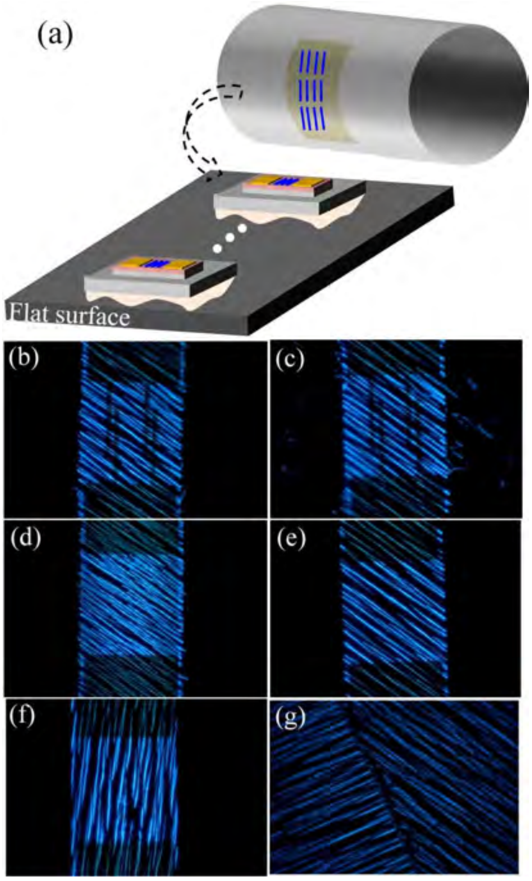

Figure 3.8: (a) Illustration of the large scale roll printing transfer technique for different FET substrates at the same step. Fluorescence microscope images after large scale transfer (b)-(c) of transistor substrates with predefined electrodes, (d)-(f) of transistor substrates without predefined electrodes, and (g) of the mica substrate with nanofibers with different growth orientations.

3.5 Summary

In this chapter, a nanofiber transfer technique was presented. This technique enables fast and destruction-free transfer of fragile organic nanostructures onto arbitrary substrates both on large-scale and on few nanoaggregate basis. AFM measurements showed the same nanofiber height and width both before and after transfer. This technique therefore gives opportunities for implementing organic functional nanomaterials into devices for new or improved functionality. In addition, transfer from one rigid substrate to another would also be possible by introducing one extra transfer step, i.e. first transferring the nanofibers from the rigid growth substrate to a flexible substrate, and then from the flexible substrate to a rigid receiver substrate. A further development could focus on a multiple printing scheme [51] for higher surface coverage or for combining different nanofiber types on the same receiver substrate for example for multicolor light sources.

Chapter 4

Electrical properties of p6P nanofibers

This chapter describes the results from a study of the electrical properties of p6P nanofibers implemented as the active material in different FET device configurations. It will begin with a general introduction to organic FETs (OFETs) and go on to describe the different nanofiber device geometries realized in this project and their resulting properties.

An OFET consists of an organic semiconducting material connected to source and drain electrodes and separated from a gate electrode by an insulating gate dielectric (Figure 4.1) [86]. Charges flow in the organic material between the source and drain electrodes, while the gate voltage modulates the conductance between source and drain [86, 87].

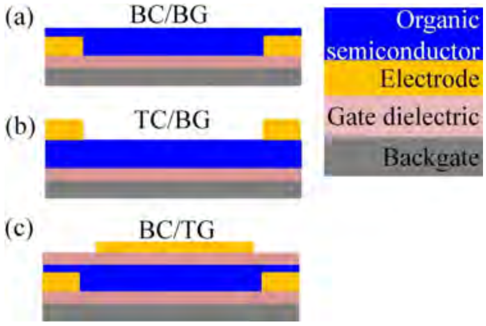

Figure 4.1: Organic field effect-transistor device configurations: (a) bottom contacts/bottom gate (BC/BG), (b) top contacts/bottom gate (TC/BG), and (c) bottom contacts/top gate (BC/TG). Adapted from [86].

The OFET type (p-type, n-type or ambipolar) is determined by the organic semiconductor and by the choice of gate dielectric and source and drain electrode materials [88, 89]. The relation between the Fermi level of the electrode material and the highest occupied molecular orbital (HOMO) and the lowest unoccupied molecular orbital (LUMO) levels of the organic semiconductor [86] gives rise to a Schottky-type energy barrier at the metal/organic interface.

Most of the organic semiconductors form p-type devices and are typically conjugated systems in which the movement of the delocalized π electrons is due to the overlap of the π-orbitals between neighboring molecules. This allows organic molecules to conduct charge carriers and behave as semiconductors [37, 91]. Such p-type semiconductors have the ability to conduct positive charge carriers when the Fermi level of source and drain metal is close to the HOMO level of the semiconductor material [86]. Among several p-type organic semiconductors are acenes [92], thiophenes [93], and phenylenes [94].

In general, organic semiconductors have low electron mobility limiting the number of n-type semiconductor materials. N-type semiconductors have the ability to conduct electrons when the Fermi level of source and drain metal is close to the LUMO level of the organic semiconductor [86]. As examples of n-type organic semiconductors are fullerens and fullerene-based materials [95, 96].

For ambipolar organic semiconductors [88, 89] both holes and electrons can be conducted. The hole and electron injection barrier is determined by the energy difference between the Fermi level of the metal source and drain electrodes and the HOMO and LUMO level of the organic material as well (Figure 4.2) [90]. However, it is still challenging to produce a device with suitable electrode material that can both inject electrons into the LUMO level and holes into the HOMO level of an organic semiconductor capable of conducting both charges [86]. One proposed solution is to use different electrode materials, so the work function of one electrode is adapted to the LUMO level of the semiconductor allowing electron injection, while the work function of the other electrode fits to the HOMO level of the semiconductor for hole injection [97].

The gate dielectric material can also influence, since the charge flow in OFETs occurs in close vicinity to the semiconductor/gate dielectric interface. Different gate dielectrics exhibit different carrier trap densities at the interface and can thereby strongly affect the charge transport. For example, it has been demonstrated that conjugated polymers, which were assumed to be a p-type material, could display n-type properties by exchanging the gate dielectric from SiO_2 to hydroxyl-free gate dielectric such as a divinyltetramethylsiloxane-bis(benzocyclobutene) derivative (BCB) [95].

The electrical characteristics of organic FETs are also known to depend on the exact transistor geometry [86, 98]. Typically one of three transistor geometries are employed: bottom contact/bottom gate (BC/BG), bottom contact/top gate (BC/TG) and top contact/bottom gate (TC/BG) (Figure 4.1) [86]. The BC/BG is known as the coplanar configuration, i.e. the source

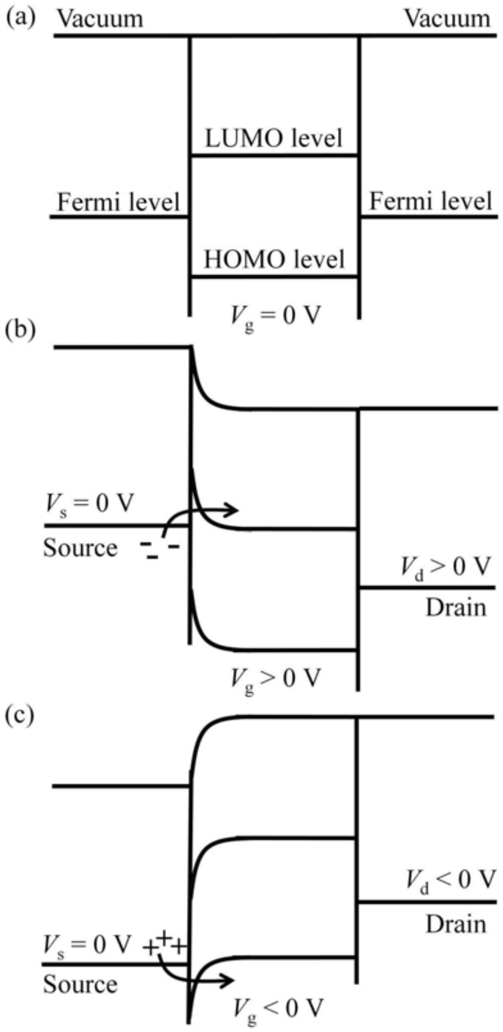

Figure 4.2: Illustration of the working principle of an ambipolar OFET. (a) Energy levels of contacts and organic semiconductor with no bias applied. When a voltage is applied to the gate (V_g), the energy levels of the semiconductor shift with the direction determined by the polarity of V_g. The application of a drain voltage (V_d) can then cause charge transport across the transistor. (b) For positive V_g and V_d, electrons can be injected from the source electrode to the LUMO of the organic semiconductor and be transported to the drain electrode. Here, the situation $V_g = V_d > 0$ V is displayed. (c) For negative V_g and V_d (here $V_g = V_d < 0$ V), holes can be injected from the source electrode to the HOMO level of the semiconductor and be transported to the drain electrode. Adapted from [90].

and drain electrodes are separated from the gate by the gate dielectric but not by the organic material (Figure 4.1(a)). The BC/BG configuration is from a device fabrication point-of-view the easiest geometry, since no further processing is required after transfer of the organic material onto the device platform, while both the TC/BG and BC/TG (Figure 4.1(b) and (c)) require additional deposition steps to form the top contacts or top gate, respectively. However, the two latter geometries (known as the staggered configurations) usually exhibit superior device performance [86]. This behavior is assumed to be due to the fact that the charges are injected not only from the edge of the electrodes (the case for a coplanar geometry) but also from the surface of the contacts due to the different electric field distributions [86].

In this work, all three device configurations have been implemented to study their influence on the nanofiber transistor performance. The top gate configuration uses a different gate dielectric material [polymethylmethacrylate (PMMA)] than the bottom gate devices [silicon dioxide (SiO_2)]. Both materials have very similar dielectric constants (3.5 and 3.9 for PMMA and SiO_2, respectively [99]) therefore the capacitance difference can easily be compensated by slightly adjusting the thickness of the gate dielectric. A difference between the gate dielectrics is the density of charge traps: $\approx 5 \times 10^8$ cm^{-2} in PMMA and $\approx 5 \times 10^{11}$ cm^{-2} in thermally grown silicon dioxide, which can influence device performance [100].

4.1 Transistor device fabrication

Silicon-based device substrates were used to integrate the nanofibers with source, drain and gate electrodes to form FET devices. The substrates included elevated platforms that were used as receiver platforms for the nanofibers to aid the nanofiber transfer. These platforms, which had a size of 1000 μm x 200 μm, were lithographically patterned on a highly n-doped silicon substrate with 200 nm thermally grown SiO_2 and realized first by HF etching through the SiO_2 layer followed by reactive ion etching 1 μm into the silicon to give a total platform height of 1.2 μm. On each receiver platform, two contact pads (390 μm x 180 μm) were prepared by photolithography, metal deposition (2 nm Ti/30 nm Au) and lift-off (Figure 4.3(a) and process recipe appendix B). Two different types of substrates were prepared to be able to prepare both bottom contact (BC) and top contact (TC) devices. The TC device substrates were ready for nanofiber transfer after the preparation of the contact pads, while the BC substrates were processed additionally with one more sequence of photolithography, metal deposition (2 nm Ti/30 nm Au), and lift-off to form small, closely spaced electrodes, which were connected to the large contact pads, and onto which the nanofibers could be connected to span the gap. Gold was chosen as the electrode material due to its inertness and due to its high work function (5.1 eV) [101] that promotes hole injection into the nanofibers. A white microscope image of the FET substrate with BC/BG configuration is shown in Figure 4.3(b).

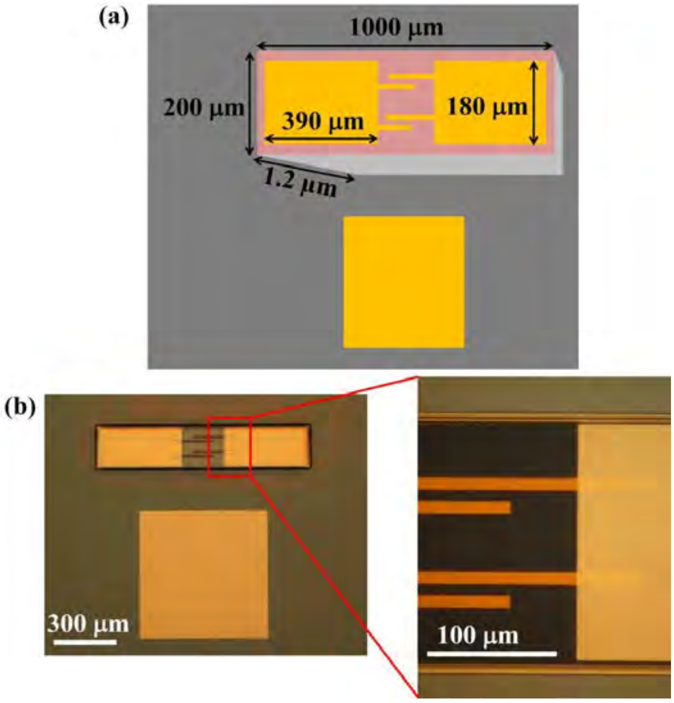

Figure 4.3: (a) Drawing with the dimension of a BC/BG FET device substrate. (b) White microscope image of the FET platform on BC/BG configuration.

The integration of the nanofibers onto the device platform took place via the roll printing transfer technique, which was described in chapter 3. After transfer, all the chips were annealed at 80°C for 20 minutes. This procedure was adopted to remove the water adsorbed during the transferring process.

4.1.1 Device configurations

Bottom contact/bottom gate device

The type 1 devices, which had a bottom contact/bottom gate (BC/BG, see Figure 4.4(a)) configuration, were ready for characterization directly after nanofiber transfer and annealing using the underlying highly doped silicon as the gate electrode. Figure 4.4(b) shows the fluorescence microscope image of the finished sample on BC/BG FET device.

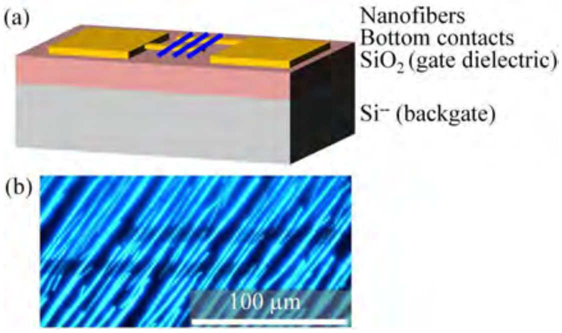

Figure 4.4: (a) Scheme of the nanofiber field effect-transistor and (b) fluorescence microscope image with BC/BG configuration.

Top contact/bottom gate device

The type 2 devices had a top contact/bottom gate configuration (TC/BG, see Figure 4.5), and were prepared by depositing gold source and drain electrodes on top of the transferred and annealed nanofibers through a nanostencil [102] with a pattern that gives top electrodes with the same dimensions as those used for the bottom contacts. In both cases, the contacts had dimensions of 10 μm x 200 μm, separated by a channel length of around 2 μm. Figure 4.5 shows an illustration of a TC/BG device with top contacts prepared by deposition through a stencil.

The nanostencils were prepared from a 525 μm thick silicon wafer coated with a 100 nm thick low-stress silicon nitride (SiN) layer. The electrode pattern was realized in the frontside SiN layer by photolithography and reactive ion etching, and the membranes were released by photolithography and etching from the wafer backside in KOH solution (28 wt% KOH concentration at 80°C for approx. 9 hours). A thin layer of photoresist was applied on the wafer frontside to protect the fragile membranes during dicing. The full process recipe is provided in appendix C [103]. After initial tests of electrode deposition onto the nanofibers through the nanostencils, it was observed that the photoluminescence spectrum of the p6P nanofibers had changed and the nanofibers had a pronounced green appearance as opposed to the clear blue colour of "perfect" nanofibers. This was attributed to the generation of defects in the nanofibers, which are known to give rise to peaks in the green part of the spectrum (see chapter 6). This could indicate that the thin SiN membrane shadow mask was too thin to protect the nanofibers against the radiation generated in the metal deposition (electron beam evaporation) system. The nanostencils were therefore coated with a thin metal layer to increase their ability to block the radiation that is expected to damage the nanofibers, and the nanofibers that were contacted using these improved nanostencils now exhibited the correct spectral appearance.

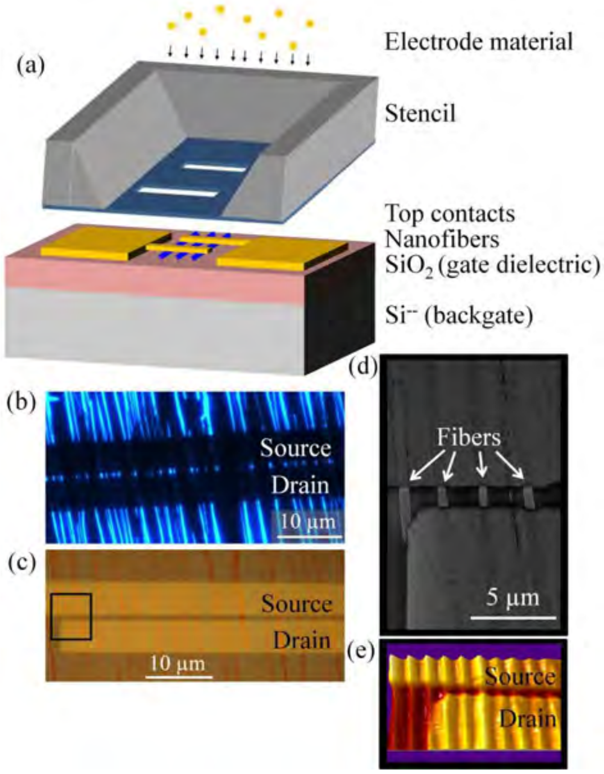

Figure 4.5: (a) Drawing of a device with TC/BG configuration prepared by deposition of the contacts through a nanostencil. (b) Fluorescence microscope image of nanofibers in top contacts configuration. (c) White microscope image of the sharp top contacts on nanofibers. (d) Scanning electron microscope, and (e) atomic force microscopy image of the electrodes connecting to the nanofibers as indicated in (c).

The completed devices were inspected using fluorescence microscopy (Figure 4.5(b)), white light microscopy (Figure 4.5(c)), scanning electron microscopy (SEM) (Figure 4.5(d)), and tapping mode atomic force microscopy (AFM) (Figure 4.5(e)). Figures 4.5 (b)-(e) show the nanofibers integrity and also the sharpness of the electrode edges on top of the nanofibers. The stencil used had 2 μm channel length but because of a blurring effect [104] during electrode deposition, a channel length of only $\approx$1.5 μm is observed in the SEM image.

Bottom contact/top gate device

The device type 3 was also a staggered configuration with bottom contacts and a top gate (BC/TG, see Figure 4.6(a)). In contrast to the bottom gate device, which used the SiO_2 layer as gate dielectric, this configuration required the application of a gate dielectric on top of the nanofibers. This was prepared by applying PMMA via spin-coating (some drops of PMMA 950 solution were rotated at 1000 rpm for 5 s followed by 8000 rpm for 45 s. Immediately after spin coating, the substrates were baked at 95°C for 4 min creating a 100-150 thick layer) onto bottom contacted nanofibers. The top gate electrode was applied by gold deposition through a nanostencil with a suitable pattern (dimensions of 120 μm x 320 μm) on top of the PMMA layer and the electrodes (Figures 4.6(a) and (b)). Tests were also performed to confirm the suitability of PMMA as gate dielectric by applying PMMA on a device substrate with BG/BC configuration without the active organic semiconductor material. Here, no electrical conduction could be observed. Investigations showed that PMMA does not alter the p6P nanofibers' electrical characteristics and that the original p6P spectrum is also preserved after coating (Figure 4.6(c) and more details in chapter 6). For the TC and TG deposition, the alignment of the SiN stencil to the device substrate was done by hand under a white light microscope.

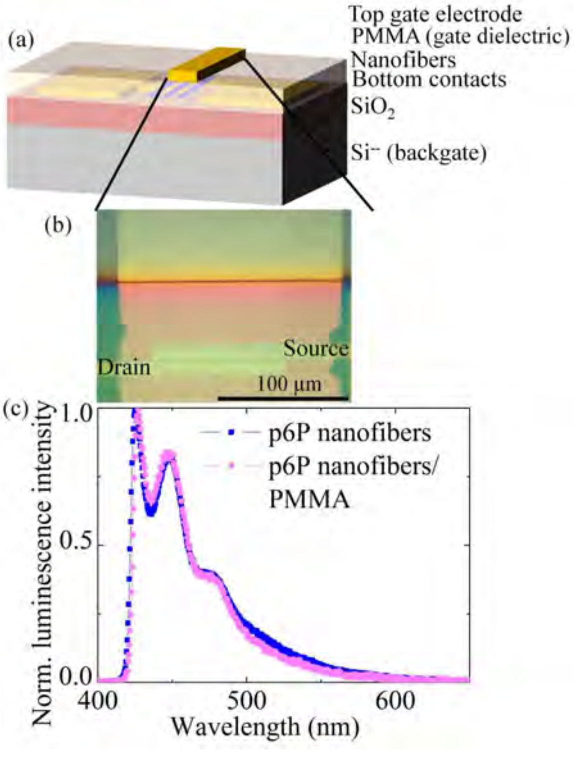

Figure 4.6: (a) Scheme of the field effect-transistor platforms on BC/TG configurations. (b) White microscope image of the BC/TG device. (c) Spectra of p6P nanofibers uncoated and coated with PMMA (λ_{ex}=365 nm).

4.2 Electrical characterization

The electrical characteristics were recorded using a probe station and a labview-controlled characterization system based on a data acquisition card and voltage and current amplifiers.

4.2.1 Nanofiber FET with BC/BG configuration

Figure 4.7(a) shows the measured transfer characteristics, i.e. current vs. gate voltage for a drain-source voltage of -15 V for p6P nanofibers on a BC/BG device. The inset in Figure 4.7(a) is the Mott-Schottky energy scheme at negative gate and drain voltages which, however, do not account for interface dipoles and traps states that could further alter the current. The source-drain electric field allows only holes injected from the source electrode or electrons injected from the drain electrode to pass through the device and the measured characteristics clearly show that the transport is p-type, i.e. holes are injected from the source (see Figure 4.7(a) inset).

Figure 4.7(b) shows the current vs. drain-source voltage for zero gate voltage for the same device. The inset schematically shows the energy level positions: the work function levels for the gold drain and source electrodes and the LUMO and HOMO levels for p6P. In Figure 4.7(b), current flow is observed only for positive source-drain voltage (V_{ds}). This must mean that the electrical characteristics are dominated by an injection barrier between the injecting metal electrode and the organic material. This is not unexpected given the energy levels shown in the inset that suggest an injection barrier for holes of around 0.9 eV. As shown in Figure 4.7(d), a positive V_{ds} then leads to downwards band bending near the drain electrode and thereby a lowering of the hole injection barrier, while a negative V_{ds} does not cause a similar band bending at the source electrode as would be required for hole injection in the opposite direction since the band bending again occurs at the drain electrode (see Figure 4.7(c)). A hysteresis effect can also be observed in Figure 4.7(b) where the forward sweep is higher than the reverse sweep. This is assumed to be caused by trapping of the charge carriers [86, 95, 105]. The observed hysteresis is presumably due to hole trapping close to the interface region between the injecting electrode and the organic material creating a space charge that reduces the band bending and thereby limits further hole injection, causing a lower back sweep current. This aspect will be elaborated on below.

4.2.2 Comparison to other device configurations

Figure 4.8 shows current vs. drain-source voltage for zero gate voltage for the three different configurations, while the inset shows the same data plotted with a different current scale. Approximately the same number of

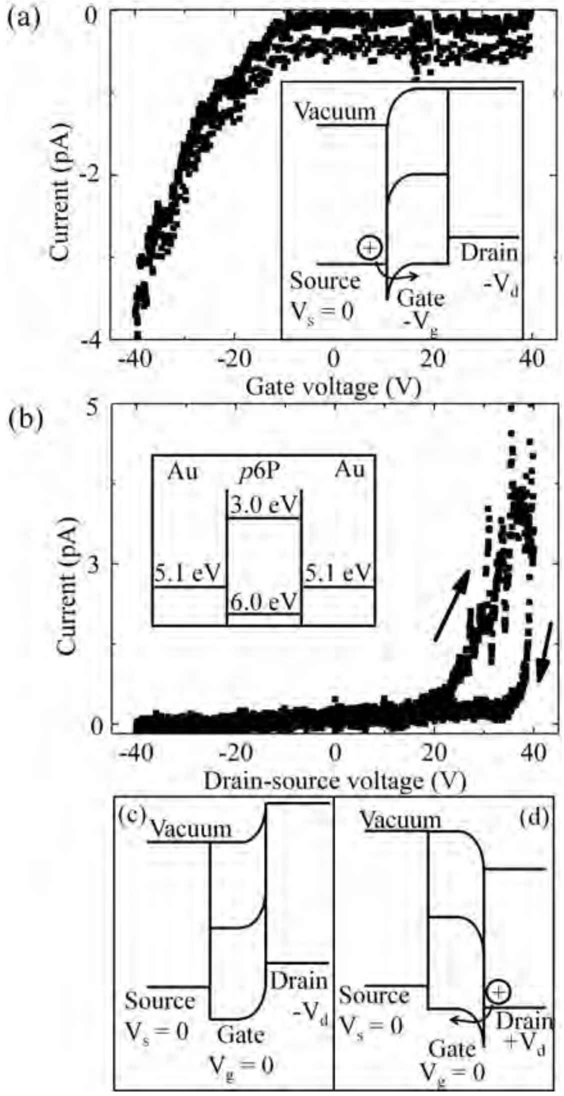

Figure 4.7: Measured transistor characteristics for BC/BG nanofibers. (a) Current versus gate voltage for V_{ds} = -15 V. Inset shows schematic Mott-Schottky energy scheme for negative gate and drain voltages. (b) Current versus drain-source voltage for zero gate voltage. Arrows indicate the sweep direction. Inset shows energy level positions: the work function level for the gold drain and source electrodes (5.1 eV) and the LUMO (3.0 eV) and HOMO (6.0 eV) levels for p6P. (c) Mott-Schottky energy scheme for zero gate voltage and negative drain voltage. (d) Mott-Schottky energy scheme for zero gate voltage and positive drain voltage.

nanofibers were present in all the samples, i.e. the cross-section areas were approximately the same. The coplanar (BC/BG) configuration exhibits a lower output current than the staggered geometries due to a high contact resistance associated with the high injection barrier to the organic material [106]. In the staggered geometries (BC/TG and TC/BG) the charges are injected not only from the edge of the electrode but also from the surface of the contacts in the region where the source-drain electrodes overlap with the gate electrode and consequently charges are injected over a larger area leading to a lower contact resistance than in the coplanar (BC/BG) geometry [86].

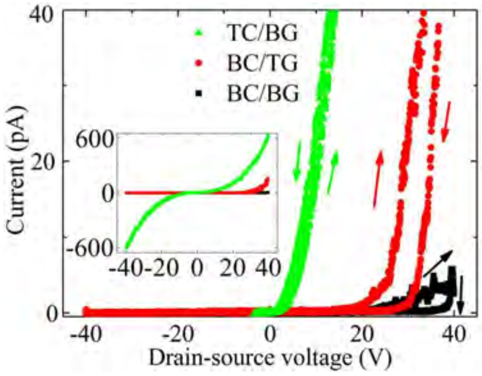

Figure 4.8: Current versus drain-source voltage for zero gate voltage for p6P nanofibers in BC/BG, BC/TG, and TC/BG. Inset shows the same data with a different current scale.

The TC/BG configuration exhibits the highest output current. It is presumably due to the smaller contact resistance between the nanofibers and electrodes due to deposition of the electrodes under vacuum, which prevents water residues in the nanofiber/electrode interface in contrast to the bottom contact devices where the nanofiber/electrode interface is created under humid conditions during the transfer. As suggested by Bao and coworkers [107], moisture residing at the interface between the electrode and the organic material is expected to cause an increased contact resistance. Although our devices are annealed after fabrication, this can presumably not eliminate all water or water transferred contaminants residing at the interface, since hysteresis is observed even after prolonged annealing. Also, metal penetrating into the organic material during electrode deposition can enable a better electrical contact for TC devices [108, 109].

The symmetric characteristics of the TC/BG device as opposed to the asymmetric behavior of the bottom connected devices can be observed in the inset of Figure 4.8. Since no n-type behavior has been observed, this must mean that in the TC/BG devices, the source electrode is injecting holes for negative drain-source voltages. The situation depicted in Figure 4.7(c) with band bending at the drain electrode is thus not valid for the top contact devices. Here, the main current limiting factor is the bulk nanofiber resistance giving rise to the observed symmetric output curve. In Figure 4.8, essentially no hysteresis is observed for the TC/BG configuration. Since these output characteristics are dominated by the nanofiber bulk as described previously, this suggests that the traps that cause the hysteresis must be spatially located near the injection region that governs the behavior of the BC devices.

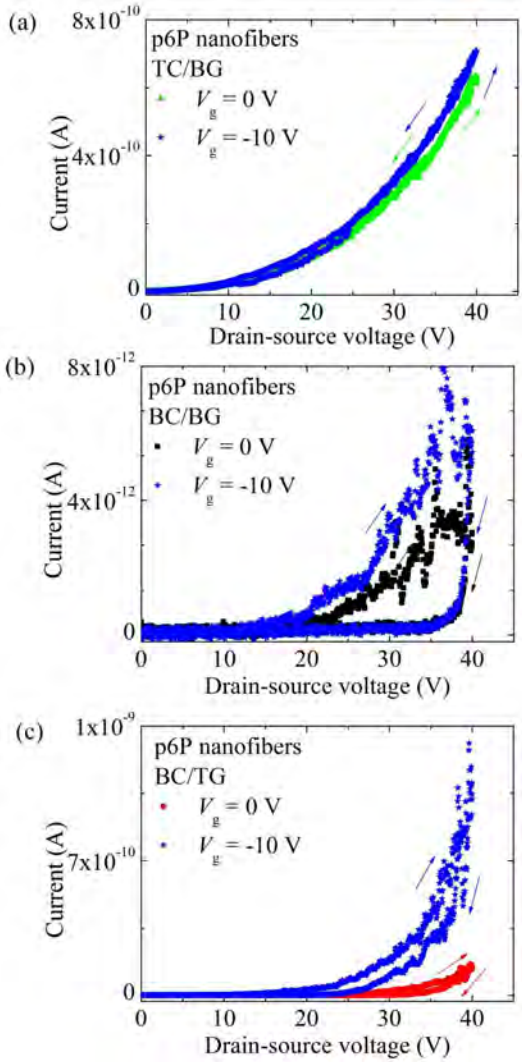

Figure 4.9: Current vs. drain-source voltage for $V_g = 0$ V and -10 V for p6P nanofiber FETs with (a) TC/BG, (b) BC/BG and (c) BC/TG configurations.

Figure 4.9 shows current vs. drain-source voltage for V_g = 0 V and -10 V for the three different configurations. In all cases the current starts to flow at lower V_{ds} and the current intensity is larger for the more negative V_g value. The TC/BG is expected to show nanofibers bulk properties, which are not modified significantly by a gate voltage at least in the range 0 → -10 V (Figure 4.9(a)). The BC/BG (Figure 4.9(b)) and BC/TG (Figure 4.9(c)) configurations both show contact resistance characteristics, which are more strongly affected by a gate voltage (lowering of the barrier for hole injection by a negative gate voltage), however, as it is expected in the staggered geometry (BC/TG) the gate effect is more pronounced due to the larger overlap area between electrodes and gate. The different hysteresis observed in the bottom contact configurations (Figures 4.9(b) and (c)) can be due to the dissimilar charge trapping characteristics for the different gate dielectrics.

Figure 4.10 shows the transfer characteristics, i.e. the current as function of gate voltage for V_{ds} = -15 V. From the data in Figure 4.10, the subthreshold swing ($S = dV_g/d(logI_{ds})$ [110]) was obtained from the p6P nanofibers on different transistor configurations to elaborate on the switching behavior. The subthreshold swing (S) was found to be 13.7, 9.5 and 7.5 V/decade, for BC/BG, BC/TG, and TC/BG configurations, respectively. The TC/BG configuration exhibits the lowest subthreshold swing being almost half that of the BC/BG device. For comparison, Klauk et al. [111] have studied the electrical characteristics for pentacene transistors with 100 nm SiO_2 as the gate dielectric and found a subthreshold swing of only 0.7 V/decade. Here, the results are around a decade above this, however, this is not unexpected since the p6P mobility is significantly below that found in pentacene [94, 111] and since the device geometry (here particularly the gate dielectric thickness) was not optimized for efficient switching.

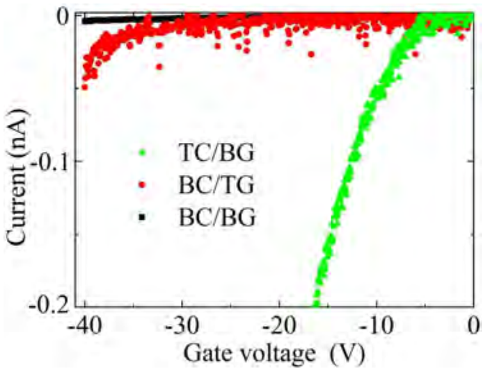

Figure 4.10: Current versus gate voltage at V_{ds} = -15 V for p6P nanofibers transferred from mica to transistor platforms in BC/BG, BC/TG, and TC/BG configurations.

4.2.3 Comparison between p6P nanofibers and thin films

In addition to the nanofiber devices, p6P thin film devices [78] were also prepared for comparison of the electrical properties of crystalline nanofibers and more unordered thin films. The preparation method was identical with the exception of the nanofiber transfer step being replaced by vapour deposition of the p6P molecules directly onto the device substrates at room temperature resulting in a structure-less film.

Figure 4.11 shows the output characteristics for a 30 nm thick p6P film on similar transistor platforms. Around 8 times more material was used to form the films compared to the material used to grow the nanofibers. In Figure 4.8 and 4.11 the higher current density for the p6P nanofibers in comparison with the film must be consequence of the crystallinity of the nanofibers, i.e. p6P nanofibers have a long range order compared with thin films which is believed to favor a high charge-carrier mobility as a result of the π-conjugated coupling between the packed molecules [37]. The asymmetric curve observed for the thin film FET also in the TC/BG configuration in Figure 4.11 must be the result of a high contact resistance compared to the resistance of the film bulk. This implies that the contact resistance in TC devices is significantly lower for the crystalline nanofibers than for the unordered film. In addition, the significant hysteresis observed for the injection limited thin film devices further support our conclusion of the traps being spatially located close to the metal/organic interface.

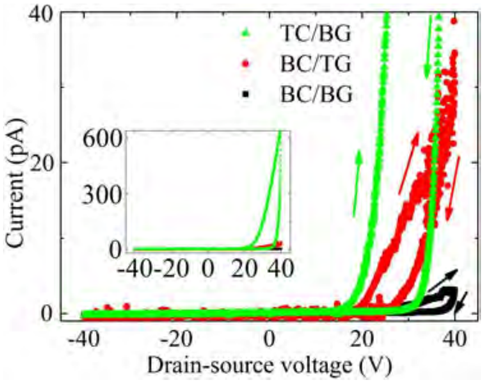

Figure 4.11: Current versus drain-source voltage for zero gate voltage for p6P thin films in BC/BG, BC/TG and TC/BG configurations (compare with Figure 4.8).

In Figures 4.8 and 4.11, a drain current saturation is not observed. The channel length used was around 2 μm and the gate dielectric was 0.2 μm thick. It is well-known that if the channel length of a transistor is less than 10 times the thickness of the gate dielectric, the space-charge-limited bulk current will be dominated by the lateral field due to the source-drain voltage preventing saturation since the gate voltage will not determine the charge distribution within the channel and consequently the ”on” or ”off” state of the transistor will not be observed [86].

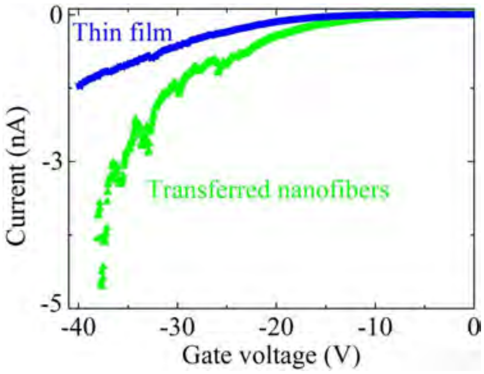

Figure 4.12: Current versus gate voltage at V_{ds} = -15 V for p6P nanofibers and thin films in TC/BG configuration.

Figure 4.12 shows the transfer characteristics at V_{ds} = -15 V for both p6P nanofibers and thin film. Figure 4.12 shows that the nanofibers conduct better than the thin films (as mentioned previously the film cross-sectional area is around 8 times the nanofiber cross-section) and current saturation is not observed reinforcing the conclusion from Figure 4.8.

4.3 Summary

In this chapter, integration of transferred organic nanofibers on different field-effect transistor platform configurations has been demonstrated. The different FET devices have been electrically characterized to reveal the significant differences in electrical performance between the different configurations. The coplanar device geometry has a high contact resistance and consequently a poor conduction compared to the staggered geometries. Within the staggered geometries, the top contact geometry shows superior performance to the bottom contact geometry presumably due to a cleaner interface between the contact and the organic material and due to metal penetration into the organic material during contact electrode deposition. The better electrical connection of the top contacts results in the nanofiber transistor output characteristics being dominated by the nanofiber bulk as opposed to the bottom contact devices which exhibit injection limited behavior. A direct comparison of the crystalline p6P nanofibers with unordered thin films shows that both materials exhibit p-type behavior but the fibers conduct significantly better owing to their better crystallinity.

Such electrically contacted organic nanostructures can have a range of applications, notably as nanoscale organic light emitters. These can be realized in similar field-effect transistor configurations and are therefore the next subject to be studied. The performance of such organic transistors is influenced by a range of factors and optimization can therefore be pursued for example by using other gate dielectrics [87], electrode materials [112], and by implementing nanofibers from other molecules [30].

Chapter 5

Electroluminescence from p6P nanofibers

The use of a FET device configuration for electroluminescence experiments is convenient since it enables the fabrication of organic light-emitting field-effect transistors (OLEFETs) with more accurate tuning of the charge injection and transport compared to the diode configuration [113]. Light emission from an OLEFET device was demonstrated for the first time by Hepp *et al.* [114] using tetracene as the light-emitting material. This resulted in an unipolar device, in which one type of charge carriers were flowing across the transistor channel and recombined with the opposite charge carrier type just next to the electrode causing the light emissiom to occur from there. Zaumseil *et al.* [115] demonstrated the movement of the light emission region within the transistor channel by varying the applied gate and source-drain bias. This was possible due to the transport of both holes and electrons at the semiconductor/dielectric interface, i.e. this constituted an ambipolar organic transistor. By varying the applied voltages, the charge accumulation region could be extended further into the channel and consequently the recombination and emission zone was then moved within the channel. Capelli *et al.* [116] have shown that a multilayer system of organic materials can generate highly efficient devices. In this case, instead of an ambipolar material, n-type and p-type organic layers were separated from each other by a light-emitting host-guest organic layer. Such a heterostructure can enable OLEFET devices with an external quantum efficiency (EQE) higher than a similar OLED. In addition, Yamao *et al.* [117] showed that biasing an OFET device with an AC voltage applied to the gate causes higher emission intensity than using a DC scheme. Different from DC biasing where an injection barrier may hinder the injection of charges from the electrode into the HOMO/LUMO levels of the organic material, with an AC gate modulation and source-drain symmetrically biased, the barriers for hole (electron) injection is reduced in the negative (positive) half-cycles of the gate signal.

Nanoscale organic light-sources have so far only been demonstrated based on patterning the emission zone by e-beam lithography [118, 119]. The Lidzey group showed that by structuring the charge injection electrodes with electron beam lithography before applying the organic layer, it is possible to fabricate individually addressable pixels with dimensions of ≈200 nm [120].

In this chapter, it is shown how the application of an AC voltage to the transistor gate electrode causes sequential injection of holes and electrons into the organic material where the charge carriers recombine radiatively, which stimulates localized and polarized blue electroluminescence (EL) from the p6P nanofibers. In addition, it is shown how the nanofibers' morphology enables them to function as subwavelength optical waveguides.

5.1 Light-emitting transistor device

The FET device substrates were prepared by lithography, metal deposition, and lift-off as described in appendix B but with different lithographic masks. Here, an interdigited electrode array was patterned (see Figure 5.1) on 300 nm thick, thermally grown SiO_2. The nanofibers were transferred for these devices via roll printing as described in chapter 3. After transfer, the samples were annealed at 80°C for 20 min.

Figure 5.1 shows the light-emitting FET device substrate with a transferred nanofiber and the biasing scheme as well. It includes an AC voltage applied to the gate (V_g=V_0·sin($2\pi ft$)) while source and drain electrodes are either symmetrically biased by a DC voltage or grounded.

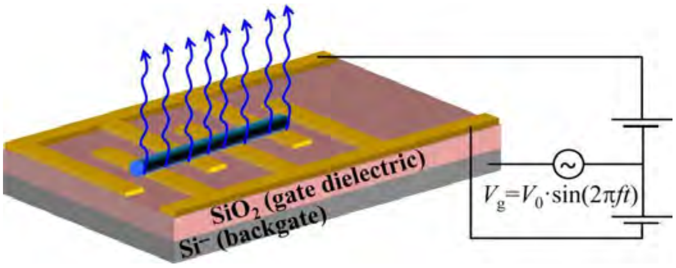

Figure 5.1: Schematic drawing of the FET device substrate including a transferred nanofiber and the biasing scheme.

5.2 Electroluminescence and morphology characterization

Figure 5.2(a) is a tapping-mode AFM image of the nanofibers integrated onto a FET substrate. These fibers are approx. 40 nm high and 900 nm wide and are bridging the metal electrodes separated by a distance of around 10 μm. Figure 5.2(b) shows a fluorescence microscope image of the same area as displayed in Figure 5.2(a).

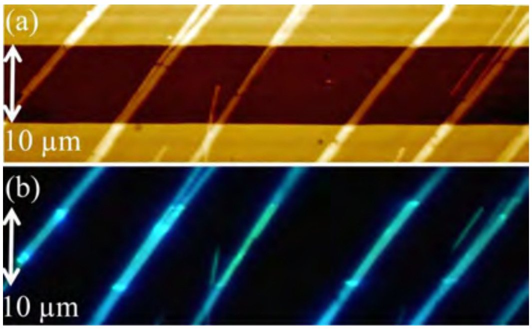

Figure 5.2: (a) AFM image and (b) fluorescence microscope image of nanofibers transferred onto a FET device substrate.

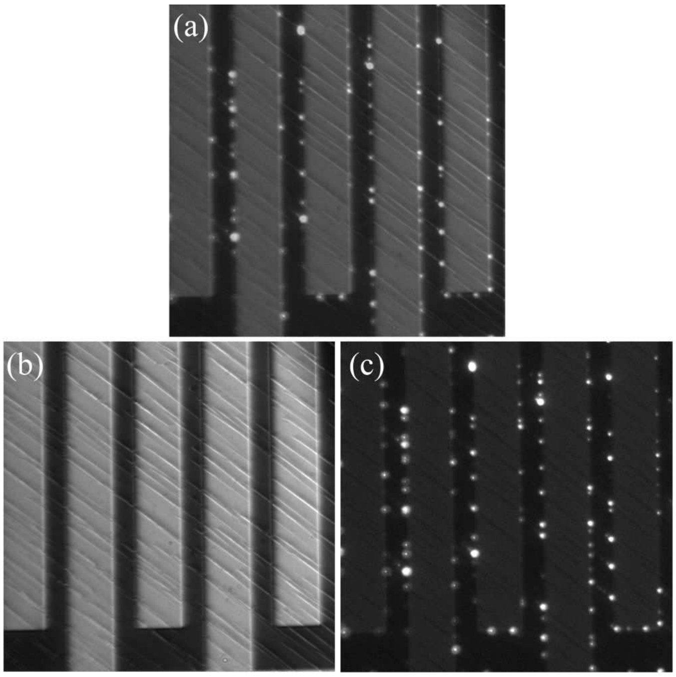

Figure 5.3: (a) Overlay of the image 5.3(b) and 5.3(c). (b) Optical microscope image with light on to show electrode and nanofiber positions. (c) Electroluminescence (EL) microscope image (f = 200 kHz, V_0 = 62.5 V, V_d = V_s = 0 V) with light off.

Figure 5.3(a) shows highly localized light emission from the p6P nanofibers at the positions where the nanofibers connect to the metal electrodes. The image is a superposition of a standard white light microscope image (Figure 5.3(b)) to show the exact position of the emission zones relative to the electrodes and nanofibers and an optical microscope image (Figure 5.3(c)) of the biased device without any external lighting. The microscope images were collected using an EMCCD camera coupled to a Navitar microscope system while the sample was kept in vacuum conditions of around 10^{-4} mbar. The electroluminescence (EL) image in Figure 5.3(c) was captured while applying a sinusoidal gate voltage with an amplitude of 62.5 V and a frequency of 200 kHz while the source and drain electrodes were grounded ($V_d = V_s = 0$ V). Experiments with a similar gate voltage and a symmetrical biasing of the source and drain electrodes (V_d = -V_s) up to 40 volts showed essentially the same result.

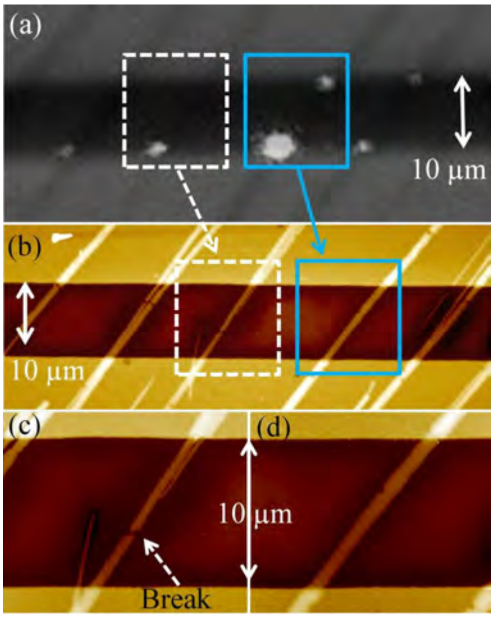

Figure 5.4: (a) Overlay image of (1) optical microscope image with light on to show electrode and nanofiber positions and (2) EL microscope image (f = 200 kHz, V_0 = 62.5 V, $V_d = V_s = 0$ V) in which full scale corresponds to an EL intensity of around 3×10^{-7} W cm^{-2} (appendix D). (b) AFM image of the nanofibers showed in (a) after EL experiments. The AFM image of the same nanofibers was made before the EL experiments and are presented in Figure 5.2(a). (c,d) Magnified AFM images of the indicated parts in (b).

Figure 5.4(a) shows a superposition of an optical microscope image of the biased device (without any external lightning) and a standard white light microscope image as it is exemplified in Figure 5.3. The EL emission was captured while applying a sinusoidal gate voltage with an amplitude of 62.5 V and a frequency of 200 kHz. Figure 5.4(b) shows AFM image of the nanofibers in Figure 5.2(a) after the EL measurements. Figures 5.4(c) and (d) show two nanofibers indicated in Figure 5.4(b). These two selected fibers are bridging the metal electrodes separated by a distance of around 10 μm. One of the nanofibers has a break indicated with an arrow (see Figure 5.4(c)) and consequently it is connecting to only one electrode. The other nanofiber is crossing two electrodes without any breaks (see Figure 5.4(d)). Despite of the break in the fiber in Figure 5.4(c) EL can still be observed from one side of the fiber (Figure 5.4(a)). No EL can be observed from the other side of the fiber (Figures 5.4(a) and (c)) presumably due the electrical contact at the metal/nanofiber interface. This point will be elaborated below.

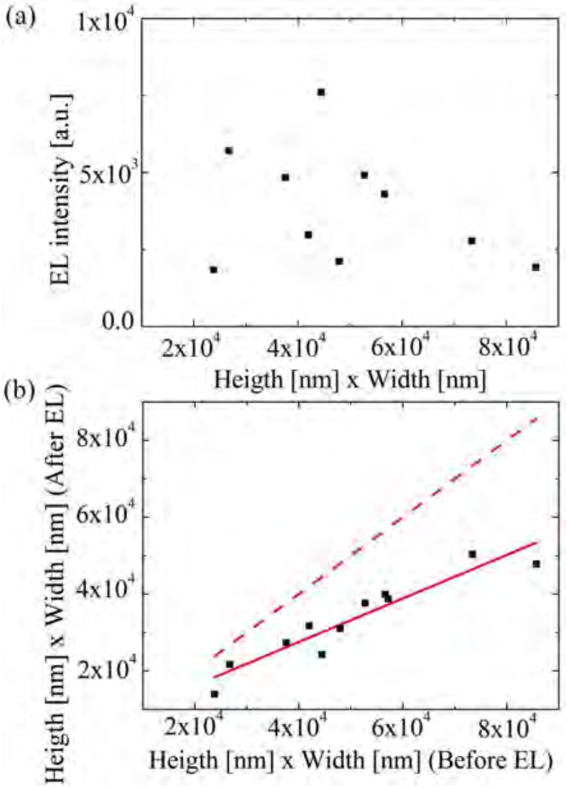

Figure 5.5: (a) Correlation between EL intensity and the nanofibers' cross-section before light emission experiments. (b) Nanofibers' size before (see Figure 5.2(a)) vs. nanofibers' size after (see Figure 5.4(b)) EL experiments. Solid line is a linear fit to the data points. For comparison, the dashed line indicates the situation where no volume reduction had occured.

The same nanofibers were examined by AFM both before (Figure 5.2(a)) and after (Figure 5.4(b)-(d) and additional data not shown) light-emission to investigate if any changes in the fibers' morphology occurred and to check whether the observed very different intensities for different metal/nanofiber interfaces are related to the nanofibers' size or to the contact between nanofiber/metal electrode. No clear correlation between EL intensity and the nanofibers' volume was observed (Figure 5.5(a)). In addition, the AFM data show that all the nanofibers, even those with no (or below detection threshold) light-emission suffered volume reduction of more than 40% after measurements of several minutes (Figure 5.5(b)). Extra material between the nanofibers after light-emission experiments were observed as it can be seen from the line scan from the AFM images in Figure 5.6. The volume reduction could be related to material ablation caused by the high electric field strength, and could have caused material accumulation between the electrodes as it is shown in Figure 5.6. Presumably, the light intensity depends rather on the electrical contact at the metal/nanofiber interface since it could be observed that the light emission intensity was fluctuating significantly for samples that had not been annealed. Annealing has previously been shown to alter the electrical contact significantly (chapter 4), since in nominally identical samples, the quality of electrical contact between an organic crystal and a metal electrode can vary strongly [121], the light emission intensity is similarly expected to vary between different nanofibers.

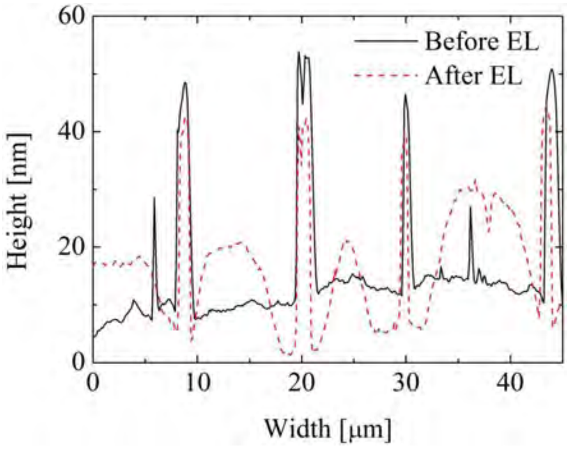

Figure 5.6: AFM line scan of the nanofibers and the region between them in the gap between the electrodes on the FET device before (see Figure 5.2(a)) and after (see Figure 5.4(b)) light-emission experiments.

Figure 5.7 shows device lifetime by monitoring the EL intensity vs. time under vacuum conditions of around 10^{-1} mbar and constant biasing conditions of f = 150 kHz and V_0 = 62.5 V. The intensity drops via a multiexponential decay with an initial fast decay by 40% within the first five minutes followed by a slower decay with a time constant of around 30 min. Since a multiexponential intensity decay has been observed during UV-photobleaching experiments on p6P nanofibers [80], this indicates that similar reactions occur in both processes.

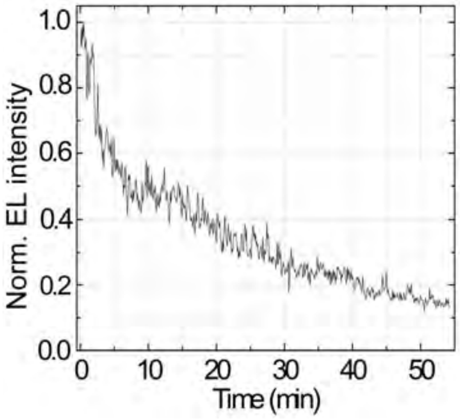

Figure 5.7: Integrated EL intensity decay during light emission experiments with f = 150 kHz, V_0 = 62.5 V, and $V_d = V_s$ = 0 V.

5.3 Operating mechanism

It can be observed from Figure 5.4 that even if a nanofiber is not connecting to both source and drain electrodes it can emit light, i.e. there is no charge transport across the channel involved in the light generation process here in contrast to the situation in conventional unipolar OLEFETs [122]. Rather, when an AC gate voltage is applied to the device, holes and electrons are sequentially injected from the same metal electrode into the organic semiconductor and are not transported along the nanofiber, i.e. they remain in close proximity of the injection electrode until the opposite charge carrier is injected causing formation of excitons and light emission. This is in agreement with the situation in p6P thin film devices: during the negative half-period of the gate voltage, holes are injected from the metal electrode and trapped in the organic material. In the other half-period when the voltage is positive, electrons are injected and the recombination of the charges then generates light emission (Figure 5.8(a)) [123, 124].

Figure 5.8(b) shows the dependence of the EL intensity on the gate voltage frequency. The apparent linear relationship reflects that each period of the gate voltage causes a certain amount of photons to be emitted (at sufficiently low frequencies). The dependence of the EL intensity on the gate voltage amplitude is shown in Figure 5.8(c). The superlinear behavior

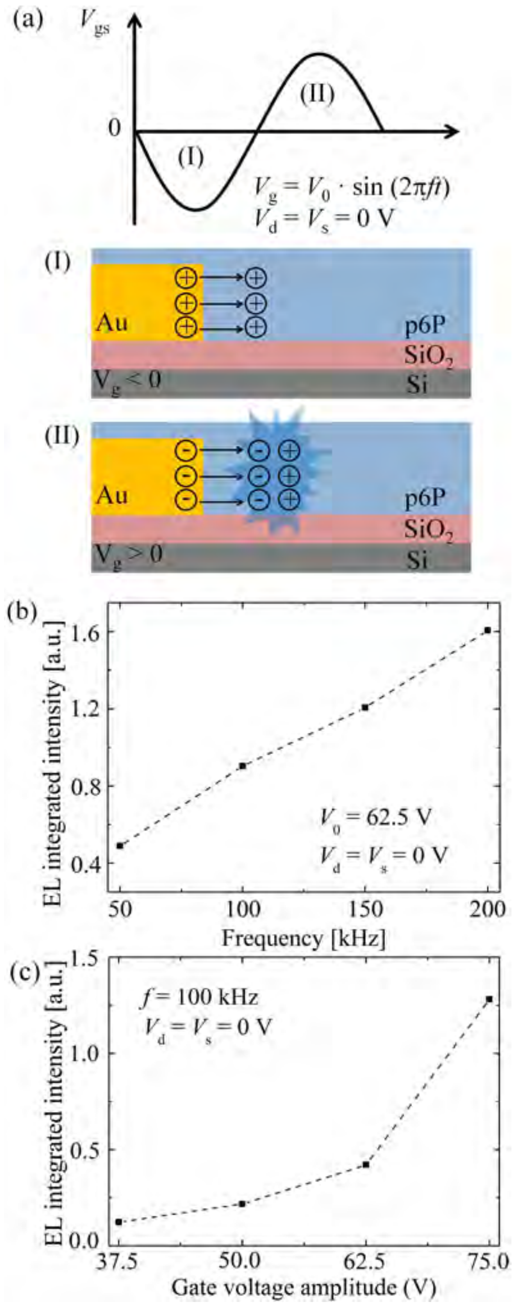

Figure 5.8: (a) Schematic drawing of time sequence for light generation. (b) EL intensity versus AC frequency. (c) EL intensity versus AC gate amplitude. Data in (b) and (c) have been obtained from different samples and the absolute intensity values are therefore not directly comparable.

is due to a non-linear relation between the charge carrier injection rate and the voltage when injection takes place over a Schottky-like energy barrier, where a more exponential-like behavior is observed for p6P-gold interfaces [125]. This agrees well with previous studies on OLEFETs based on p6P thin films [126].

5.4 Spectral and polarization properties

In order to confirm that the observed light indeed is EL, the spectrum of the emitted light was measured. Figure 5.9 shows the normalized EL and photoluminescence (PL) spectra. The EL spectrum was acquired by applying an AC gate voltage with amplitude 75 V and frequency of 200 kHz while the PL excitation was done using a HeCd laser with wavelength of 325 nm and in both cases recording the spectrum with a cooled CCD array-based spectrometer. The characteristic peaks from the p6P nanofibers are clearly at the same position for both spectra confirming that the observed light is indeed EL coming from the p6P nanofibers. The EL spectrum has a broad peak at longer wavelengths that is, however, also visible in the PL spectrum with a lower intensity. A possible explanation is that while the EL originates from a small part of the nanofibers very close to the electrode edge, where structural defect might have been introduced during transfer, the PL is sampled from the whole nanofiber area. The dips at around 550 nm and 625 nm are due to automatically subtracted background.

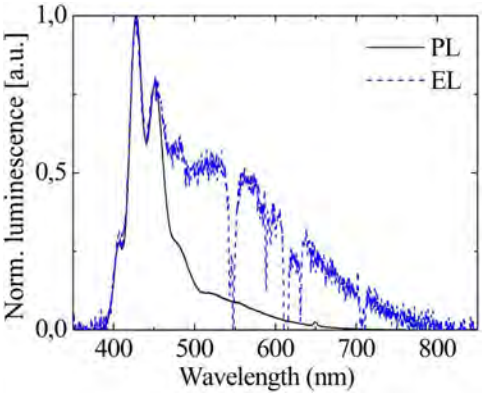

Figure 5.9: Comparison between EL and PL spectra from the p6P nanofibers.

Figures 5.10(a) and (b) show the light emission detected with a polarizer inserted in front of the microscope. The p6P nanofibers emit highly polarized light under UV excitation because the emitting dipoles are oriented along the molecules' long axes, which are mutually parallel in the herringbone packed crystalline nanofibers [64]. The transmitting axis of the polarizer in Figure 5.10(a) is parallel (±10°) to the long axis of the nanofibers and in Figure 5.10(b) it is perpendicular (±10°) to the fibers. The integrated EL (bias parameters: f = 200 kHz, V_0 = 75 V, V_d = V_s = 0 V) intensity in Figure 5.10(b) is around 3 times more intense than the integrated EL intensity observed in Figure 5.10(a) showing that the EL emission is polarized and thereby demonstrating that the molecular ordering is to a large extent maintained in the transferred nanofibers.

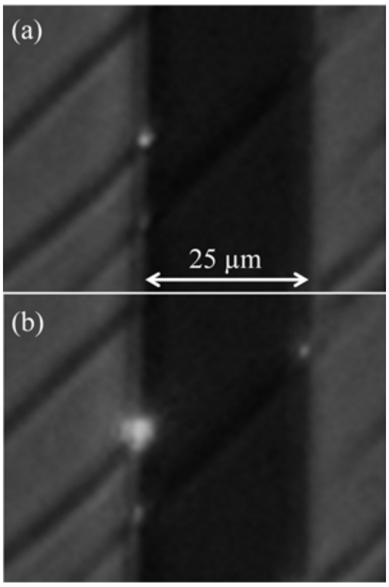

Figure 5.10: Polarization. Overlay image of (1) optical microscope image with light on to show electrode and nanofiber positions and (2) EL microscope image (f = 200 kHz, V_0 = 75 V, V_d = V_s = 0 V) with polarizer (a) parallel (±10°) and (b) perpendicular (±10°) to the long nanofibers axis. Full scale corresponds to an EL intensity of around 1×10^{-6} W cm^{-2} (see appendix D).

5.5 Waveguiding of electroluminescence

The waveguiding property of the nanofibers has previously been demonstrated by the observation of the radiation of light from a break in a nanofiber, in which photoluminescence was excited locally at a position several tens of micrometers away from the break [73]. A part of this PL was launched into a guided mode of the nanofiber and radiated at the nanofiber break with the intensity of the guided light decreasing with distance along the waveguide due to reabsorption [73]. In Figure 5.11, waveguiding of electrically stimulated light in the p6P nanofibers is demonstrated. Figures 5.11(a) and (b) show the EL image of a sample with several nanofibers on electrodes separated by a 25 μm gap. The images were recorded with bias parameters: $f = 200$ kHz, $V_0 = 62.5$ V and $V_d = V_s = 0$ V. In addition to the bright spots at the electrode/nanofiber interfaces, a spot (indicated with an arrow) can be observed between the electrodes. Figures 5.11(c) and (d) show AFM images and Figures 5.11(e) and (f) show fluorescence microscope images, respectively, of the areas indicated in Figures 5.11(a) and (b). The position of the indicated bright spots in Figures 5.11(a),(b) corresponds exactly to the position of the breaks in the nanofibers morphology as seen in the AFM images. The fluorescence microscope images confirm the waveguiding ability of these particular nanofibers as an increased intensity is observed at the breaks. This confirms that the bright spots indicated in Figure 5.11(a),(b) indeed are light that is generated at the adjacent nanofiber/metal interface and guided along the nanofiber. In Figure 5.11(a), the nanofiber dimensions are approx. 55 nm height and approx. 740 nm width and the break in the nanofiber is approx. 10.4 μm distant from the electrode/nanofiber interface. In Figure 5.11(b), the nanofiber dimensions are approx. 66 nm height and approx. 600 nm width and the break in the nanofiber is approx. 13.6 μm distant from the electrode/nanofiber interface.

Since the intensity of the waveguided EL is quite weak, it is necessary to use long acquisition time when recording the EL images, which cause saturation of some of the brighter EL spots in the image. Figure 5.12(a) shows an intensity profile along the nanofibers shown in Figures 5.11(a) and (b). In Figure 5.12(a) the dashed lines are the raw data from which the camera saturation can be observed and the solid lines are the fitted Gaussian peaks (using PeakFit software). The fitting was done to estimate the total intensity of the saturated spots at the metal/nanofiber interfaces.

Balzer *et al.* [73] showed how the waveguiding behavior can be quantified by equation (5.1), which predicts an exponential decay of the guided intensity with distance.

$$I(z) = I(z_0)exp[2Im(\beta(z - z_0))] \tag{5.1}$$

where z_0 is the excitation point and z is the distance along the nanofiber from the excitation point. $I(z)$ is the intensity of the guided light as a function of position. β is the propagation constant and $Im(\beta)$ is the imaginary part of β.

In these experiments, which used light stimulated by PL, the propagation constant β was found by studying the damping when the distance between the excitation point and the scattering point was varied. This was done by simply translating the excitation point.

For a guided wave excited by EL (Figures 5.11(a) and (b)) the movement

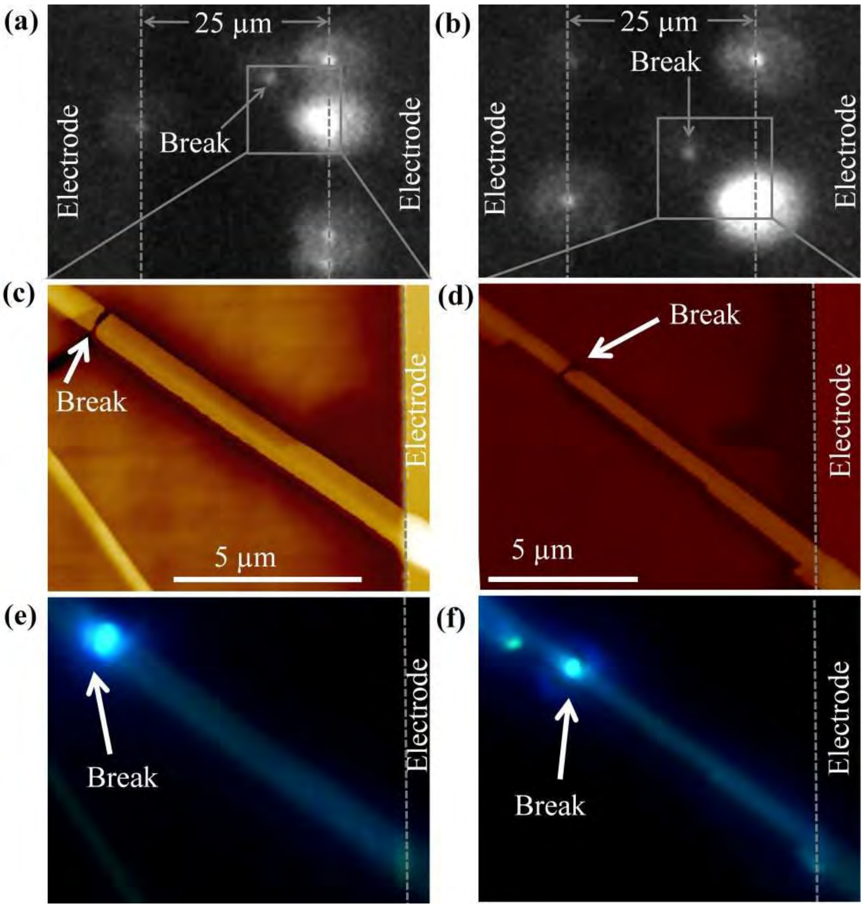

Figure 5.11: Waveguiding. (a,b) Electroluminescence image of the nanofibers with f = 200 kHz, V_0 = 62.5 V and also $V_d = V_s = 0$ V in which full scale corresponds to an EL intensity of around 1×10^{-6} W cm^{-2} (appendix D). (c,d) AFM images. (e,f) Fluorescence microscope images.

of the excitation point is not possible. A comparison of the damping therefore requires the use of several nanofibers with breaks at different distances from the nanofiber/electrode interface.

Figure 5.12(b) shows the intensity of the waveguided emission for the two different nanofibers in Figures 5.11(a) and (b) on a normalized plot. The normalization is done to be able to compare the intensities, since the emission intensities at different nanofiber/electrode interfaces are dissimilar. It should, however, be noted that the $I(z_0)$ in equation (5.1) is the intensity of the guided light at position z_0 while what is measured is not the guided light but rather the light that is scattered out of the fiber at position z_0. The analysis here therefore assumes that there is a constant factor between

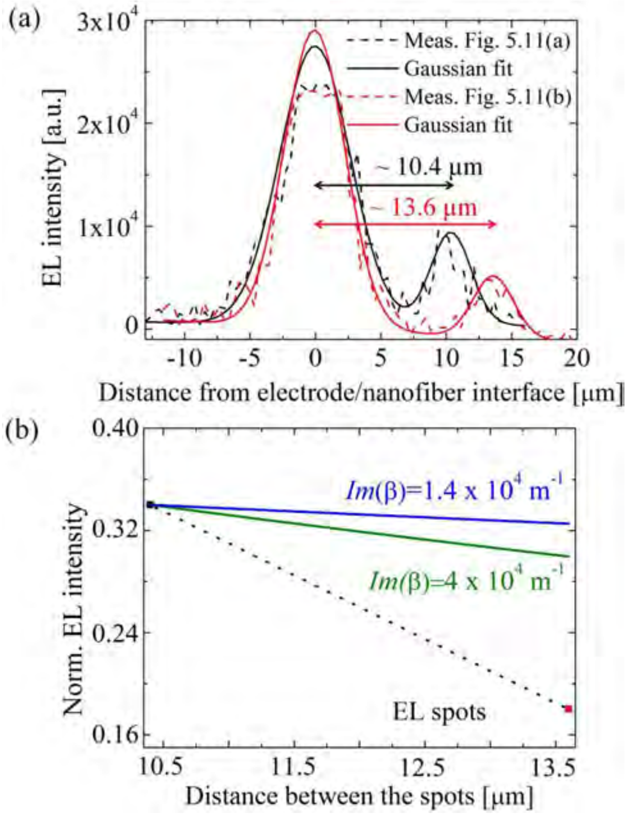

Figure 5.12: (a) Intensity profile along the nanofibers in Figure 5.11(a) and (b). (b) Dotted line shows normalized intensity of the waveguided emission for the two different nanofibers in Figures 5.11(a) and (b).

the light that is scattered out of the fiber and the light that is launched into a guided mode.

Previous waveguiding experiments have provided a range of values for the propagation constant $Im(\beta)$ between 1.4×10^4 m^{-1} and 4.0×10^4 m^{-1} (see appendix E). The two solid lines in Figure 5.12(b) are exponential curves that pass through the first EL data point from the light scaterred from the break and have exponential factors equal to the propagation constants found from the literature. As can be seen, there is significantly more damping observed here than what has previously been observed. It is not clear why this discrepancy is seen. However, in contrast to the waveguiding studies by Balzer *et al.* [73], in which a single nanofiber was used and the propagation distance was altered by simply translating the excitation spot along the nanofiber, here two different fibers were used since the excitation position cannot be changed with electrical stimulation. Since the two nanofibers used in this analysis might have different morphology at the outcoupling points (breaks), this would influence the light scattering and thus the collected intensity at the nanofibers' break (the two intensity values are connected by a dashed line in Figure 5.12(b)). This would influence the result which could cause a different apparent damping. However, it is unknown if this can fully explain the observation, or if the transfer process is somehow altering the nanofibers and inducing a higher damping.

5.6 Summary

In this chapter, it was demonstrated that p6P nanofibers integrated on a FET device platform can emit polarized, highly localized, blue light under AC gate voltage stimulation. All the 13 samples used in EL studies worked successfully. The electroluminescence is caused by the radiative recombination of holes and electrons that are subsequently injected from the same electrode. In addition, it was shown how the nanofibers can act as optical waveguides of the generated EL that can thereby be routed to a different position on the chip. It shows the ability to electrically stimulate light in a nanoscale organic emitter and thereby opens up a wealth of opportunities for developing customizable on-chip light sources since the molecular building blocks of the nanofiber can be tailored via well-established synthesis techniques.

Chapter 6

Reduced bleaching by bilayer polymer/oxide coating

In addition to the special properties of the p6P nanofibers (see chapter 2), this material exhibit a characteristic photoinduced reaction during illumination with UV light that causes a decrease in luminescence intensity (photobleaching). The bleaching must be avoided since this reaction destroys the nanofibers and makes the technological use of the nanofibers difficult. Since photobleaching is partly attributed to a photooxidation reaction [80, 127], a promising solution is to apply a special coating onto the organic material to encapsulate and protect it from the ambient surroundings. Various materials as, for example, SiO_x [80], Al_2O_3 [128], and the bilayers Al_2O_3/SiO_2 [129], P(TFE-PDD)/SiO_x, P(TFE-PDD)/Al_2O_3, and PMMA/Al_2O_3 [130, 131, 132] have been investigated as a protecting layer against oxidation for organic materials.

In this chapter, an alternative bilayer coating is proposed, in which the first layer should work as a protection layer to avoid modifications of the p6P luminescence spectrum and the second layer is used as oxygen blocker. Such a combination results in a significant reduction in bleaching without affecting significantly the emission spectrum from the nanofibers. Once an appropriate coating material was found, surface characterizations were made by atomic force microscopy (AFM) to investigate how the morphology of the coated nanofibers was affected by UV exposure and in addition uncoated and coated samples were investigated with Raman spectroscopy to verify the the integrity of the nanofibers after coating. In addition, a degradation can also be observed during electrical measurements as a decrease in conductance. In the last part of this chapter, a similar coating is tested for its ability to minimize the electrical degradation effects.

6.1 Coating preparation

After nanofiber growth, different coatings were applied to study their ability to reduce the nanofiber bleaching. These include: SiO_x, Al_2O_3, P(TFE-PDD), PMMA, SU-8, SiO_x/Al_2O_3, P(TFE-PDD)/SiO_x, PMMA/SiO_x, P(TFE-PDD)/Al_2O_3, and PMMA/ Al_2O_3. The SiO_x and Al_2O_3 films were applied by electron beam evaporation using an Edwards Auto500 thin film deposition system. A mixture of silicon and silicon dioxide (SiO_2) was used as the deposition material to create SiO_x films [80] and the evaporation conditions were a pressure of 1×10^{-5} mbar and a maximum evaporation rate of about 0.3 nm/s. Activated alumina (Al_2O_3) was used as the deposition material to produce the Al_2O_3 films (pressure of 1×10^{-5} mbar and maximum rate of about 0.1 nm/s). The deposition thicknesses were monitored by a quartz crystal microbalance and the film thicknesses were verified using a profilometer. The polymer films [P(TFE-PDD), PMMA, and SU-8] were applied by spin coating. The spin coating conditions to create a 100-150 thick layer of PMMA are described in chapter 4. P(TFE-PDD) (Dupont) films were made from perfluorocarbon solution (FC-77, 3M, USA) by spin coating and drying at room temperature resulting in a thickness of 300 nm as measured using a profilometer.

6.2 Photobleaching

To collect the spectra and the bleaching decays, the samples were irradiated with an Hg lamp (emission line of 365 nm selected by a band pass filter) using an epifluorescence microscope with a Nikon UV-2A filter cube to separate the excitation and luminescence light, and a Ocean Maya2000 spectrometer coupled to the microscope with a collecting glass fiber with 100 μm core diameter. In this setup, the UV light irradiated the nanofibers under normal incidence and the resulting luminescence was observed under normal incidence, too. The UV light was focused on the sample surface with a 100× objective giving a spot size of around 820 μm and an intensity at the sample surface of about 0.2 W/cm^2. As the UV-2A filter blocks wavelengths below 420 nm, some additional bleaching experiments were performed using a HeCd laser with a wavelength of 325 nm and without filters to observe the development of the full p6P spectrum, which extends below 420 nm. In this latter case, the spot size was around 1 mm and the intensity at the sample surface was approximately 0.1 W/cm^2.

6.2.1 Monolayer coatings

First, the coating materials were deposited onto a sample of pristine mica for recording the background. SU-8 was immediately discarded since it produces strong autofluorescence at the same region as the p6P nanofibers (see

Figure 6.1). SiO_x, Al_2O_3, PMMA, and P(TFE-PDD) monolayer and multilayer coatings showed transparent and colorless films without measurable autofluorescence.

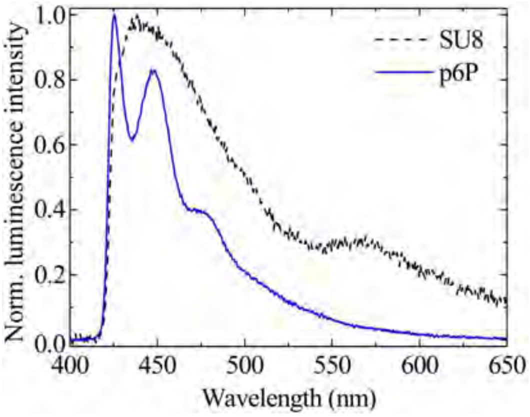

Figure 6.1: p6P nanofibers and SU-8 film spectra.

Figure 6.2 shows the normalized, initial spectra (at the beginning of UV illumination) for uncoated nanofibers and coated nanofibers with 200 nm SiO_x, 10 nm Al_2O_3, 300 nm P(TFE-PDD), and 100-150 nm PMMA, respectively.

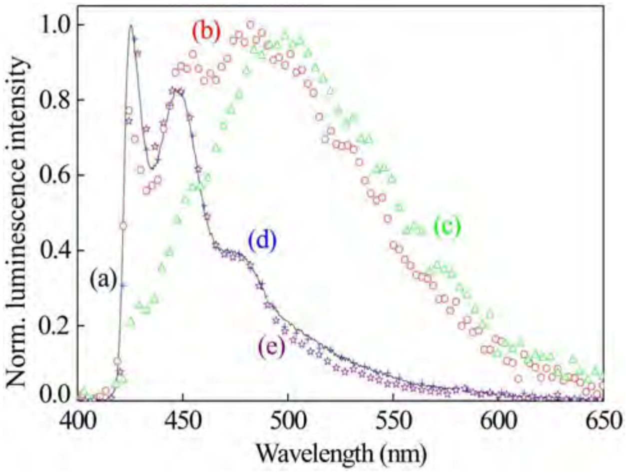

Figure 6.2: Normalized luminescence spectra of uncoated nanofibers (a), black line (-), and coated p6P nanofibers on mica. The coatings are 200 nm SiO_x (b), red circle (○), 10 nm Al_2O_3 (c), green triangle (△), 300 nm P(TFE-PDD) (d), blue cross (+), and 100-150 nm PMMA (e), purple star (⋆), respectively. Excitation at λ_{ex}=365 nm.

As seen from Figure 6.2, the two polymer coatings [P(TFE-PDD) and PMMA] do not change the p6P emission spectrum. The spectrum of the SiO_x coating, however, shows a broad emission peak in the green region around 500 nm. High SiO_x evaporation rates (>1 nm/s) generate an even broader emission from 425 to 625 nm and the luminescence of the nanofibers cannot be observed anymore. However, even using a fairly low SiO_x deposition rate, p6P nanofibers coated with 300 nm SiO_x show meanderlike breaks [80] in addition to the peak in the green. It is thus not suitable to use more than 200 nm SiO_x directly on p6P nanofibers and it must be concluded that the evaporation rate for SiO_x films must not be too high (rate ≤ 0.3 nm/s).

In previous studies, Al_2O_3 has been applied as a coating material for organic solar cells as it is not permeable to oxygen [128, 129]. Figure 6.2 shows that the Al_2O_3 coating also induces a broad peak around 500 nm and the characteristic peaks from the nanofibers are no longer distinguishable. The reason for the parasitic emission is not clear yet. However, it excludes both inorganic coatings in direct contact with the p6P nanofibers so far as for a usage as oxygen barrier, although it has been shown that an atomic layer deposition process at temperature as low as 33°C has the potential to coat thermally fragile substrate such as organic materials [133].

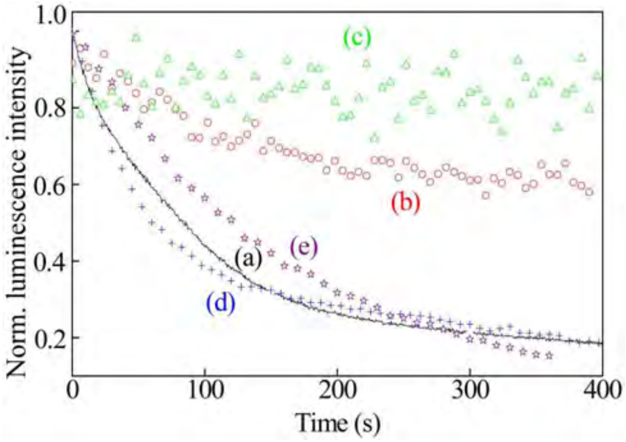

Figure 6.3: Normalized luminescence intensity for emitted light at λ_{em}=422 nm as a function of time from uncoated nanofibers (a), black line (-), and coated p6P nanofibers on mica. The coatings are 200 nm SiO_x (b), red circle (○), 10 nm Al_2O_3 (c), green triangle (△), 300 nm P(TFE-PDD) (d), blue cross (+), and 100-150 nm PMMA (e), purple star (⋆), respectively. Excitation at λ_{ex}=365 nm.

Figure 6.3 shows bleaching decay curves for the spectra displayed in Figure 6.2. For the 200 nm SiO_x coating, the luminescence intensity decays by about 40% after 7 min of UV illumination. For the 10 nm Al_2O_3 coating, the luminescence intensity does almost not change even after 13 min UV illumination. The spectra after UV illumination (not shown) reveal that the broad peak around 500 nm is significantly reduced for SiO_x coatings and the p6P spectrum is at least partially recovered [80] but for Al_2O_3 coatings, the p6P spectrum is not recovered. The bleaching of p6P nanofibers coated with P(TFE-PDD) and PMMA is similar to the bleaching for uncoated p6P nanofibers. This clearly indicates that the polymers alone cannot be used as coating materials since they are ineffective in reducing the bleaching.

6.2.2 Bilayer coatings

The bilayer SiO_x/Al_2O_3 was tested to investigate its use as an appropriate coating material for reducing the bleaching effects since a 200 nm SiO_x coating does not drown the characteristic fluorescence peaks from nanofibers completely (Figure 6.2) and since a 10 nm Al_2O_3 coating seems to stop bleaching (Figure 6.3). However, the bilayer 100 nm SiO_x/40 nm Al_2O_3 shows a huge peak at about 500 nm and the peaks of the p6P nanofibers are significantly reduced as seen in Fig. 6.4.

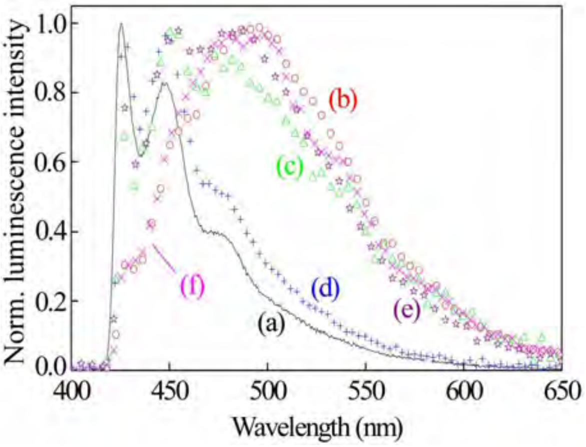

Figure 6.4: Normalized luminescence spectra of uncoated nanofibers (a), black line (-), and coated p6P nanofibers on mica. The coatings are 100 nm SiO_x/40 nm Al_2O_3 (b), red circle (○), P(TFE-PDD)/200 nm SiO_x (c), green triangle (△), P(TFE-PDD)/40 nm Al_2O_3 (d), blue cross (+), PMMA/200 nm SiO_x (e), purple star (⋆), and PMMA/40 nm Al_2O_3 (f) pink x (×), respectively. Excitation at λ_{ex}=365 nm.

The fact that polymer coatings do not interfere with the luminescence spectrum from the p6P (Figure 6.2) and oxide coatings appear to reduce bleaching reactions (Figure 6.3) indicates that bilayer coatings, with an initial polymer material as a protection layer to avoid the green fluorescence and an oxide layer as oxygen blocker would be favorable. Different polymer/oxide bilayer combinations were tested with the resulting spectra shown in Figure 6.4.

The P(TFE-PDD)/40 nm Al_2O_3 and P(TFE-PDD)/200 nm SiO_x spectra are not so distorted if compared to the p6P spectrum (Figure 6.4) but the coatings show a fast bleaching reaction (see Figure 6.5). Another disadvantage of using P(TFEPDD) is that the surface of the P(TFE-PDD)/200 nm SiO_x coated sample shows the appearance of meanderlike breaks on the surface in addition to the region exposed to UV light appearing partly burned as can be observed in Figure 6.6.

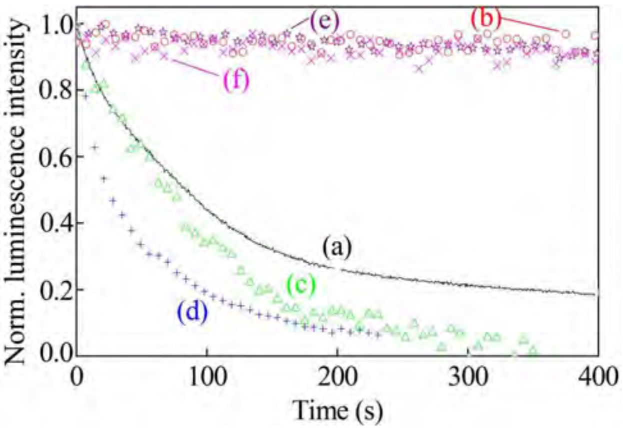

Figure 6.5: Normalized luminescence intensity for emitted light at λ_{em}=422 nm from uncoated nanofibers (a) black line (-), and coated p6P nanofibers on mica. The coatings are 100 nm SiO_x/40 nm Al_2O_3 (b), red circle (○), P(TFE-PDD)/200 nm SiO_x (c), green triangle (△), P(TFE-PDD)/40 nm Al_2O_3 (d), blue cross (+), PMMA/200 nm SiO_x (e), purple star (⋆), and PMMA/40 nm Al_2O_3 (f) pink x (×), respectively. Excitation at λ_{ex}=365 nm.

In terms of reducing the bleaching, the combinations of 100 nm SiO_x/40 nm Al_2O_3, PMMA/200 nm SiO_x, and PMMA/40 nm Al_2O_3 are most promising, as the bleaching is significantly suppressed as seen in Figure 6.5. From Figure 6.4, however, it is clear that the bilayer PMMA/200 nm SiO_x, although inducing a broad peak around 500 nm, has the least degrading effect on the spectrum. In addition, it is interesting to investigate the spectra after bleaching. Figure 6.7 shows that after extended UV exposure, the peak around 500 nm is now less pronounced and the "pure" p6P spectrum is partly recovered for the PMMA/SiO_x coating, while the other two bilayer coating samples still exhibit a substantial green emission peak.

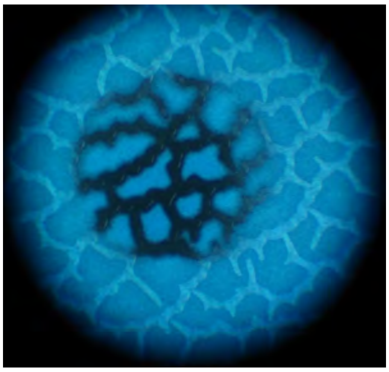

Figure 6.6: Fluorescence microscope image of the sample coated with P(TFE-PDD)/200 nm SiO_x. The nanofiber film exhibits meanderlike breaks and after 7 min the spot exposed to UV light appears burned.

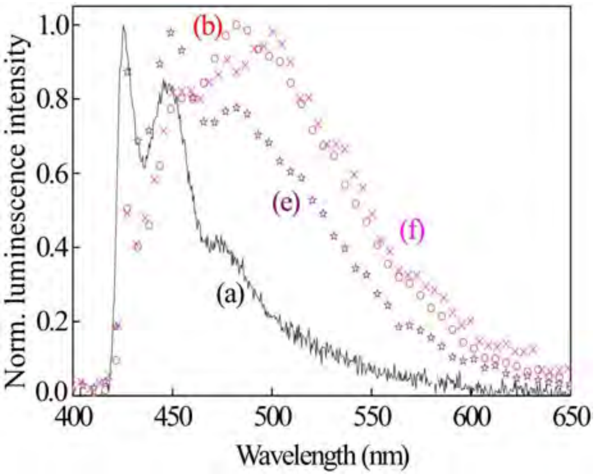

Figure 6.7: Normalized luminescence spectra of uncoated nanofibers (a), black line (-), after 410 s of UV illumination and coated p6P nanofibers on mica. The coatings are 100 nm SiO_x/40 nm Al_2O_3 (b), red circle (○), after 1865 s of UV illumination, PMMA/200 nm SiO_x (e), purple star (⋆), after 880 s of UV illumination and PMMA/40 nm Al_2O_3 (f) pink x (×), after 1995 s of UV illumination, respectively. Excitation at λ_{ex}=365 nm.

6.2.3 PMMA/SiO_x coating optimization

Of the tested coating candidates, the combination of PMMA/SiO_x appears to be an appropriate coating for p6P nanofibers, so additional samples were prepared to search for the best SiO_x thickness and to verify the effectiveness of this coating. From Figure 6.8, it can be observed that the thicker SiO_x

coating in the PMMA/SiO$_x$ bilayer has the more intense peak at around 500 nm, while it was observed that they give rise to almost the same slow bleaching decay (in Figure 6.5, the bleaching decay for PMMA/200 nm SiO$_x$ is shown) even after 30 min of UV illumination (the luminescence intensity decays by about 25% for 50, 100, and 300 nm SiO$_x$ and only by 14% for 200 nm SiO$_x$ for the samples shown in Figure 6.8). After irradiation the spectra in Figure 6.8 are similar to the spectrum for uncoated nanofibers as observed in Figure 6.7. Therefore, to better identify the behavior of the PMMA/200 nm SiO$_x$, the full spectrum was recorded using a 325 nm wavelength laser system to excite the photoluminescence to study the time evolution of the full spectrum (Figure 6.9).

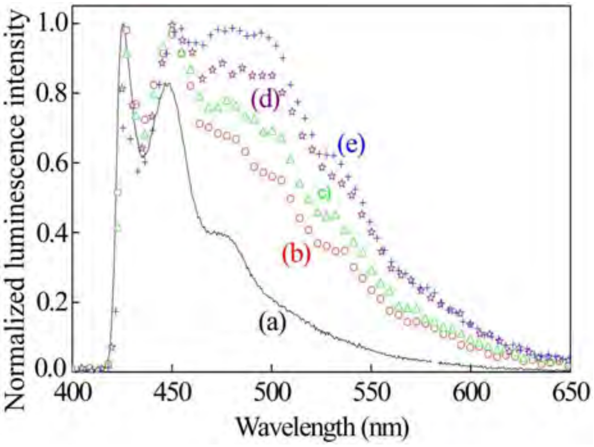

Figure 6.8: Normalized luminescence spectra of uncoated nanofibers (a), black line (-), and coated p6P nanofibers on mica. The coatings are PMMA/50 nm SiO$_x$ (b), red circle (○), PMMA/100 nm SiO$_x$ (c), green triangle (△), PMMA/200 nm SiO$_x$ (d), purple star (⋆), PMMA/300 nm SiO$_x$ (e), blue cross (×), respectively. Excitation at λ_{ex}=365 nm.

The similar appearance of the spectra excited by 325 nm and 365 nm wavelengths, respectively, indicates that the additional photon energy in the 325 nm photons is not causing any significant difference. From Figure 6.9, it can be observed that the peak at around 500 nm decreases while the peaks at ∼401 and ∼422 nm do not suffer from significant variations in wavelength and intensity. The changes of the peak at ∼448 nm are due to the changes on the large peak around 500 nm, which has a broad tail into the 448 nm peak. The peak around 500 nm appears to be the only peak that decreases significantly after UV illumination for the PMMA/SiO$_x$ coating. After 40 min of UV illumination, the full spectrum of the p6P nanofibers coated with PMMA/200 nm SiO$_x$ looks similar to the full spectrum for uncoated p6P nanofibers (Figure 6.9).

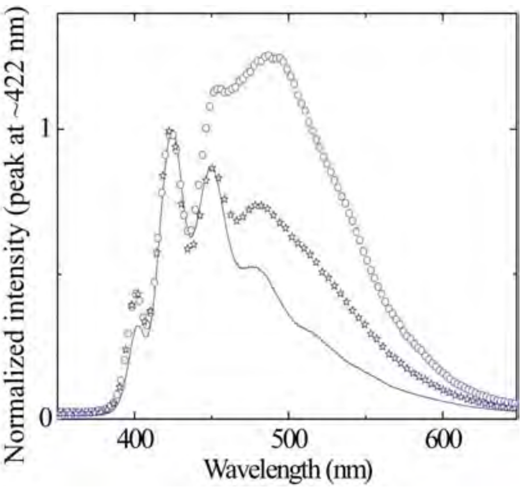

Figure 6.9: Normalized luminescence spectra of uncoated nanofibers, black line (-), and p6P nanofibers on mica coated with PMMA/200 nm SiO_x at the beginning of illumination, purple circle (○), and after 40 min of UV illumination, blue star ($\star$). Excitation at λ_{ex}=325 nm, spectra are normalized using the emission wavelength λ_{em}=422 nm.

In Figure 6.10(a), the residual difference between the spectra from coated p6P nanofibers (PMMA/200 nm SiO_x) and the spectrum from uncoated p6P is presented and in Figure 6.10(b) the evolution of the prominent peak at 500 nm derived from the residual difference in Figure 6.10(a). It appears that the spectrum from the coated samples tends to stabilize with time.

D. Vollath et al. [130, 131] have shown a large emission peak for alumina nanoparticles coated with PMMA around 450 nm and the authors have suggested that the combination of nonfluorescent oxide material with nonfluorescent polymer coating may lead to a nanocomposite with strong fluorescence. In order to investigate if the additional peaks observed in our measurements were due to a similar effect, a pure mica substrate was coated with the PMMA/200 nm SiO_x bilayer, however no fluorescence could be observed.

Kadashchuk et al. [134] have observed a similar peak in p6P spectra and found that it was caused by structural defects within the p6P material. The following explanation is proposed to account for the observations: upon deposition of either SiO_x or Al_2O_3 (which are both deposited by electron beam evaporation), structural defects are generated in the nanofibers either by the impinging metal atoms/clusters or by the thermal stress, thereby causing the significant defect peak around 500 nm. A similar spectral change is not observed with the single-layer PMMA and P(TFE-PDD) coatings, as the spin-coating process is gentler. The PMMA/SiO_x bilayer coating

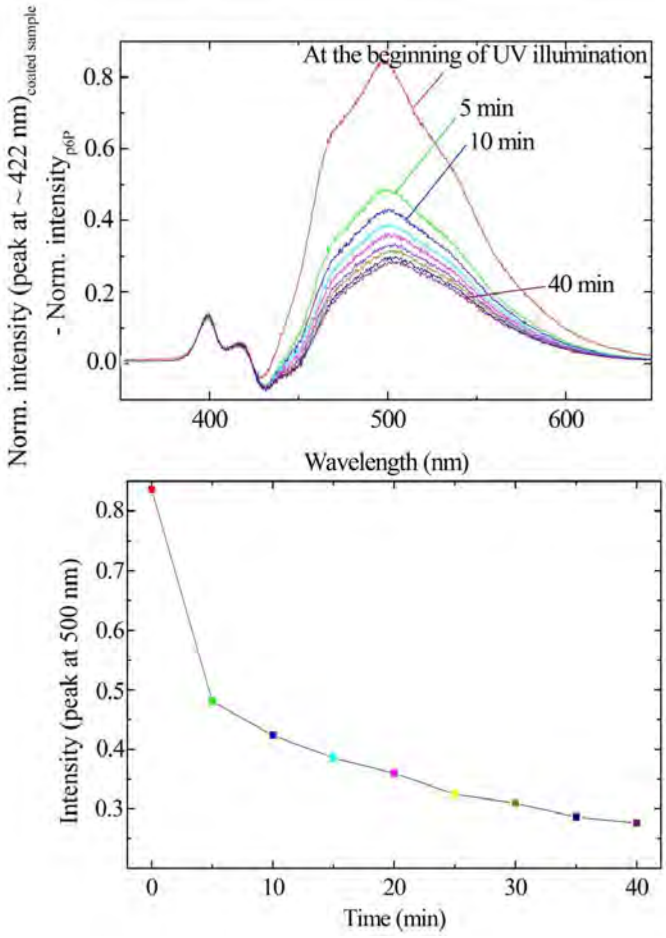

Figure 6.10: (a) Residual difference between spectra of coated p6P nanofibers with PMMA/200 nm SiO_x and uncoated p6P nanofibers recorded at 5 min intervals and (b) evolution of the prominent peak at 500 nm observed from the residual difference between spectra of coated p6P nanofibers with PMMA/200 nm SiO_x and uncoated p6P nanofibers during UV illumination using a 325 nm laser.

appears to be the best compromise of minimum bleaching and the least pronounced defect peak, which is even reduced with UV illumination. The reason for the reduction is at present not clear, but we speculate that the UV illumination could somehow "anneal" some of the defects.

6.2.4 PMMA/SiO$_x$ coating characterization

Raman Spectroscopy

Raman spectroscopy measurements were made for structural investigations of the p6P molecules [71, 72] before and after coating. This was done using a laser with a wavelength of 532 nm and a power of ≈130-200 mW coupled to a microscope with a 10× objective. Raman spectroscopy measurements show the characteristic peaks from p6P nanofibers [71, 72] even after coating with PMMA/200 nm SiO$_x$ which suggests that at least the local atomic arrangement of the nanofibers has not been affected by this bilayer coating (Figure 6.11).

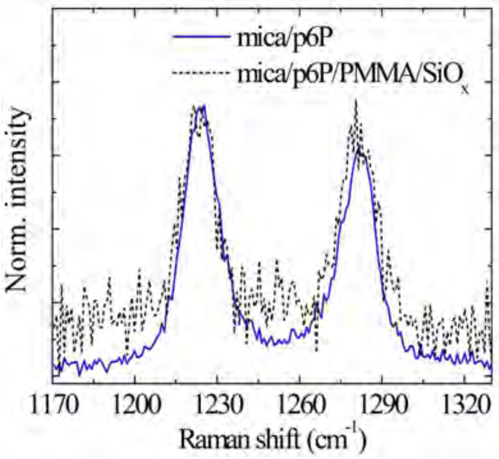

Figure 6.11: Raman spectroscopy of uncoated thick layer of p6P and of coated p6P nanofibers with PMMA/200 nm SiO$_x$.

Atomic Force Microscopy (AFM)

Tapping-mode AFM was used to study morphology of the coated nanofibers before and after UV illumination. Figures 6.12(a) and (b) show AFM images of a PMMA/SiO$_x$ coated sample before and after 1 h of UV illumination, respectively, and Figure 6.12(c) shows the linescans for the lines indicated in Figures 6.12(a) and (b). The surface roughness average for the coated but unbleached region on the PMMA/SiO$_x$ sample (Figure 6.12(a)) is 113 nm. For the coated and bleached (during 1 h) region (Figure 6.12(b)), the surface roughness average is 110 nm. Obviously, the bleaching has very little effect on the surface morphology of the coated samples, since the surface roughness is essentially the same. Hence, the coating is not affected by the UV illumination and the nanofibers are preserved and no material is removed from the nanofibers.

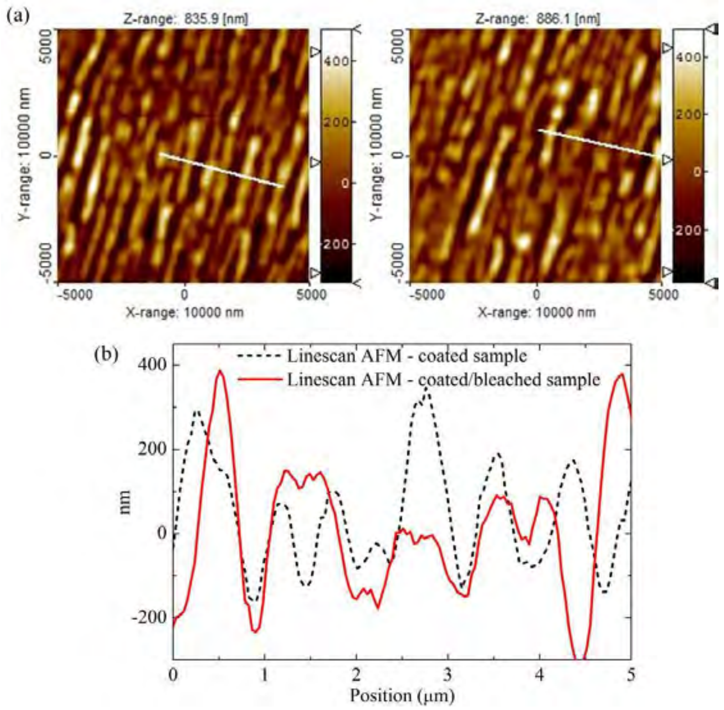

Figure 6.12: (a) AFM image from mica/p6P/PMMA/200 nm SiO_x sample and (b) AFM image from mica/p6P/PMMA/200 nm SiO_x sample after 1 h UV illumination. (c) Linescans for the images in Figures 6.12(a) and 6.12(b).

6.3 Reduction of electrical degradation

This section describes preliminary experiments carried out in order to investigate if the bilayer coating, which was developed to avoid degradation of the optical nanofiber properties, also can function to preserve the electrical nanofiber properties. The degradation in this case would be observed as a *decrease in conductance*, which could potentially then be minimized by the bilayer coating. Only preliminary tests were done, but these showed some promising results and are therefore presented here. One of the experiments was performed with coated p6P nanofibers on a FET device platform and the other with an uncoated p6P thin film also on a FET device platform.

Figure 6.13(a) shows the current density vs. drain-source voltage for zero gate voltage for nanofibers integrated via the roll printing technique (Chapter 3) onto a FET device in BC/BG configuration and coated with the 100-150 PMMA/200 SiO_x layer. The FET platform had the same design with interdigitated electrodes as described in chapter 5, however the SiO_2 dielectric was only 200 nm thick (as in chapter 4) and the distance between the electrodes was 25 μm. The inset in Figure 6.13(a) shows a fluorescence microscope image of the nanofibers on the FET platform before coating and electrical characterization. In the measurements in Figure 6.13(a), the drain-source voltage was swept from 0 V to 40 V, then kept constant at 40 V for 200 s before sweeping back to 0 V. During the constant voltage, the current was measured as a function of time to study if some type of degradation occurs (region indicated in Figure 6.13(a)). The time evolution of the current can be observed in Figure 6.13(b) and from the exponential curve fitting, a time decay of around 2827 s was extracted. Comparing the electrical characteristics shown in Figure 4.7(b), two things are very distinct: 1) the turn-on voltage is much lower in Figure 6.13(a) and 2) the hysteresis is considerably smaller in Figure 6.13(a).

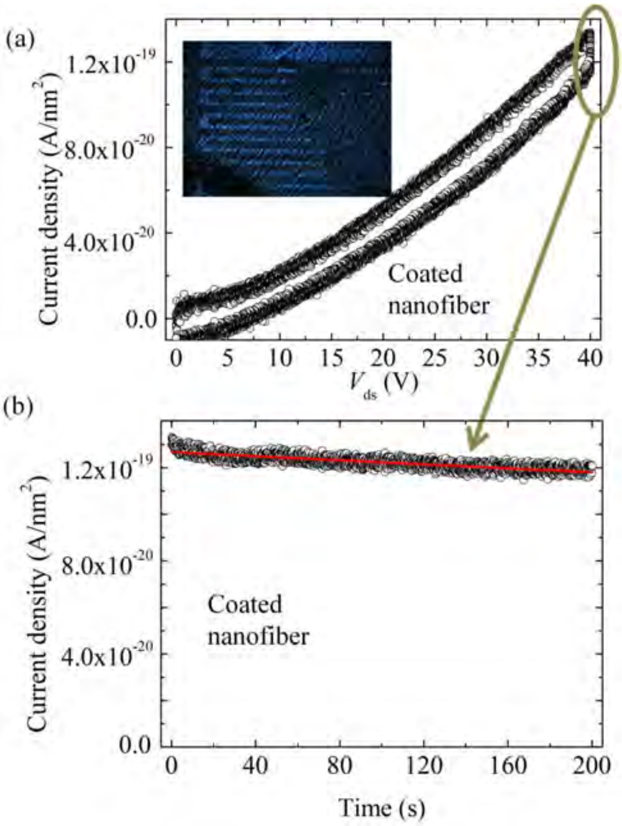

Figure 6.13: (a) Current density vs. drain-source voltage for zero gate voltage for transferred nanofibers to a FET device and coated with PMMA/SiO$_x$. Inset shows a fluorescence microscope image of the transferred nanofibers before coating. (b) Current density vs. time. Red line is the fitted exponential curve.

The lower turn-on voltage might not be related to the coating. A difference between the samples used in chapter 4 and the samples used here is the number of fibers, where there are around 10^2 times more fibers here. The higher number of fibers increases the probability of a larger number of well connected nanofibers. Another important issue is the size of the distance between the electrodes, where it is 12.5 times larger in the device used here. This gives a relatively larger contribution from the bulk resistance compared to the contact resistance and the influence of the injection barrier is consequently smaller.

The observed hysteresis in chapter 4 was interpreted as being due to trapping of charges. The results shown in Figure 6.13(a) would then indicate that charge trapping is somehow influenced by the ambient conditions around the sample. It should, however, be stressed that only one sample was investigated and no firm conclusions can therefore be drawn from these results.

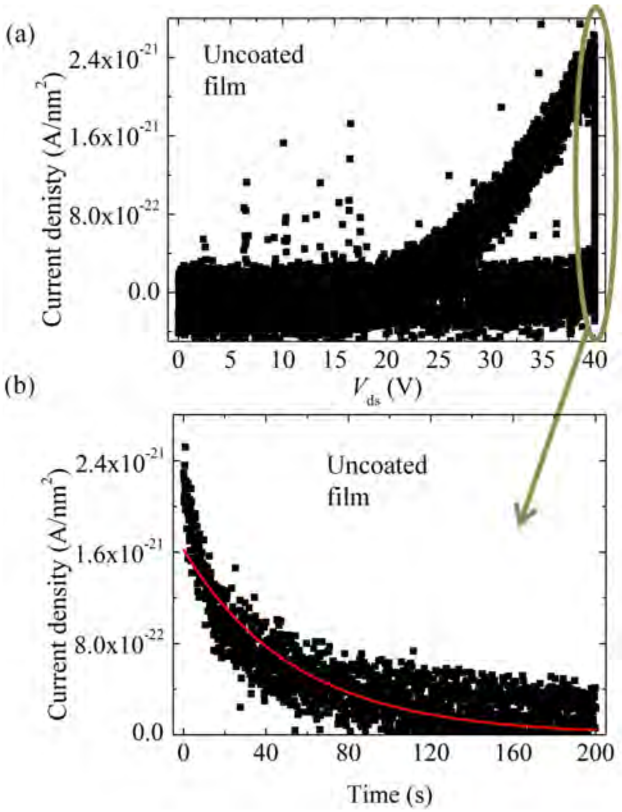

Figure 6.14: (a) Current density vs. drain-source voltage for zero gate voltage for p6P thin. (b) Current density vs. time. Red line is the fitted exponential curve.

To check the behavior of the time evolution of the current in uncoated p6P, a p6P thin film sample was tested using the same operational conditions used for the coated fibers (see Figure 6.14(a)). In Figures 6.13 and 6.14, the transfer characteristics are presented as current density instead of current intensity for the sake of direct comparison between film and fibers. Figure 6.14(b) shows stronger degradation, i.e. fast reduction of the current density for the uncoated film (time decay of around 54 s). Even with higher current being conducted (around two orders of magnitude) in the coated nanofibers the current conduction is much more stable compared to the uncoated p6P film device. Thus, the coating seems to be working as a protective layer for the coated fibers in Figure 6.13, however, more samples should be tried out. In addition, experiments in vacuum could be carried out, since vacuum should reduce any degradation caused by the surroundings as it should be done by the coating as well. The coating could also be used as a protective layer for EL experiments, which in chapter 5 have only been performed in vacuum conditions and very low degradation was observed (see Figure 5.7).

6.4 Summary

In a previous publication [80], it was shown that the bleaching can be attenuated but not completely stabilized in vacuum surroundings and that a coating of a few hundred nanometers thick layer of SiO_x does not completely stop the bleaching but significantly alters the spectrum from the nanofibers.

SiO_x coatings on p6P nanofibers result in a huge luminescence peak at 500 nm but after about 7 min of UV irradiation the spectra exhibit a reduction in this peak and the spectral features look more similar to the uncoated p6P nanofibers. However, the luminescence intensity still decays at a relatively high rate. Al_2O_3 coatings also generate a huge peak around 500 nm and even after long UV illumination, the spectra do not change and it has not been possible to identify the characteristic peaks from p6P nanofibers.

Bilayer polymer/oxide coatings show different behaviors. PMMA/200 nm SiO_x appears to be the best coating. Only weak bleaching has been observed even after about 30 min of UV illumination, the uncoated p6P spectrum has been to a large degree recovered after UV exposure, and Raman measurements suggest that no significant changes in molecular structure occurs. AFM images show that the surface morphology of this coating is almost not altered after extended UV illumination. In addition, the appearance of the coated sample with PMMA/200 nm SiO_x is not altered much as seen for example in Figure 6.6, even after 30 min of UV illumination. As conclusion the bilayer PMMA/200 nm SiO_x is proposed as blocking against oxygen and reducing UV light-induced photoreactions for protecting p6P nanofibers.

Chapter 7

Summary and Outlook

The development of a roll printing technique has enabled fast and large scale integration of organic p6P nanofibers on various devices with controlled positioning of the nanofibers and without loss of their parallel alignment. For integration of a certain number of fibers, the possibility of using nanostencils during the growth process or the use of a prestructured receiver substrate are demonstrated. The roll printing maintains the integrity of the nanofibers and enables direct electrical connection to metal electrodes in FET devices. Presumably, the roll printing technique can be applied for transfer of other organic nanofiber types and even for integration of several different types of nanofibers on the same device substrate by a multiple printing strategy.

The roll printing transfer has allowed the development of two types of operational devices: OFETs and organic light-emitting devices. The p6P nanofibers were integrated in both top and bottom contacted FET devices. The nanofiber OFETs showed p-type behavior with better conductance compared to transistor based on unordered thin films of the same material because of their better crystallinity. The nanofiber OFET devices with top contacts were made via nanostenciling, which does not damage the nanofibers during device fabrication as conventional lithography techniques would do. The conductance of top contact devices is higher and the turn-on voltage is lower compared to bottom contact devices due to a better electrical contact between the metal electrode and the organic material. This results in the output characteristics for top contact devices being dominated by the nanofiber bulk as opposed to the bottom contact devices, which exhibit injection-limited behavior.

In the future, further investigations of the transport properties of the organic nanofibers could be done by a four-point probe method [135] to elucidate their intrinsic properties. Improvements of the transistor characteristics could be accomplished by optimization of the gate dielectric thickness and by the use of larger source-drain gap distances to reduce short-channel effects and thereby induce saturation in the output characteristics. The use of a hydroxyl-free gate dielectric with a reduced number of charge trapping centers and/or the use of different electrode materials could potentially render ambipolar nanofiber OFETs. In addition, the p6P was used as a model system in these studies, however, other organic materials can be used. Other phenylene-based molecules such as methoxycyano-p-quaterphenylene (MOCNP4) [30] can form similar crystalline nanofiber structures with different transport properties.

Light-emitting devices made from organic nanofibers have been realized by application of an AC voltage to the nanofiber transistor gate electrode and symmetrical DC biasing of source and drain electrodes. This generated blue, localized, and polarized light emission from 100% of the fabricated devices (total number of 13). In addition, waveguiding was observed with light being guided along individual nanofibers and scattered from nanofiber breaks. The electroluminescence and the electrical characteristics as well, are strongly affected by the contact between the nanofiber and metal electrode, showing better performance after annealing presumably due to elimination of water at the nanofiber/electrode interface. Several optimizations could be performed on the present device geometry such as the use of polar self-assembled monolayers on the electrodes [136] to improve the carrier injection and thereby light emission.

The p6P nanofibers exhibit a characteristic photoinduced reaction (bleaching) resulting in a decrease in luminescence intensity upon UV light exposure in ambient conditions, which could render the technological use of the nanofibers problematic. In order to protect the nanofibers against bleaching, a bilayer polymer/oxide coating has been developed. This consists of first a polymer material (PMMA), which functions as a protection layer to avoid modifications of the p6P luminescence spectrum, and second an oxide layer (SiO_x) used as oxygen blocker. The coating showed a significant reduction in bleaching without affecting significantly the emission spectrum from the nanofibers.

The development of the nanofiber light-emitting devices has demonstrated nanoscale light sources with numerous potential device applications as for example lab-on-chip detectors. A further interesting step could be the realization of multicolor devices by multilayer transfer of different nanofibers. The development of the transfer printing technique as well the nanofiber OFET, the light-emitting devices, and of the protective coating layer were demonstrated using p6P nanofibers but can easily be applied for other organic materials. This therefore represents an important step in demonstrating the application potential of organic nanomaterials.

Appendix A

List of Publications

- L. Tavares, J. Kjelstrup-Hansen, H.-G. Rubahn, and H. Sturm. *Reduced bleaching in organic nanofibers by bilayer polymer/oxide coating.* Journal of Applied Physics, 2010, 107, pp. 103521 (1-6).
- L. Tavares, J. Kjelstrup-Hansen, K. Thilsing-Hansen, and H.-G. Rubahn. *Organic nanofibers integrated by transfer technique in field-effect transistor devices.* Nanoscale Research Letters, 2011, 6, pp. 319 (1-8).
- J. Kjelstrup-Hansen, L. Tavares, R. M. de Oliveira Hansen, X. Liu, K. Bordo, and H.-G. Rubahn. *Optical properties of microstructured surface-grown and transferred organic nanofibers.* Journal of Nanophotonics, 2011, 5, pp. 051701 (1-11).
- I. P. Radko, J. Fiutowski, L. Tavares, H.-G. Rubahn, and S.I. Bozhevolnyi. *Organic nanofiber-loaded surface plasmon-polariton waveguides.* Optics Express, 2011, 19, pp. 15155-15161.
- L. Tavares, J. Kjelstrup-Hansen, and H.-G. Rubahn. *Efficient Roll-on Transfer Technique for Well-Aligned Organic Nanofibers.* Small, *DOI: 10.1002/smll.201100660.*
- L. Tavares, J. Kjelstrup-Hansen, and H.-G. Rubahn. *Localized and guided electroluminescence from printed organic nanofibers.* ACS Nano, *Submitted.*
- R. M. de Oliveira Hansen, L. Tavares, J. Kjelstrup-Hansen, and H.-G. Rubahn. *Electrical Transport Properties of In Situ-Grown Organic Nanofibers on Transistor and 4-point Measurement Platforms.* Nanoscale, *Submitted.*

Appendix B

Process Recipe: Platforms

The transistor platforms used in chapters 3 and 4 were prepared using highly n-doped 4-inch silicon (100) wafers 525 μm thick with 200 nm thermally grown SiO_2. The fabrication steps are detailed below:

Positive photolithography - Platforms

1) Vapor deposition of hexamethyldisilzane (HDMS) for resist adhesion: 120°C, 30 min.

2) Spin on resist AZ5214A 1.5 μm thick:

2.1) 4 s dispense: 0 RPM, acc. 100 rps^2
2.2) 5 s dispense: 5000 RPM, acc. 5000 rps^2
2.3) 30 s dispense: 4000 RPM, acc. 10000 rps^2.

3) Bake on hot plate: 90°C, 60 s.

4) UV exposure of the resist: 4.2 s. This step is illustrated in Figure B.1, where the shape of the platforms are transferred to the resist. The platforms, as illustrated in Figure 4.3(a), have the dimensions of 1000 μm x 200 μm.

5) Development of the resist: Developer AZ351B (4 L of water/1 L developer), at 22°C for 60 s, agitation.

6) Rinse/dry: Rough rinse 1 min. Fine rinse 1 min. Spin dry 1 min 30 s.

7) HF: 4 min 48 s (Etch rate: $\approx$50 nm per min). HF etches the SiO_2 producing the 1000 μm x 200 μm x 0.2 μm SiO_2 platforms.

8) Rinse/dry: Rough rinse 5 min. Fine rinse 5 min. Spin dry 1 min 30 s.

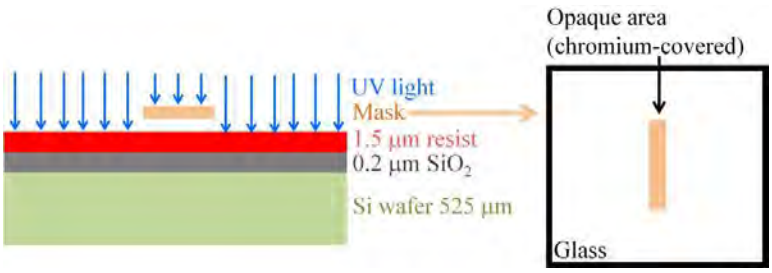

Figure B.1: Platfoms being produced by photolithography on SiO_2.

9) RIE plasma etching: 30 s. Etch rate: 2 μm/min. Etch parameters are given in table B.1. The RIE plasma etches the Si (1 μm) producing platforms with total height of 1.2 μm.

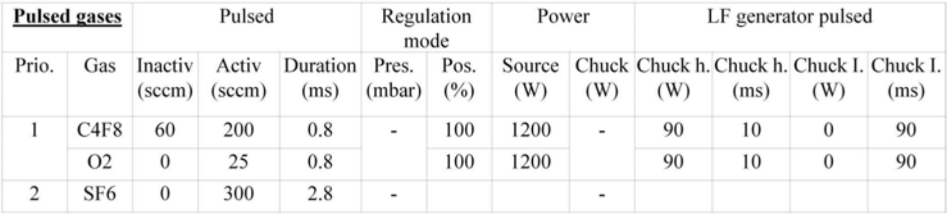

Pulsed gases		Pulsed			Regulation mode		Power		LF generator pulsed			
Prio.	Gas	Inactiv (sccm)	Activ (sccm)	Duration (ms)	Pres. (mbar)	Pos. (%)	Source (W)	Chuck (W)	Chuck h. (W)	Chuck h. (ms)	Chuck l. (W)	Chuck l. (ms)
1	C4F8	60	200	0.8	-	100	1200	-	90	10	0	90
	O2	0	25	0.8		100	1200		90	10	0	90
2	SF6	0	300	2.8	-			-				

Table B.1: RIE plasma conditions for etching in Si.

10) Removal of resist in acetone. Fine strip 15 min. Ultrasonic agitation.

11) Rinse/dry: Rough rinse 1 min. Fine rinse 1 min. Spin dry 1 min 30 s.

Negative photolithography - Bonding pads

12) HDMS: 120°C, 30 min.

13) Spin on resist AZ5214A 1.5 μm thick:

13.1) 4 s dispense: 0 RPM, acc. 100 rps^2
13.2) 5 s dispense: 5000 RPM, acc. 5000 rps^2
13.3) 30 s dispense: 4000 RPM, acc. 10000 rps^2.

14) Bake on hot plate: 90°C, 60 s.

15) Alignment of the bonding pads on top of the platforms. This step is illustrated in Figure B.2, where the bonding pads with dimensions of 390 μm x 180 μm (Figure 4.3) are transferred to the resist on top of the platform.

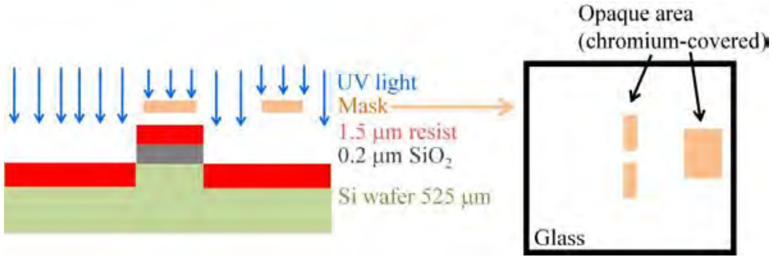

Figure B.2: Bonding pads being produced on top of the platforms. The gate is prepared on top of the doped silicon, which function as backgate electrode.

16) UV exposure of the resist: 2 s.

17) Reversal bake on hot plate: 130°C, 1 min 40 s.

18) Flood exposure: 25 s.

19) Development of the resist: Developer AZ351B (4 L of water/1 L developer), at 22°C for 60 s, agitation.

20) Rinse/dry: Rough rinse 1 min. Fine rinse 1 min. Spin dry 1 min 30 s.

21) Metal deposition by electron beam deposition (e-beam) of the bonding pads and gate electrode: 2 nm titanium/30 nm gold.

22) Lift-off:

22.1) Removal of metals in acetone. Fine strip 5 min with ultrasonic agitation with the wafer at the center of the bath container. Fine strip 5 min with ultrasonic agitation with the wafer at the extremity of the bath container.

22.2) Rinse/dry: Rough rinse 1 min. Fine rinse 1 min. Spin dry 1 min 30 s.

The top contact chips are ready in the step 22.2. The top contact electrodes are then made by nanostencil as described in appendix C.

For bottom contact chips, one additional process is done as following:

Positive photolithography - Electrodes

23) HDMS: 120°C, 30 min.

24) Spin on resist AZ5214A 1.5 μm thick:

    24.1) 4 s dispense: 0 RPM, acc. 100 rps^2
    24.2) 5 s dispense: 5000 RPM, acc. 5000 rps^2
    24.3) 30 s dispense: 4000 RPM, acc. 10000 rps^2.

25) Bake on hot plate: 90°C, 60 s.

26) Alignment of the electrodes that connect to the bonding pads on top of the platforms. This step is illustrated in Figure B.3. The electrodes have dimensions of 10 μm x 200 μm (Figure 4.3).

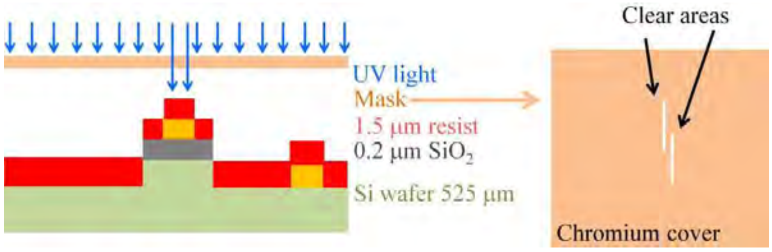

Figure B.3: Electrodes to connect the bonding pads being produced on top of the platforms.

27) UV exposure of the resist: 4.2 s.

28) Development of the resist: Developer AZ351B (4 L of water/1 L developer), at 22°C for 60 s, agitation.

29) Rinse/dry: Rough rinse 1 min. Fine rinse 1 min. Spin dry 1 min 30 s.

30) Metal deposition by e-beam of the electrodes: 2 nm titanium / 30 nm gold.

31) Lift-off:

31.1) Removal of metals in acetone. Fine strip 5 min at full ultrasonic with the wafer at the center of the bath container. Fine strip 5 min at full ultrasonic with the wafer at the extremity of the bath container.

31.2) Rinse/dry: Rough rinse 1 min. Fine rinse 1 min. Spin dry 1 min 30 s.

32) Spin on resist AZ5214A 1.5 μm thick. This step is to keep the chips clean after dicing.

32.1) 4 s dispense: 0 RPM, acc. 100 rps^2
32.2) 5 s dispense: 5000 RPM, acc. 5000 rps^2
32.3) 30 s dispense: 4000 RPM, acc. 10000 rps^2.

33) Bake on hot plate: 90°C, 60 s.

34) Dicing. Use dicing saw.

Appendix C

Process Recipe: Nanostencil

The nanostencils were prepared using a silicon wafer 525 μm thick with both polished and unpolished sides coated with 0.1 μm low-stress silicon nitride (SiN). The fabrication steps are detailed below:

Photolithography on the polished front-side

1) Vapor deposition of hexamethyldisilzane (HDMS) for resist adhesion: 120°C, 30 min.

2) Spin on resist AZ5214A 1.5 μm thick:

  2.1) 4 s dispense: 0 RPM, acc. 100 rps^2
  2.2) 5 s dispense: 5000 RPM, acc. 5000 rps^2
  2.3) 30 s dispense: 4000 RPM, acc. 10000 rps^2.

3) Bake on hot plate: 90°C, 60 s.

4) UV exposure of the resist: 4 s. This step is illustrated in Figure C.1, where the shape of the small holes to form the electrodes are transferred to the resist.

5) Development of the resist: Developer AZ351B (4 L of water/1 L developer), at 22°C for 60 s, agitation.

6) Rinse/dry: Rough rinse 1 min. Fine rinse 1 min. Spin dry 1 min 30 s.

7) RIE plasma etching: 1 min 30 s (1500 Ws, SH/S 200 mm, 80 W (10%), SF6: 300 sccm, 2.2 Pa, 20°C).

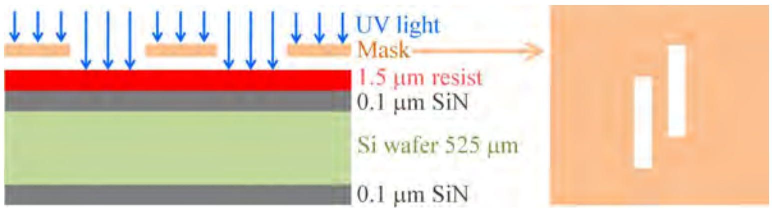

Figure C.1: Photolithography. Transfer of the electrodes pattern to the resist on the polished side of the wafer.

Photolithography on the unpolished backside

After patterning the shape of the electrodes on top of the SiN in the wafer front-side, the large holes that will form the membrane must be made on the backside of the wafer.

8) HDMS: 120°C, 30 min.

9) Spin on resist AZ5214A:

9.1) 4 s dispense: 0 RPM, acc. 100 rps^2
9.2) 5 s dispense: 5000 RPM, acc. 5000 rps^2
9.3) 30 s dispense: 3000 RPM, acc. 10000 rps^2.

10) Bake: 90°C, 60 s.

11) Alignment of the backside mask to the front-side pattern (backside alignment).

The dimensions of the open holes in the backside mask were determined to fit with the electrodes on the front-side as it is illustrated by the dashed line in Figure C.2.

Figure C.2: Dashed line are the dimensions of the suspended SiN membrane determine from the backside mask.

To determine the backside size of the mask pattern, the etching characteristics of silicon in KOH must be taken into account (see Figure C.3).

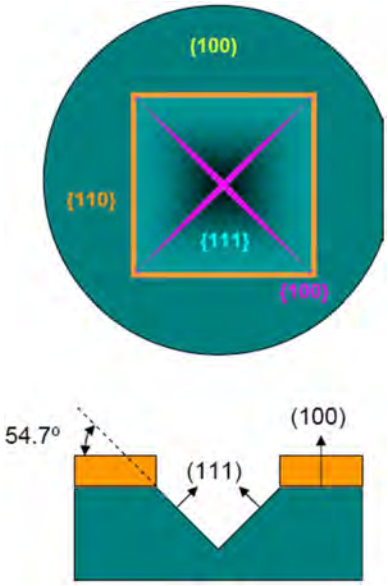

Figure C.3: Etching of silicon in KOH.

Where the etch ratio for the planes (100) and (111) in Figure C.3 are:

$R_{\{100\}}$=100 μm h^{-1}

$R_{\{111\}}$=1 μm h^{-1}

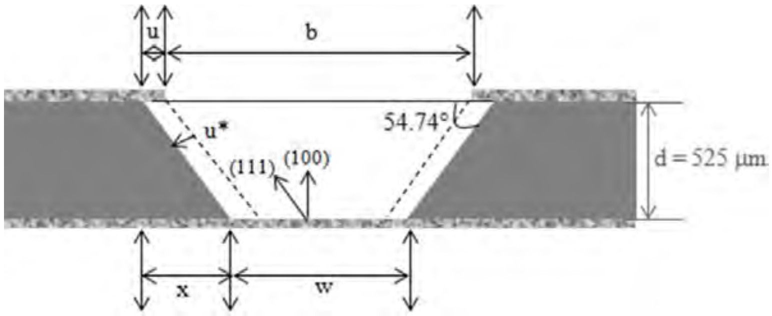

Figure C.4: Scheme to determine the final dimensions of the suspended SiN membrane determine from the backside mask.

Therefore, from Figure C.4 and for a circular silicon wafer with dimensions: 100 mm diameter and 525 μm:

$$x = \frac{d}{tan 54.74^\circ} \tag{C.1}$$

$x = \frac{525 \mu m}{1.14} \approx 371.17\ \mu$m

$$b = w + 2 \cdot x \tag{C.2}$$

So, for a required pattern of size w the mask should have a structure of size b as can be calculated from equation C.2.

For the stencils used to form the top contacts of the devices in chapter 4, the dimensions of the stencils are illustrated in Figure C.5.

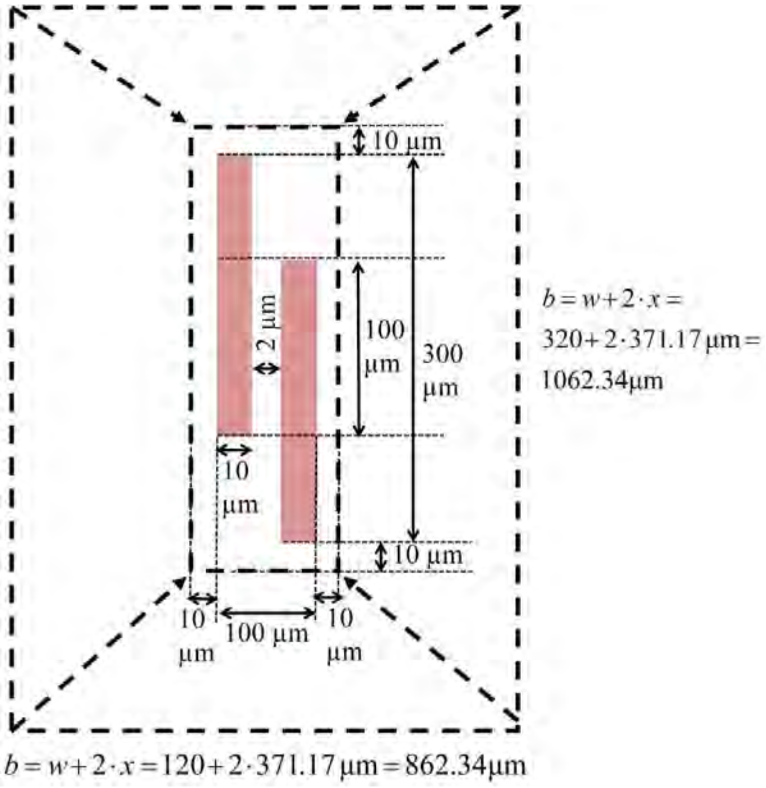

Figure C.5: Stencil dimensions.

12) UV exposure of the resist on the backside side of the wafer: 4.9 s. Here, the shape of the opening into the silicon to form the SiN membrane around the holes for the electrodes are transferred to the resist (see Figure C.6).

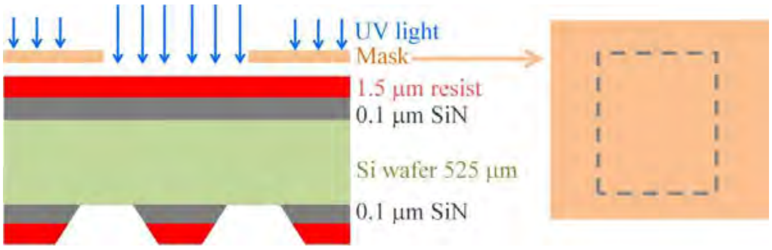

Figure C.6: Wafer upside down compared to Figure C.1 for backside patterning.

13) Development of the resist: Developer AZ351B (4 L of water/1 L developer), at 22°C for 60 s, agitation.

14) Rinse/dry: Rough rinse 1 min. Fine rinse 1 min. Spin dry 1 min 30 s.

15) RIE plasma etching: 3 min (1500 Ws, SH/S 200 mm, 80 W (10%), SF6:300 sccm, 2.2 Pa, 20°C).

16) Removal of resist in acetone. Fine strip 5 min.

17) Rinse/dry: Rough rinse 1 min. Fine rinse 1 min. Spin dry 1 min 30 s.

18) HF bath: 20 s. HF removes the native oxide layer on Si.

19) Rinse/dry: Rough rinse 5 min. Fine rinse 5 min. Spin dry 1 min 30 s.

20) KOH to etch Si the wafer. 28% wt, 80 °C, ≈ 9 h.

For 800 mL
Concentration 28% by weight
$\delta_{28\%}$=1.266 Kg/L
$M_{total}= \delta \cdot V_{total} = 1.266$ Kg/L $\cdot$ 0.8 L = 1.0128 Kg
$M_{KOH}= 0.28 \cdot M_{total} = 0.28 \cdot 1.0128$ Kg = 0.2836 Kg
$M_{H_2O}= 0.72 \cdot M_{total} = 0.72 \cdot 1.0128$ Kg = 0.7292 Kg
V_{H_2O}=0.73 L

Figure C.7 show a white microscope image of the backside of the wafer during KOH etching.

21) Rinse/dry: Rough rinse 5 min. Fine rinse 5 min. Dry gently.

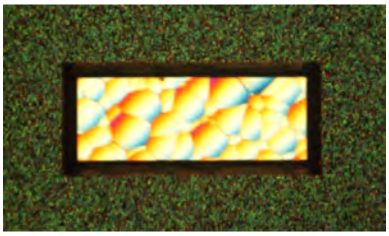

Figure C.7: White microscope image of the unpolished-backside of the wafer during KOH etching.

22) Fix a blue tape capable to cover the entire wafer on the backside. It will support the membranes during dicing and help to spin coat resist (see next step).

23) Spin on resist AZ5214A in order to support the SiN membrane during dicing.

23.1) 4 s dispense: 0 RPM, acc. 100 rps^2
23.2) 5 s dispense: 5000 RPM, acc. 5000 rps^2
23.3) 30 s dispense: 3000 RPM, acc. 10000 rps^2.

24) Bake: 90°C, 60 s.

25) Dicing 5 mm × 5mm chips. Use dicing saw.

The nanostencils are fixed on top of the chip (prepared as described until step 22.2 in appendix B) with the organic material. The alignment is made by hand under a white light microscope and the metal electrodes are prepared by e-beam deposition: 2 nm titanium / 30 nm gold.

Appendix D

Electroluminescence intensity

The absolute emitted EL intensity (I_{emit}) from the nanofibers in chapter 5 was estimated based on the transmittance (T) through the optical system (Figure D.1), the ratio (f) of collected to emitted light assuming a Lambertian emitter, the magnification (M) of the optical system, and the intensity (I_{CCD}) recorded at the EMCCD camera:

$$I_{emit} = \frac{I_{CCD} \times M^2}{T \times f} \tag{D.1}$$

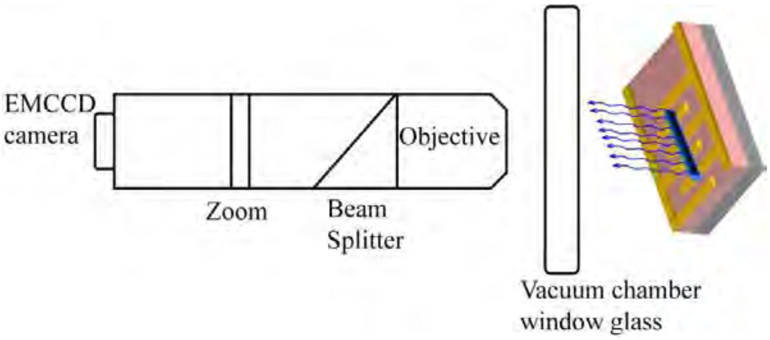

Figure D.1: Scheme of the optical system used to record EL from the FET devices.

1) Intensity (I_{CCD}) recorded at the EMCCD:

$$I_{CCD} = \frac{(Number\ of\ Photons/Pixel)_{max} \times Photon\ energy}{Acquisition\ time \times Pixel\ area} \tag{D.2}$$

$$(Number\ of\ Photons/Pixel)_{max} = \frac{Sensitivity \times Counts_{max}}{EM\ gain \times QE} \tag{D.3}$$

The scheme of the EMCCD camera structure is in Figure D.2 (adapted from [URL[1]]). From the indicated area in "Quantum Efficiency Curve" in Figure D.3 [URL[2]], it can be read that the quantum efficiency (QE) for the peak for p6P at 425 nm is around 45%.

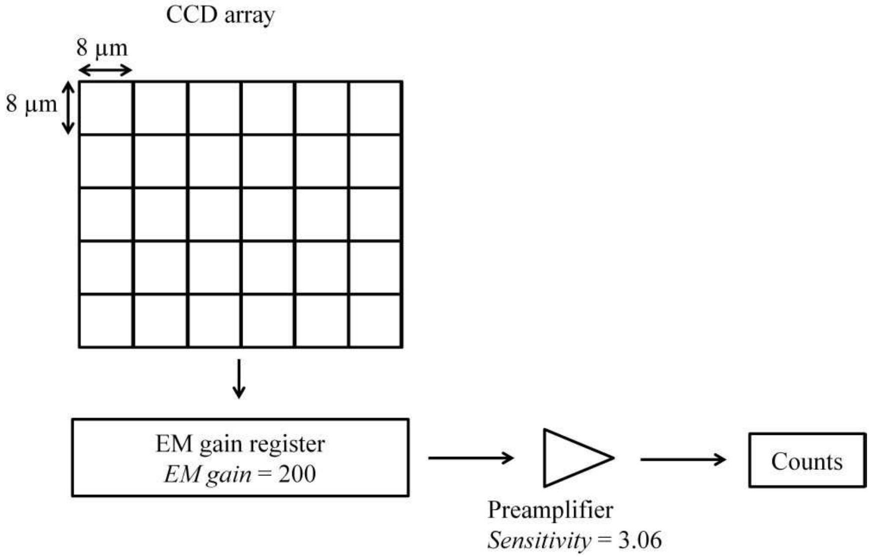

Figure D.2: Scheme of the EMCCD structure of the camera (adapted from URL[1]).

Sensitivity = 3.06 electrons/count.

The information about *Sensitivity* was taken from the technical Performance Sheet from Andor and Figure D.4 was obtained from a private conversation with Andor's product support.

$Counts_{max} = 15883$

Obtained from the full scale in the EL images in chapter 5 with specific settings.

EM gain = 200 (it is the maximum recommended setting for EM gain).

From equation D.3:

---

[1] `http://www.andor.com/pdfs/Digital%20Camera%20Fundamentals.pdf`

[2] `http://www.andor.com/scientific_cameras/luca/models/default.aspx?iProductCodeID=14`

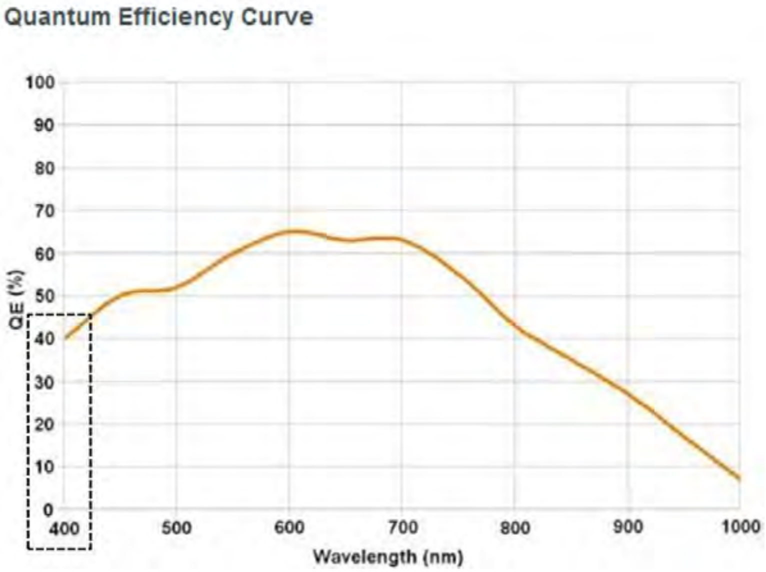

Figure D.3: Quantum Efficiency Curve (adapted from URL[2]).

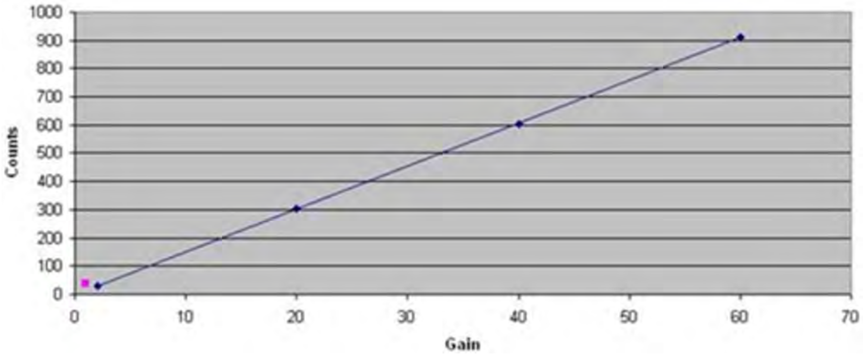

Figure D.4: Experimental determination of the gain for the EMCCD camera. From private conversation with Andor's product support.

$(Number\ of\ Photons/Pixel)_{max} = \frac{3.06 \times 15883}{200 \times 0.45} = 540.022$

To complete equation D.2:

$Photon\ energy = \frac{hc}{\lambda} = \frac{6.626 \times 10^{-34}[Js] \times 3 \times 10^{8}[m/s]}{4.25 \times 10^{-7}[m]} \approx 4.677 \times 10^{-19}$ J.
Where $\lambda = 425$ nm is the main peak wavelengths of the emitted light from p6P nanofibers.

$Acquisition\ time = 5$ s.

Pixel area = 64×10^{-12} m^2 (*Pixel area* can be found in URL[2]).

So, from equation D.2:

$I_{CCD} = \frac{540.022 \times 4.677 \times 10^{-19} [J]}{5[s] \times 64 \times 10^{-12} [m^2]} = 7.89 \times 10^{-7}$ W m^{-2}

2) Transmission T through the optical system:

The transmission was measured in a wavelength range of 400 - 450 nm (and private communication with Andor's product support) giving:

Transmission through the vacuum chamber glass window = 92 %.

Transmission through the 10 × objective = 80 %.

Transmission through the Beam Splitter = 40 %.

Transmission through the zoom lens (Zoom 6000 [URL[3]]) = 75 %.

$$T = 0.92 \times 0.8 \times 0.4 \times 0.75 = 0.22 \tag{D.4}$$

3) Ratio f of collected to emitted light assuming a Lambertian emitter:

$$f = \frac{f_{objective}}{f_{total}} = \frac{\int_0^{\theta} sin(2\theta) d\theta}{\int_0^{\theta=90^\circ} sin(2\theta) d\theta} \tag{D.5}$$

The numerical aperture (NA) of an objective lens is defined by $NA = nsin\theta$, in which $n = 1$ is the index of refraction for air, the NA for the 10 × objective is 0.25, so $\theta = \sin^{-1} 0.25 \approx 14.4775^\circ$.

$f_{objective} = \int_0^{\theta=14.4775^\circ} sin(2\theta) d\theta = [-\frac{1}{2}\cos 2\theta]_0^{14.4775^\circ} = 0.0625$

$f_{total} = \int_0^{\theta=90^\circ} sin(2\theta) d\theta = [-\frac{1}{2}\cos 2\theta]_0^{90^\circ} = 1$

So, from equation D.5:

$f = \frac{f_{objective}}{f_{total}} = 0.0625$

4) Magnification M of the images:

The ratio of the transverse dimensions of the final image formed by any optical system to the corresponding dimension of the object is defined as

---

[3] `http://machinevision.navitar.com/pdfs/6x_brochure.pdf`

magnification [137].

Image area of the EMCCD camera: 64 mm^2 (see Figure D.2).

The size of Figure 5.4(a): 0.64 mm^2, so $M = 100$.

The size of Figures 5.10 and 5.11(a)-(d): 0.14 mm^2, so $M \approx 457$.

So, from equation D.1 the I_{emit} is:

for Figure 5.4(a): $I_{emit} = \frac{I_{CCD} \times M^2}{T \times f} = \frac{7.89 \times 10^{-7} [W/m^2] \times 100}{0.22 \times 0.0625} \approx 6 \times 10^{-3}$ W m^{-2}

and for Figures 5.10 and 5.11(a) and (d): $I_{emit} = \frac{I_{CCD} \times M^2}{T \times f} = \frac{7.89 \times 10^{-7} [W/m^2] \times 457}{0.22 \times 0.0625}$ $\approx 2 \times 10^{-2}$ W m^{-2}.

Appendix E

Waveguiding

According to Balzer *et al.* [73], the crystal structure observed in the p6P nanofibers (Figure 2.3) cause anisotropic dielectric properties, i.e. the dielectric constant is a tensor with two different components, the parallel ($\epsilon_{||}$) and the perpendicular ($\epsilon_{\perp}$).

$$\epsilon_{||} = \epsilon_{||}^{'} - i\epsilon_{||}^{''} = 4.8 - i\epsilon_{||}^{''}[73] \tag{E.1}$$

Different values of $\epsilon_{||}^{''}$ have been reported; either by Balzer *et al.* [73, 138] ($\epsilon_{||}^{''}$ ≈0.0119) and by Volkov *et al.* [139] ($\epsilon_{||}^{''}$ ≈0.0042).

$$\epsilon_{\perp} = 1.9[73] \tag{E.2}$$

From ref.[73] the damping of the guided light in the nanofiber is presumably due reabsorption inside the nanofiber and can be determined by the propagation constant β, which is related to the dielectric components ($\epsilon_{||}$ and $\epsilon_{\perp}$):

$$\beta = \sqrt{\frac{\omega^2}{c^2}\epsilon_{||} - \frac{\epsilon_{||}}{\epsilon_{\perp}}\left(\frac{m\pi}{a}\right)^2} \tag{E.3}$$

Inserting E.2 and E.1 in E.3:

$$\beta = \sqrt{\frac{\omega^2}{c^2}\epsilon_{||}^{'} + \frac{\omega^2}{c^2}i\epsilon_{||}^{''} - \frac{\epsilon_{||}^{'}}{\epsilon_{\perp}}\left(\frac{\pi}{a}\right)^2 - i\frac{\epsilon_{||}^{''}}{\epsilon_{\perp}}\left(\frac{\pi}{a}\right)^2} \tag{E.4}$$

Rearranging E.4:

$$\beta = \sqrt{\left(\frac{\omega^2}{c^2} - \frac{1}{\epsilon_{\perp}}\left(\frac{\pi}{a}\right)^2\right)\epsilon_{||}^{'} + i\epsilon_{||}^{''}\left(\frac{\omega^2}{c^2}\frac{1}{\epsilon_{\perp}}\left(\frac{\pi}{c}\right)^2\right)} \tag{E.5}$$

$$\beta = \sqrt{\left(\epsilon_{||}^{'} + i\epsilon_{||}^{''}\right)\left(\frac{\omega^2}{c^2} - \frac{1}{\epsilon_{\perp}}\left(\frac{\pi}{a}\right)^2\right)} \tag{E.6}$$

$$\beta = \sqrt{\frac{\omega^2}{c^2} - \frac{1}{\epsilon_\perp}\left(\frac{\pi}{a}\right)^2}\sqrt{\epsilon_{||}^{'} + i\epsilon_{||}^{''}} \tag{E.7}$$

$$\beta = \sqrt{\frac{\omega^2}{c^2} - \frac{1}{\epsilon_\perp}\left(\frac{\pi}{a}\right)^2}\sqrt{\epsilon_{||}^{'}\left(1 + i\frac{\epsilon_{||}^{''}}{\epsilon_{||}^{'}}\right)} \tag{E.8}$$

$$\beta = \sqrt{\frac{\omega^2}{c^2} - \frac{1}{\epsilon_\perp}\left(\frac{\pi}{a}\right)^2}\sqrt{\epsilon_{||}^{'}}\sqrt{\left(1 + i\frac{\epsilon_{||}^{''}}{\epsilon_{||}^{'}}\right)} \tag{E.9}$$

Using square root Maclaurin series expansion:

$$\sqrt{1+x} = \sum_{n=0}^{\infty} \frac{(-1)^n (2n)!}{(1-2n)(n!)^2 (4^n)} x^n \cong 1 + \frac{1}{2}x \tag{E.10}$$

for the last term of the equation E.9 $\left(\sqrt{\left(1 + i\frac{\epsilon_{||}^{''}}{\epsilon_{||}^{'}}\right)}\right)$:

$$\beta = \sqrt{\frac{\omega^2}{c^2} - \frac{1}{\epsilon_\perp}\left(\frac{\pi}{a}\right)^2}\sqrt{\epsilon_{||}^{'}}\left(1 + i\frac{\epsilon_{||}^{''}}{2\epsilon_{||}^{'}}\right) \tag{E.11}$$

$$\beta = \sqrt{\frac{\omega^2}{c^2} - \frac{1}{\epsilon_\perp}\left(\frac{\pi}{a}\right)^2}\left(\sqrt{\epsilon_{||}^{'}} + i\frac{\epsilon_{||}^{''}}{2\sqrt{\epsilon_{||}^{'}}}\right) \tag{E.12}$$

Therefore the imaginary part of the propagation constant β is:

$$Im(\beta) = \sqrt{\frac{\omega^2}{c^2} - \frac{1}{\epsilon_\perp}\left(\frac{\pi}{a}\right)^2}\frac{\epsilon_{||}^{''}}{2\sqrt{\epsilon_{||}^{'}}} \tag{E.13}$$

$\omega = \frac{2c\pi}{\lambda}$

giving $\frac{\omega^2}{c^2} = \frac{4\pi^2}{\lambda^2}$, where λ=425 nm.

Using from literature $\epsilon_\perp$=1.9 [73] and a=740 nm for the fiber in Figure 5.11(a), from equation E.13 and for the dielectric constant $\epsilon_{||}^{''} \approx 0.0119$ [73, 138] and $\epsilon_{||}^{''} \approx 0.0042$ [139] it is possible for example to estimate the $Im(\beta)$ for the fiber in Figure 5.11(a): $Im(\beta)_{\epsilon_{||}^{''} \approx 0.0119} = 4.0 \times 10^4$ m^{-1} and $Im(\beta)_{\epsilon_{||}^{''} \approx 0.0042} = 1.4 \times 10^4$ m^{-1}.

Bibliography

[1] B. Bhushan, *Handbook of Nanotechnology* (Springer, 2004).

[2] W. Lu and C. M. Lieber, Nature Materials **6**, 841 (2007).

[3] S. Lal, S. Link, and N. J. Halas, Nature Photonics **1**, 641 (2007).

[4] M. Li, H. X. Tang, and M. L. Roukes, Nature Nanotechnology **2**, 114 (2007).

[5] J. Goldberger, R. Fan, and P. Yang, Accounts of Chemical Research **39**, 239 (2006).

[6] Y. Cui, Q. Wei, H. Park, and C. M. Lieber, Science **293**, 1289 (2001).

[7] K. Jain, Expert Review of Molecular Diagnostics **3**, 153 (2003).

[8] A. L. Pyayt, B. Wiley, Y. Xia, A. Chen, and L. Dalton, Nature Nanotechnology **3**, 660 (2008).

[9] J. D. Plummer, M. Deal, and P. D. Griffin, *Silicon VLSI Technology: Fundamentals, Practice, and Modeling* (Prentice Hall, 2000).

[10] J. W. Judy, Smart Materials and Structures **10**, 1115 (2001).

[11] M. A. Unger, H.-P. Chou, T. Thorsen, A. Scherer, and S. R. Quake, Science **288**, 113 (2000).

[12] O. N. Tufte, P. W. Chapman, and D. Long, Journal of Applied Physics **33**, 3322 (1962).

[13] W. Riethmüller, W. Benecke, U. Schnakenberg, and B. Wagner, Sensors and Actuators A: Physical **31**, 121 (1992), Proceedings of Eurosensors V.

[14] P. Kim *et al.*, Biochip Journal **2**, 1 (2008).

[15] M. T. Björk *et al.*, Nano Letters **2**, 87 (2002).

[16] M. S. Gudiksen, L. J. Lauhon, J. Wang, D. C. Smith, and C. M. Lieber, Nature **415**, 617 (2002).

[17] T. O. Hutchinson, Y.-P. Liu, C. Kiely, C. J. Kiely, and M. Brust, Advanced Materials **13**, 1800 (2001).

[18] P. Yang, R. Yan, and M. Fardy, Nano Letters **10**, 1529 (2010).

[19] Y. Xia *et al.*, Advanced Materials **15**, 353 (2003).

[20] J. R. Morber, *1D nanowires: understanding growth and properties as steps toward biomedical and electrical application*, PhD thesis, Georgia Institute of Technology, 2008.

[21] Z. L. Wang, Advanced Materials **12**, 1295 (2000).

[22] Y. Xia, J. A. Rogers, K. E. Paul, and G. M. Whitesides, Chemical Reviews **99**, 1823 (1999).

[23] Y. Cui, Z. Zhong, D. Wang, W. U. Wang, and C. M. Lieber, Nano Letters **3**, 149 (2003).

[24] R. Yan, D. Gargas, and P. Yang, Nature Photonics **3**, 569 (2009).

[25] J. C. Johnson *et al.*, Nature Materials **1**, 106 (2002).

[26] B. Tian *et al.*, Nature **449**, 885 (2007).

[27] H. Kind, H. Yan, B. Messer, M. Law, and P. Yang, Advanced Materials **14**, 158 (2002).

[28] Y. Huang, X. Duan, and C. M. Lieber, Small **1**, 142 (2005).

[29] L. C. Chuang *et al.*, Nano Letters **11**, 385 (2011).

[30] M. Schiek *et al.*, Small **4**, 176 (2008).

[31] T. Sekitani, U. Zschieschang, H. Klauk, and T. Someya, Nature Materials **9**, 1015 (2010).

[32] M. S. Lee *et al.*, Thin Solid Films **477**, 169 (2005).

[33] A. L. Briseno *et al.*, Nano Letters **7**, 668 (2007).

[34] Y. Tong *et al.*, Langmuir **26**, 1130 (2010).

[35] A. Borras, M. Aguirre, O. Groening, C. Lopez-Cartes, and P. Groening, Chemistry of Materials **20**, 7371 (2008).

[36] F. Balzer and H.-G. Rubahn, Applied Physics Letters **79**, 3860 (2001).

[37] J. Roncali, P. Leriche, and A. Cravino, Advanced Materials **19**, 2045 (2007).

[38] T. Shimizu *et al.*, Advanced Materials **19**, 917 (2007).

[39] A. I. Hochbaum, R. Fan, R. He, and P. Yang, Nano Letters **5**, 457 (2005).

[40] M. C. Wang and B. D. Gates, Materials Today **12**, 34 (2009).

[41] Y. Li and J.-J. Delaunay, *Progress Toward Nanowire Device Assembly Technology* (Paola Prete (Ed.), 2010).

[42] A. Javey, Nam, R. S. Friedman, H. Yan, and C. M. Lieber, Nano Letters **7**, 773 (2007).

[43] Y. Huang, X. Duan, Q. Wei, and C. M. Lieber, Science **291**, 630 (2001).

[44] S. Yan, L. Lu, H. Meng, N. Huang, and Z. Xiao, Nanotechnology **21**, 095303 (2010).

[45] G. Yu, A. Cao, and C. M. Lieber, Nature **2**, 372 (2007).

[46] K. S. Kim *et al.*, Nature **457**, 706 (2009).

[47] J.-Y. Lee, S. T. Connor, Y. Cui, and P. Peumans, Nano Letters **8**, 689 (2008).

[48] R. Krupke, F. Hennrich, H. v. Löhneysen, and M. M. Kappes, Science **301**, 344 (2003).

[49] C.-H. Liu and X. Yu, Nanoscale Research Letters **6**, 75 (2011).

[50] S. Myung, M. Lee, G. Kim, J. Ha, and S. Hong, Advanced Materials **17**, 2361 (2005).

[51] Z. Fan *et al.*, Nano Letters **8**, 20 (2008).

[52] R. Yerushalmi, Z. A. Jacobson, J. C. Ho, Z. Fan, and A. Javey, Applied Physics Letters **91**, 203104 (2007).

[53] Y. Wu *et al.*, Chemistry - A European Journal **8**, 1260 (2002).

[54] J. Kjelstrup-Hansen, O. Hansen, H.-G. Rubahn, and P. Bøggild, Small **2**, 660 (2006).

[55] C. H. Lee, D. R. Kim, and X. Zheng, Proceedings of the National Academy of Sciences **107**, 9950 (2010).

[56] J. H. Oh *et al.*, Proceedings of the National Academy of Sciences **106**, 6065 (2009).

[57] J. Kjelstrup-Hansen, S. Dohn, D. N. Madsen, K. Molhave, and P. Boggild, Journal of Nanoscience and Nanotechnology **6**, 1995 (2006).

[58] K. Thilsing-Hansen, *Growth and Integration of Organic Nanofibers in Devices*, PhD thesis, University of Southern Denmark, 2010.

[59] C. Simbrunner *et al.*, ACS Nano **4**, 6244 (2010).

[60] K. Al-Shamery, H.-G. Rubahn, and H. Sitter, *Organic Nanostructures for Next Generation Devices* (Springer, 2008).

[61] F. Balzer and H.-G. Rubahn, Advanced Functional Materials **15**, 17 (2005).

[62] J. Kjelstrup-Hansen, *Integration of Nanocomponents in Microsystems*, PhD thesis, Technical University of Denmark, 2006.

[63] R. Resel, Thin Solid Films **433**, 1 (2003).

[64] F. Balzer and H. G. Rubahn, Surface Science **548**, 170 (2004).

[65] K. Müller and C. Chang, Surface Science **14**, 39 (1969).

[66] D. E. Williams and Y. Xiao, Acta Crystallographica - Section A **49**, 1 (1993).

[67] V. E. Klymenko and V. M. Rozenbaum, **110**, 5978 (1999).

[68] J. Brewer and H.-G. Rubahn, Physica Status Solidi (c) **2**, 4058 (2005).

[69] F. Balzer *et al.*, Nanotechnology **17**, 984 (2006).

[70] F. Balzer, A. Pogantsch, and H.-G. Rubahn, Journal of Luminescence **129**, 784 (2009).

[71] G. Heimel, D. Somitsch, P. Knoll, and E. Zojer, Synthetic Metals **139**, 823 (2003), Proceedings of the Fifth International Topical Conference on Optical Probes of Conjugated Polymers and Organic and Inorganic Nanostructures.

[72] G. Heimel, D. Somitsch, P. Knoll, J.-L. Bredas, and E. Zojer, The Journal of Chemical Physics **122**, 114511 (2005).

[73] F. Balzer, V. G. Bordo, A. C. Simonsen, and H.-G. Rubahn, Physical Review B **67**, 115408 (2003).

[74] J. Brewer, C. Maibohm, L. Jozefowski, L. Bagatolli, and H.-G. Rubahn, Nanotechnology **16**, 2396 (2005).

[75] F. Quochi *et al.*, Journal of Luminescence **112**, 321 (2005).

[76] F. Quochi *et al.*, The Journal of Physical Chemistry B **109**, 21690 (2005).

[77] F. Quochi *et al.*, Applied Physics Letters **88**, 041106 (2006).

[78] D. J. Gundlach, Y.-Y. Lin, T. N. Jackson, and D. G. Schlom, Applied Physics Letters **71**, 3853 (1997).

[79] M. Klemenc, F. Meghdadi, S. Voss, and G. Leising, Synthetic Metals **85**, 1243 (1997).

[80] C. Maibohm, J. R. Brewer, H. Sturm, F. Balzer, and H.-G. Rubahn, Journal of Applied Physics **100**, 054304 (2006).

[81] A. Carlson *et al.*, Applied Physics Letters **98**, 264104 (2011).

[82] M. C. Coelho and N. Harnby, Powder Technology **20**, 201 (1978).

[83] O. H. Pakarinen *et al.*, Modelling and Simulation in Materials Science and Engineering **13**, 1175 (2005).

[84] J. Israelachvili, *Intermolecular and Surface Forces* (Academic Press, 1992).

[85] M. Nosonovsky and B. Bhushan, Physical Chemistry Chemical Physics **10**, 2137 (2008).

[86] J. Zaumseil and H. Sirringhaus, Chemical Reviews **107**, 1296 (2007).

[87] A. Facchetti, M.-H. Yoon, and T. Marks, Advanced Materials **17**, 1705 (2005).

[88] C. Siol, C. Melzer, and H. von Seggern, Applied Physics Letters **93**, 133303 (2008).

[89] T. B. Singh *et al.*, Advanced Materials **17**, 2315 (2005).

[90] H. H. Henrichsen, *Electrical Interfaces for Organic Nanodevices*, PhD thesis, Technical University of Denmark, 2010.

[91] C. Sheraw, T. Jackson, D. Eaton, and J. Anthony, Advanced Materials **15**, 2009 (2003).

[92] C. Dimitrakopoulos and P. Malenfant, Advanced Materials **14**, 99 (2002).

[93] W. Li, H. E. Katz, A. J. Lovinger, and J. G. Laquindanum, Chemistry of Materials **11**, 458 (1999).

[94] J. Kjelstrup-Hansen, X. Liu, H. H. Henrichsen, K. Thilsing-Hansen, and H.-G. Rubahn, Physica Status Solidi (c) **7**, 2763 (2010).

[95] L.-L. Chua *et al.*, Nature **434**, 194 (2005).

[96] S. Tiwari, E. Namdas, V. Ramgopal Rao, D. Fichou, and S. Mhaisalkar, Electron Device Letters, IEEE **28**, 880 (2007).

[97] R. Schmechel, M. Ahles, and H. von Seggern, Journal of Applied Physics **98**, 084511 (2005).

[98] D. J. Gundlach *et al.*, Journal of Applied Physics **100**, 024509 (2006).

[99] J. Veres, S. Ogier, G. Lloyd, and D. de Leeuw, Chemistry of Materials **16**, 4543 (2004).

[100] J.-H. Chen *et al.*, Advanced Materials **19**, 3623 (2007).

[101] H. B. Michaelson, Journal of Applied Physics **48**, 4729 (1977).

[102] J. Brugger *et al.*, Microelectronic Engineering **53**, 403 (2000).

[103] K. F. Larsen, *Fabrication Of Devices For Epitaxial Growth Of Horizontal III-V Nanowires, Bachelor thesis, Technical University of Denmark*, 2009.

[104] O. Vazquez-Mena *et al.*, Nanotechnology **20**, 415303 (2009).

[105] M. Egginger, S. Bauer, R. Schwödiauer, H. Neugebauer, and N. Sariciftci, Monatshefte für Chemie / Chemical Monthly **140**, 735 (2009).

[106] J. Appenzeller *et al.*, Physical Review Letters **89**, 126801 (2002).

[107] D. Li *et al.*, Applied Physics Letters **86**, 042105 (2005).

[108] S. R. Saudari, Y. J. Lin, Y. Lai, and C. R. Kagan, Advanced Materials **22**, 5063 (2010).

[109] P. V. Pesavento, R. J. Chesterfield, C. R. Newman, and C. D. Frisbie, Journal of Applied Physics **96**, 7312 (2004).

[110] Y. Guo, G. Yu, and Y. Liu, Advanced Materials **22**, 4427 (2010).

[111] H. Klauk *et al.*, Journal of Applied Physics **92**, 5259 (2002).

[112] C.-a. Di *et al.*, Journal of the American Chemical Society **128**, 16418 (2006).

[113] C. Rost *et al.*, Applied Physics Letters **85**, 1613 (2004).

[114] A. Hepp *et al.*, Physical Review Letters **91**, 1574061 (2003).

[115] J. Zaumseil, R. H. Friend, and H. Sirringhaus, Nature Materials **5**, 69 (2006).

[116] R. Capelli *et al.*, Nature Materials **9**, 496 (2010).

[117] T. Yamao, Y. Shimizu, K. Terasaki, and S. Hotta, Advanced Materials **20**, 4109 (2008).

[118] I. Viola *et al.*, ACS Applied Materials and Interfaces **2**, 484 (2010).

[119] H. Yamamoto *et al.*, Nano Letters **5**, 2485 (2005).

[120] F. A. Boroumand, P. W. Fry, and D. G. Lidzey, Nano Letters **5**, 67 (2005).

[121] R. W. I. de Boer, M. E. Gershenson, A. F. Morpurgo, and V. Podzorov, Physica Status Solidi (a) **201**, 1302 (2004).

[122] F. Cicoira and C. Santato, Advanced Functional Materials **17**, 3421 (2007).

[123] J. Kjelstrup-Hansen, X. Liu, H. H. Henrichsen, K. Thilsing-Hansen, and H.-G. Rubahn, Physica Status Solidi (c) **7**, 2763 (2010).

[124] X. Liu *et al.*, Organic Electronics **11**, 1096 (2010).

[125] J. Kjelstrup-Hansen, P. Bøggild, and H.-G. Rubahn, Journal of Physics: Conference Series **61**, 565 (2007).

[126] X. Liu, J. Kjelstrup-Hansen, H. Boudinov, and H.-G. Rubahn, Organic Electronics **12**, 1724 (2011).

[127] M. S. Weaver *et al.*, Applied Physics Letters **81**, 2929 (2002).

[128] P. Madakasira *et al.*, Synthetic Metals **155**, 332 (2005).

[129] F. Zhang *et al.*, Applied Surface Science **254**, 3045 (2008).

[130] I. L. D. Vollath and D. V. Szabó, MRS Proceedings **703** (2001).

[131] D. Vollath, D. Szabó, and S. Schlabach, Journal of Nanoparticle Research **6**, 181 (2004).

[132] Z. Wang *et al.*, Physics Letters A **350**, 252 (2006).

[133] M. D. Groner, F. H. Fabreguette, J. W. Elam, and S. M. George, Chemistry of Materials **16**, 639 (2004).

[134] A. Kadashchuk *et al.*, The Journal of Chemical Physics **130**, 084901 (2009).

[135] J. A. Merlo and C. D. Frisbie, The Journal of Physical Chemistry B **108**, 19169 (2004).

[136] B. H. Hamadani, D. A. Corley, J. W. Ciszek, J. M. Tour, and D. Natelson, Nano Letters **6**, 1303 (2006).

[137] E. Hecht, *Optics* (Addison Wesley; 4 edition, 2002).

[138] F. Balzer, V. G. Bordo, A. C. Simonsen, and H.-G. Rubahn, Applied Physics Letters **82**, 10 (2003).

[139] V. S. Volkov, S. I. Bozhevolnyi, V. G. Bordo, and H.-G. Rubahn, Journal of Microscopy **215**, 241 (2004).